Design and Analysis of Corrugated Conical Horn Antennas with Terahertz Applications

Presented by

Fiachra Cahill, B.Sc

A thesis submitted for the degree of

Master of Science

Department of Experimental Physics
Maynooth University, NUI Maynooth
Co. Kildare
Ireland

September 2015

Head of Department

Professor J. A. Murphy, M.Sc., M.S., Ph.D.

Research Supervisor

Dr Créidhe O' Sullivan, Ph.D.

Table of Contents

Abstract

The focus of this thesis is the design and analysis of corrugated conical horn antennas for use in the THz region of the electromagnetic spectrum, for the company SWISSto12®. These antennas are designed to work across the industry standard WR frequency bands, as free-space radiators or as part of a larger quasi-optical network. The main analysis tools used in this work were the in-house mode-matching code, SCATTER, and the commercially available CST: Microwave Studio, which makes use of the finite integration technique. A version of SCATTER which incorporated creation of a corrugated horn antenna's geometry from user chosen inputs was used to perform parametric sweep analysis when designing the horn antennas. The main design stages were (1) a rectangular to circular transition from a WR rectangular waveguide to a circular waveguide input, (2) a circular smooth-walled to corrugated transition and (3) a transition from a small diameter corrugated waveguide to either a large diameter corrugated waveguide or to free-space. Several styles were examined for the various design stages; the choice of style for the final designs was influenced not only by their performance but also by manufacturing feasibility and cost. Overall, nine individual designs for the WR-1.0. WR-1.5, WR-3.4, WR-5.1, WR-6.5, WR-6.5+, WR-10 and WR-10+ bands have been completed to meet the criteria set by SWISSto12; two of these designs have been manufactured and tested and the results from the measurements performed are presented here.

Acknowledgements

First of all I must thank my supervisor Dr Créidhe O' Sullivan for her constant support and encouragement and for her many kind words over the past two years. I also need to especially mention Dr Stephen Doherty for his mentorship and guidance and for organizing my funding from SWISSto12, without which this thesis may have been very different. I would like to thank all of the other senior members of the Terahertz group: Dr J. Anthony Murphy, Dr Marcin Gradziel and Dr Neil Trappe who have all helped me out in one way or another during course of this Masters. I am likewise grateful to the rest of the academic staff in the department: Dr Frank Mulligan and Dr Peter van der Burgt for organising and helping us in the second-year labs, to Dr Niall McKeith for doing the same in first-year labs and also for providing me with some work in the Science Museum over the summer of 2014 and to Dr Michael Cawley. Furthermore, I am thankful to the members of the administrative and technical staff: Ms Grainne Roche, Mr Derek Gleeson, Mr John Kelly, Mr Pat Seery, Mr Dave Watson, Mr (soon to be Dr) Ian McAuley and Ms. Marie Galligan for keeping the department running smoothly and providing me with help when it was needed. To my fellow postgrads: thanks for sharing the experience. A special thanks goes to those I shared an office with Colm, Niamh, Patrick and especially Steve and Donnacha for the many interesting discussions (not just about physics!) and positivity, I couldn't have asked for better office-mates.

I must thank SWISSto12 (especially Dr Alessandro Macor and Dr Emile de Rijk) for providing me with financial support and interesting work. Also the MU Department of Experimental Physics for funding my trips abroad to visit SWISSto12 in Laussane, EuCAP 2015 in Lisbon and the ESA Alpbach Summer School 2015.

To Hannah, for your constant support and love (and for listening to me moan!) I am truly grateful, and to Emer for always being there for me. Finally to my parents, Mum and Dad, I owe the most gratitude; your support throughout my 6 years in university has been unwavering and is something I will be forever grateful for, thank you.

1. Introduction

1.1 Introduction to THz radiation

Terahertz (or THz) radiation refers to electromagnetic (EM) radiation with frequencies (v) of the order 10^{12} Hz, or wavelengths (λ) of the order 0.1 mm. This region is not strictly defined and is interchangeably referred to as the THz region, sub-millimetre region or far-infrared region. Its definition in terms of frequency or wavelength is 0.3 THz – 3 THz or 1 mm – 100 μm and sometimes 0.1 THz – 10 THz (1). This region has long been called the 'THz Gap' or the last unexplored region of the electromagnetic spectrum due to the lack of readily available sources and detectors. This gap is now being filled as the scientific and engineering community at large is taking an interest in applications at these wavelengths. The THz region in the context of the electromagnetic spectrum as a whole is shown in Figure 1.1.
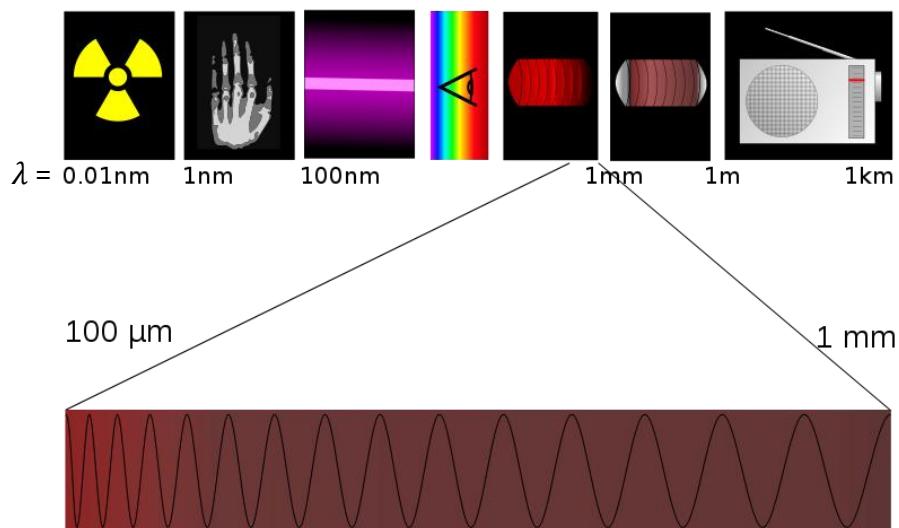
Figure 1.1: The electromagnetic spectrum, highlighting the location of the THz region (source: "Spectre Terahertz" by Tatoute. Licensed under CC BY-SA 3.0 via Wikimedia Commons)

One reason this gap formed in the first place is that it exists between two regimes of EM wave analysis. At shorter wavelengths there is the optical regime, where traditional mirrors and lenses are useful and analysed using ray tracing and at higher wavelengths the use of radio-wave electronic circuits and analysis is the norm. The gap is closing in from both sides, as optical techniques are being applied to increasing wavelengths and microwave techniques are being applied to

decreasing wavelengths. A combination of technologies and analysis techniques are necessary for the reception, transmission and modelling of THz waves.

1.2 Applications of THz radiation

The scope for exploitation of sub-millimeter waves is large and varied. Originally of interest to astronomers and observational cosmologists, there is now increasing interest from other areas of science and industry: physics (2), plasma-physics (3) chemistry (4), biology (5), materials science (6) and medicine (7). There is also a large interest in security applications (8).

1.2.1 Astronomical applications.

The astronomical applications of THz radiation lie in observations of the low-energy Universe. From Wien's law, $\lambda_{max}T = b$, where b is Wien's constant (2.8×10^3 m.K), it can be seen that blackbody temperature and peak wavelength are inversely proportional: long wavelengths imply colder temperatures. In fact; 1 mm - 100 μm corresponds to blackbody temperatures of 29.8 K – 2.98 K.

Some recent missions working in this range are the Herschel Space Observatory, the Atacama Large Millimetre Array (ALMA) and the Planck surveyor. Herschel was a space observatory operating in the wavelength band 55 – 672 μm, located at L2 (the second Earth-Sun Lagrange point). It was launched in 2009 and finished its mission in 2013. Herschel's scientific objectives included: peering through dust-enshrouded regions of star-formation activity in the Milky-Way and neighbouring galaxies in order to better understand the stellar lifecycle, detailed studies of the physics and chemistry of the interstellar medium, spectroscopic and photometric studies of comets, asteroids and outer planet atmospheres and their satellites, and to survey the cosmic infrared background (9).

Figure 1.2: Image from the Herschel Space Observatory showing the distribution of gas and dust in the Taurus Molecular Cloud. (10)

ALMA is a ground based observatory, operating at wavelengths from 0.3 – 0.96 mm. Radiation at these wavelengths is strongly absorbed by water in the atmosphere, for this reason ALMA is situated in the driest place on Earth: the Atacama Desert in Chile. Currently still being assembled, ALMA will consist of up to 66 Cassegrain antennas with 12 m and 7 m primary dishes, with variable baseline separations of up to 15 km. The ability to change configuration will allow ALMA to change its field of view and angular resolution effectively allowing it to "zoom in" on areas of interest. The science goals of ALMA include: determining the redshift of star-forming galaxies, to image the gas and dust in protostellar and protoplanetary disks around young Sun-like stars, to perform detailed studies of the interstellar medium, to study in detail the process of star-formation from the gravitational collapse of molecular clouds and the composition of these clouds and many more (11). An image taken using the 2011 ALMA configuration is shown in Figure 1.3.

Figure 1.3: Composite image of the Antennae galaxies from ALMA and the Hubble space telescope. The red areas are star forming regions. (12)

The Planck Surveyor was a mission to provide the most detailed study of the Cosmic Microwave Background (CMB) ever achieved. Launched in 2009 (on the same rocket as Herschel), it completed its mission in 2013 and was also in orbit about the L2 point. Its band of operation was 27 GHz to 1 THz. Planck has released the best estimates for: the age of the Universe (13.798 ± 0.037 billion years), Hubble's constant (67.8 ± 0.77), baryon density (0.02214 ± 0.00024) cold dark matter density (0.1187 ± 0.0017) and the dark energy density (0.692 ± 0.010) amongst

other things (13). The Planck all sky map of the CMB is shown in Figure 1.4. This is a Mollweide projection of the CMB temperature anisotropies, showing fluctuations in temperature from when the Universe was approximately 380,000 years old. This data informs theories about the evolution of structure in the Universe.
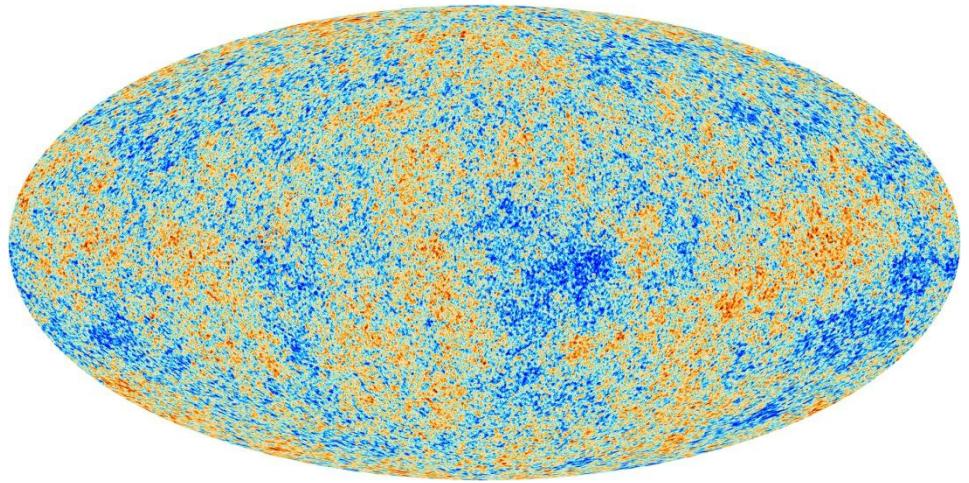
Figure 1.4: Planck all sky map. (14)

Clearly there is a huge amount of interesting astrophysics to be done in the THz region. Herschel, ALMA and Planck all have instruments that were designed in collaboration with Maynooth University.

1.2.2   **Commercial applications**

Apart from scientific research applications, there are also several commercial uses for THz radiation (15). Some of these are in the pharmaceutical industry, for example, the coatings of pharmaceutical tablets control the release of the active ingredients, non-uniformity or other defects in the coating may severely compromise the function of the tablet. Using THz imaging it is possible to measure the quality of tablet coatings to within the order of THz wavelengths. It is also possible using similar techniques to measure tablet density and moisture content quickly, making it suitable for production-line use. Another application, which is gaining a lot of attention at the moment, is in security. Because it is absorbed by skin but not by clothing or metallic objects, THz radiation is useful for performing security scanning for concealed items in a non-invasive manner. Security scanners such as the one shown in Figure 1.5 are already in place in airports around the world. Due to its non-ionizing properties it is perfectly safe to perform these scans.

Figure 1.5: Image of a person carrying a concealed weapon taken using a THz security scanner (left) and an example of such a scanner (right) (Source: http://www.sds.l-3com.com).

This non-ionizing characteristic of THz radiation is also of interest to the medical community as a way of performing safe diagnostic scans, such as examining a wound underneath a bandage without needing to remove the bandage.

An almost ubiquitous component of these applications is the horn antenna, which is the main focus of this thesis. EM waves can be efficiently propagated through both waveguides and free-space and horn antennas are used to couple power between them. Horn antennas will be discussed further in chapter 2. There are many more current and potential applications, some of which will be addressed in section 1.3

1.3 SWISSto12®

SWISSto12® is a start-up company based in Laussane, Switzerland that specializes in THz instrumentation. Founded in 2011, they began in the plasma physics research group in École Polytechnique Federal de Laussane (EPFL) where they developed a novel manufacturing technique for building corrugated cylindrical waveguides for use in plasma physics experiments, in particular for dynamic-nuclear-polarization nuclear magnetic resonance (DNP-NMR). THz frequencies are of increasing interest to the plasma physics community for use in plasma diagnostics. However, due to the relative scarcity of high powered THz sources, and the large diffraction of THz radiation in free-space propagation, it remains challenging to achieve signal transmission over distances which are orders of magnitude greater than the wavelength with a good power coupling to the source, low loss and low dispersion

(16). Corrugated cylindrical waveguides are the ideal candidate for this application due to their low signal attenuation. This low-loss is associated with the propagation of the HE_{11} hybrid electric mode, which has a theoretical loss of the order 1% per 100 m over a bandwidth of over one octave. The corrugation geometry (Figure 1.6) depends on the wavelength to be propagated and has dimensions smaller than $\frac{\lambda}{2}$.
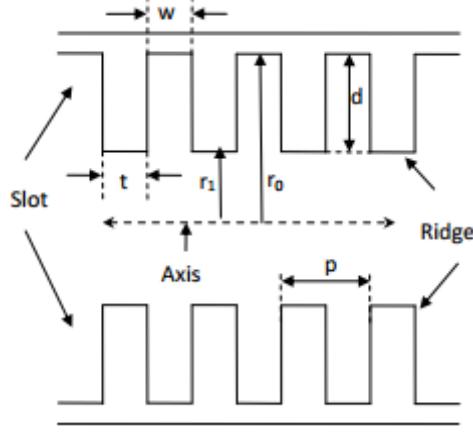
Figure 1.6: Corrugated waveguide geometry.

Until very recently it has been extremely difficult to manufacture corrugated waveguides for use at high frequencies, due to the sub-millimetre scale required. Traditionally, corrugated waveguides have been built by machining inside hollow metal tubes; this is limited by current technology to several hundreds of GHz, over a few cm with inner radii of the order of 1 cm. SWISSto12 have developed a new method for manufacturing single mode (HE_{11}) corrugated waveguides in the THz range using a "stacked rings" approach, with application up to 7.5 THz over tens of centimetres, without mechanical degradation of the dimensions (16). The stacked rings approach involves creating the waveguides by stacking individual rings of alternating radius and thickness inside a guiding pipe, as seen in Figure 1.7.
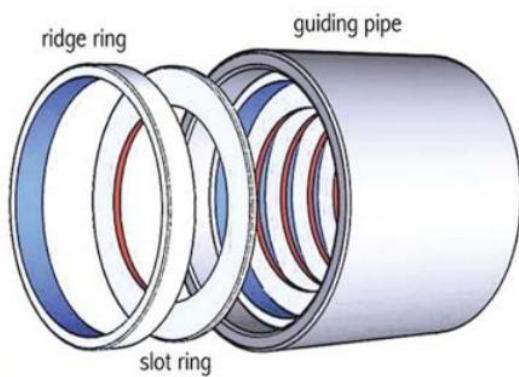
Figure 1.7: Stacked rings approach to building corrugated waveguides.

These rings are obtained from laminated high-precision stainless steel sheets with thicknesses down to $10 \pm 1\ \mu m$, cut by electric discharge machining to accuracies of $\pm\ 2\ \mu m$. The rings are coated in gold to improve their conductivity, and therefore the transmission quality of the waveguide. The robustness of this technique has been demonstrated up to 1.5 THz (16). It also possible, using this technique, to produce more complex corrugated horn antennas. The driver behind development of these waveguides was for use in DNP-NMR experiments carried out at EPFL. It was soon realised that another application would be spectroscopic measurements of materials, which lead to the development of the material characterisation kit (MCK), which utilises the low loss properties of the corrugated waveguide.

The MCK is used for fast analysis of the spectroscopic (i.e. frequency dependent) characteristics of certain materials. It is used in conjunction with a vector network analyser (VNA) in the configuration shown in Figure 1.8:
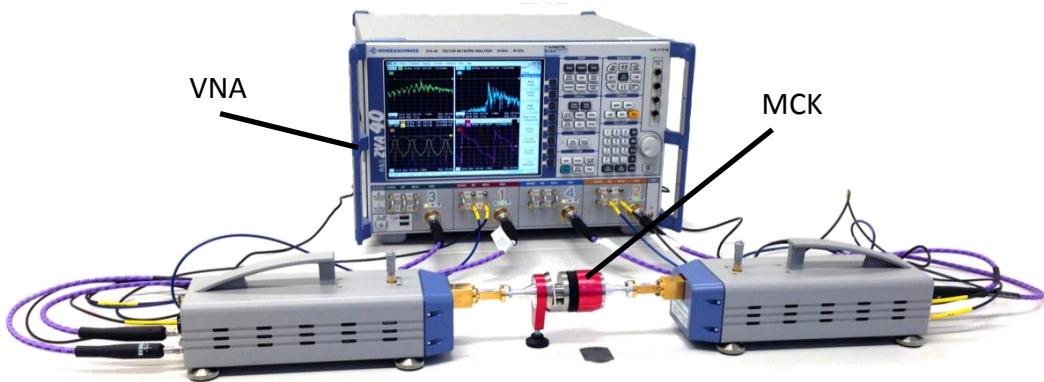
Figure 1.8: SWISSto12's material characterisation kit.

A sample is placed in the MCK and the transmission and reflection properties of the material are measured across a wide frequency band using the VNA. The VNA uses frequency extension modules to produce the THz frequencies required and it outputs this signal through a rectangular waveguide. In order to bridge the gap between the rectangular frequency extension module waveguide and SWISSto12's corrugated waveguide a transition component is required. The perfect candidate for this is a corrugated conical horn antenna with a circular to rectangular transition at the narrow aperture. This is the component which has been designed by the author across 6 frequency bands. The design process and performance of the transitions

and antennas will be described in detail in the following chapters. These antennas can be used as part of the MCK or as free-space radiators. The MCK layout is shown in Figure 1.9. The horn or corrugated convertor is connected to the rectangular waveguide using a self-aligning flange, these flanges are of standard size for VNA extenders, allowing for a modular design of the horn/convertor components. Some results from measurements of a sample of n-doped silicon are shown in Figure 1.10.
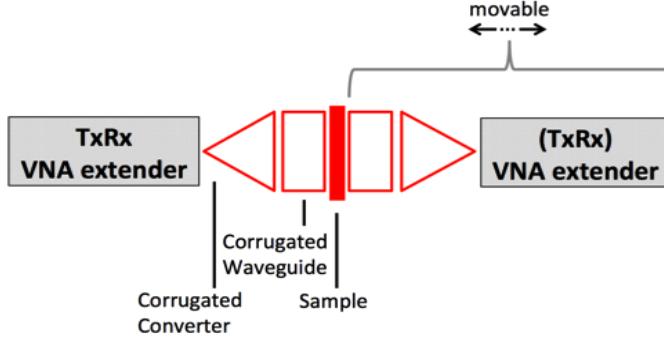
Figure 1.9: Material characterisation kit layout.
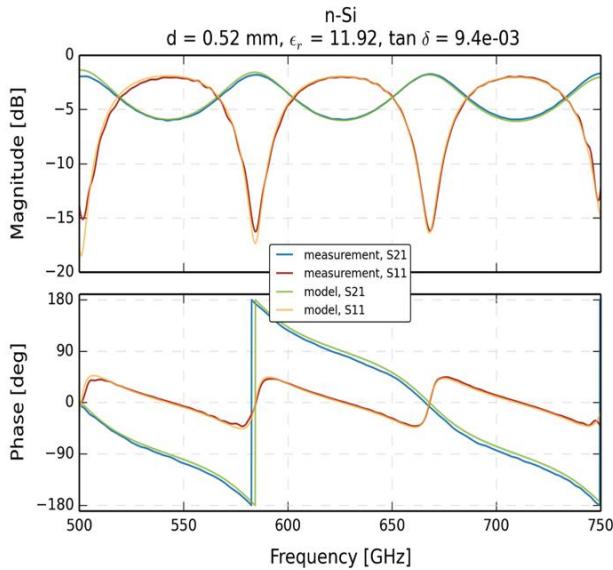
Figure 1.10: Transmission (S21) and reflection (S11) measurements compared to theoretical predictions for n-Si, assuming a thickness (d) of 0.52 mm, permittivity (ϵ_r) of 11.92 and a dielectric loss tangent ($\tan(\delta)$ of 9.4×10^{-3}). These were taken with a previously developed prototype for the WR-1.5 band (not designed by the author) (17).

A recent addition to SWISSto12's capabilities is 3D stereolithography (3D printing) of passive components such as waveguides or horn antennas (18). The printed material is a polymeric non-conductive material, in order to meet the reflection requirements of waveguides this must be coated in a conductive layer. In this case gold is applied to the appropriate areas of the components using an electroless plating technique (ELP). ELP is a simple low-cost method of metalizing dielectric

substrates. First the non-conductive surfaces are activated by a deposition of cationic metallic ions, and then coated in a solution containing a gold salt. Deposition rates are typically a few hundred nanometres per hour, allowing thickness of up to 1 μm to be reached. In order for a material to be highly reflective it requires a thickness of at least three times the skin depth, which for frequencies of over 50 GHz is less than 1 μm. The validity of this technique has also been tested and shown to work well (18). The nature of the 3D-printing allows complex structures to be built as single pieces. The technique is also a relatively fast and cheap way to produce these components. The components are lightweight making them of particular interest for future space missions. Some examples of 3D printed components developed by SWISSto12 are shown in Figure 1.11:

Figure 1.11: 3D printed components from Swissto12. A pyramidal horn antenna (left) and a cutomised waveguide (right).

1.4 Outline of thesis

Chapter 1. In this chapter a brief introduction to EM radiation in the THz part of the spectrum was given along with a description of its importance for applications in astrophysics, medical imaging and security. The start-up company SWISSto12 with which I have collaborated was described and the motivation behind the work in this thesis was given.

Chapter 2 introduces the concept of waveguides for transmitting signals in the form of EM radiation. A detailed mathematical description of the modes of propagation of EM waves inside circular waveguides is given including a derivation of the cut-off frequency and guide-wavelength, two important properties of waveguides that will be exploited in a later chapter. Rectangular waveguides and their propagating modes are then described. A discussion on horn antennas and their properties

follows this, including an introduction to the hybrid modes in a smooth-walled horn. I explain how a sudden change in radius can excite additional modes and investigate the combination of waveguide TE and TM modes required to give pure linear polarization. Finally the corrugated circular waveguide is introduced with a mathematical expression for the HE_{11} hybrid mode. In this chapter I have generated plots to aid the visualisation of modes and in the discussion of far-field patterns I have used corrugated horns that I designed as part of this project.

Chapter 3 outlines some simulation techniques used for the analysis of corrugated horn antennas. I begin with the surface impedance model and a hybrid mode analysis. This is an approximate but quick analysis technique. An example of the use of this approach for the ESA Planck satellite is given, along with an explanation of the propagation characteristics of corrugated waveguides. The next technique described is the mode-matching technique, utilised by Maynooth University's SCATTER code. Much of the design work in this thesis required modifying this code to allow various parameters to be optimized. Mode-matching is a technique which takes advantage of scattering matrices to propagate an electromagnetic wave through a corrugated circularly symmetric system. Finally the commercially available electromagnetic simulation tool CST: Microwave Studio is discussed and some basic examples of its use are given. There is also a comparison between a SCATTER and CST simulation. Both SCATTER and CST were used extensively and I give a guideline as to which situations each is best suited.

Chapter 4 includes the design processes involved in rectangular to circular waveguide transitions and corrugated conical horn antennas. The design goals and performance metrics set by SWISSto12 are discussed and several options for designs are explored. A specific example of the design process for a component for the WR-1.0 band is then given. The results for seven final designs for the WR-1.0, WR-1.5, WR-3.4, WR-5.1, WR-6.5, and WR-10 band are given (there are two separate designs for the WR-3.4 band for two separate applications) including their final geometries. There is also a discussion of two designs done for extended bandwidths (WR-6.5+ and WR-10+). An analysis of the geometries is presented in order to identify any trends which would be of use to future designers. Finally a

Monte-Carlo analysis of the effects of the manufacturing tolerances on the performance of three horns operating in different frequency bands is shown.

Chapter 5 contains the results from measurement campaigns on two separate components. The WR-1.5 band horn antenna, of which there are three manufactured versions, had their return loss, HE_{11} content and radiation patterns measured. The WR-6.5 band horn antenna was only considered in the context of an MCK, and so only the return loss and insertion loss measurements are given. For both of these horns there is a comparison between measurement and simulation (all measurements were performed by SWISSto12).

Chapter 6 is a final summary and conclusion on the work carried out in the thesis.

My work in this thesis has contributed to the following papers:

- *C. O'Sullivan*; J. A. Murphy; I. Mc Auley; D. Wilson; M. L. Gradziel; N Trappe; F. Cahill; T. Peacocke; G. Savini; K. Ganga* **"Optical modelling of far-infrared astronomical instrumentation exploiting multimode horn antennas"**, Proc. SPIE 9153, Millimeter, Submillimeter, and Far-Infrared Detectors and Instrumentation for Astronomy VII, 2014
- *S. Doherty, A. von Bieren, F. Cahill*, A. Macor, E. de Rijk, N. Trappe, M. Billod, C. O'Sullivan, M. Favre, M. Gradziel, J.A. Murphy,* **"Rectangular to Large Diameter Conical Corrugated Waveguide Converter Based on Stacked Rings",** European Conference on Antennas and Propagation (EuCAP), 2015

    *Indicates the conference presenter.

2. Introduction to waveguides

The idea of using hollow conducting materials to guide electromagnetic waves was originally developed by Lord Rayleigh in 1897. However their practical application didn't come to the fore until oscillators generating useful amounts of power in the GHz range were developed some years later. Even still, applications in that range were limited until the 1930s when functioning waveguide assemblies were independently developed by teams at Bell Telephone Laboratories and the Massachusetts Institute of Technology, (19). It is extremely impractical/impossible to use standard circuitry at operating frequencies upwards of GHz as the wire's lengths are much greater than a wavelength and so act as transmitters, radiating power away. This power diffracts significantly making free-space propagation unsuitable for applications over distances much greater than a wavelength. Both of these problems are mitigated by the use of waveguides.

The two most commonly used waveguides are circular and rectangular in cross-section; this due to the fact that there are closed form solutions to the electromagnetic wave-equation under the boundary conditions that apply. The principle of operation of waveguides is that wave-fronts which are reflected at the walls interfere in such a way that their transverse fields form a natural set of eigenfunctions. An intuitive description of this is given, for example, in chapter 3 of (20).

2.1 Circular waveguides

Circular waveguides are useful in many applications due to the radial symmetry of the fields they support and, as will be discussed, they can be easily matched to corrugated conical horn antennas which are ubiquitous in many areas of telecommunications and radio astronomy.

It will be shown that for both the magnetic and electric fields, the entire field can be described in terms of the z-component alone. In this section I follow derivations given by (20) and (19).

2.1.1 **Derivation of electric and magnetic fields in a circular waveguide**

We assume that the z-component of the electric field inside the guide has an amplitude which is a function of the transverse components ((r, ϕ) in circular coordinates) and that the *z*-component is dominated by the changing phase (the exponential term in (2.2)).
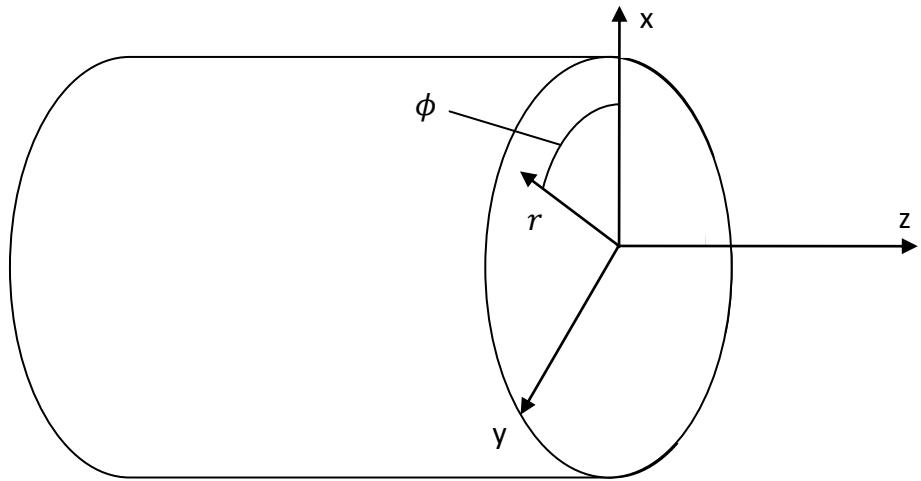
Figure 2.1: Geometry of a circular waveguide

The wave equation for this component is given by:

$$\nabla^2 \vec{E}_z = \mu\epsilon \frac{\partial^2 \vec{E}_z}{\partial t^2}, \tag{2.1}$$

where

$$\vec{E}_z = E_{0z}(r, \phi)e^{j(\omega t - \beta z)} \tag{2.2}$$

and β is the longitudinal component of the wave number:

$$\beta = \sqrt{k^2 - k_T^2} \tag{2.3}$$

and k_T is the transverse wavenumber. The RHS of equation (2.1) becomes

$$-\mu\epsilon\omega^2 E_{0z}(r, \phi) \, e^{j(\omega t - \beta z)}. \tag{2.4}$$

Evaluating the Laplacian on the LHS of equation (2.1) and dropping the common exponential term leads to

$$\frac{1}{r}\frac{\partial}{\partial r}\left(r\frac{\partial E_{0z}}{\partial r}\right) + \frac{1}{r^2}\frac{\partial^2 E_{0z}}{\partial \phi^2} = (\beta^2 - \mu\epsilon\omega^2)E_{0z}. \tag{2.5}$$

We now apply a separation of variables:

$$E_{0z}(r,\phi) = R(r)\Phi(\phi). \tag{2.6}$$

Dividing across by $R(r)\Phi(\phi)$ and multiplying by r^2 gives:

$$\frac{r}{R(r)}\left(\frac{\partial R(r)}{\partial r} + \frac{\partial^2 R(r)}{\partial r}r\right) - (\beta^2 - \mu\epsilon\omega^2)r^2 + \frac{1}{\Phi(\phi)}\frac{\partial^2 \Phi(\phi)}{\partial \phi^2} = 0 \tag{2.7}$$

We now have separate functions of r and ϕ which when subtracted yield 0. This means that the two functions must be independently equal to the same constant. Starting with the ϕ term we say

$$\frac{1}{\Phi(\phi)}\frac{\partial^2 \Phi(\phi)}{\partial \phi^2} = -m^2. \tag{2.8}$$

Rearranging this so that we have 0 on the RHS and multiplying by $\Phi(\phi)$ leads to a standard homogenous linear differential equation, which has the following set of solutions:

$$\Phi(\phi) = C_1\sin(m\phi) + C_2\cos(m\phi) \tag{2.9}$$

where C_1 and C_2 are constants of integration. In order to satisfy the wave equation, E_{0z} and hence $\Phi(\phi)$, must have period 2π. This will be true if m is an integer. Now, solving for $R(r)$, we start with:

$$\frac{r}{R(r)}\left(\frac{\partial R(r)}{\partial r} + \frac{\partial^2 R(r)}{\partial r}r\right) - (\beta^2 - \mu\epsilon\omega^2)r^2 = m^2 \tag{2.10}$$

Multiplying across by $\frac{R(r)}{r^2}$ and rearranging:

$$\frac{1}{r}\frac{\partial}{\partial r}\left(r\frac{\partial R(r)}{\partial r}\right) + R(r)\left((\mu\epsilon\omega^2 - \beta^2) - \frac{m^2}{r^2}\right) = 0 \tag{2.11}$$

Now, examining the term $\mu\epsilon\omega^2$:

$$\mu\epsilon = \frac{1}{c^2} \tag{2.12}$$

and

$$\omega^2 = \left(\frac{2\pi c}{\lambda}\right)^2 \tag{2.13}$$

so,

$$\mu\epsilon\omega^2 = k^2$$

and from (2.3) we get that

$$k^2 - \beta^2 = k_T^2. \tag{2.14}$$

And finally, with some more rearranging we have:

$$r^2\frac{\partial^2 R(r)}{\partial r^2} + r\frac{\partial R(r)}{\partial r} - R(r)(r^2 k_T^2 - m^2) = 0. \tag{2.15}$$

According to (21 p. 80) Bessel's differential equation can take the form

$$x^2\frac{\partial^2 y}{\partial x^2} + x\frac{\partial y}{\partial x} - y(x^2\lambda^2 - n^2) = 0 \tag{2.16}$$

where n is an integer and the order of the Bessel function that is a solutions to this equation. Clearly, (2.15) will have solutions which are Bessel functions. According to (20 p. 84), there are two possibilities for k_T.

If $k^2 < \beta^2$ then k_T^2 will be negative (so k_T will be complex) and according to (20) the solutions for $R(r)$ will be a linear combination of $I_n(k_T r)$ and $K_n(k_T r)$ where I_n is a modified Bessel function of the first kind and K_n is a modified Bessel function of the second kind. $K_n(k_T r)$ is infinite at the origin, so this is unphysical and $I_n(k_T r)$ has no zeros except at the origin, however $\vec{E}_z$ must be zero at the waveguide walls so we can discard this solution as well. This leaves us with solutions for $k^2 > \beta^2$, namely: $J_n(k_T r)$ and $Y_n(k_T r)$ (where J_n is a Bessel function of the first kind and Y_n is a Bessel function of the second kind) so the solution for $R(r)$ is given by

$$R(r) = A_1 J_m(k_T r) + A_2 Y_m(k_T r). \tag{2.17}$$

However, $Y_n(k_T r)$ is infinite at $r = 0$, which means that A_2 must be equal to zero. This leaves us with our final solution for E_z:

$$E_z = A_1 J_m(k_T r)(C_1\sin(m\phi) + C_2\cos(m\phi))\, e^{j(\omega t - \beta z)} \tag{2.18}$$

Similarly an expression for H_z can be derived (19):

15

$$H_z = \text{A}_1' J_m(k_T r)(\text{C}_1' \sin(m\phi) + \text{C}_2' \cos(m\phi))\, e^{j(\omega t - \beta z)} \qquad (2.19)$$

The other components of the electric and magnetic field can be shown to be function of these z components as follows. We start with Maxwell's curl equations:

$$\nabla \times \vec{E} = -\mu \frac{\partial \vec{H}}{\partial t} \qquad (2.20)$$

$$\nabla \times \vec{H} = \epsilon \frac{\partial \vec{E}}{\partial t}. \qquad (2.21)$$

By expanding, simplifying and matching the vector components the transverse fields are found to be (19):

$$H_{0\phi} = -\frac{j}{k_T^2}\left(\omega\epsilon \frac{\partial E_{0z}}{\partial r} + \frac{\beta}{r} \frac{\partial H_{0z}}{\partial \phi}\right) \qquad (2.22)$$

$$H_{0r} = -\frac{j}{k_T^2}\left(\beta \frac{\partial H_{0z}}{\partial r} - \frac{\omega\epsilon}{r} \frac{\partial E_{0z}}{\partial \phi}\right) \qquad (2.23)$$

$$E_{0\phi} = -\frac{j}{k_T^2}\left(\frac{\beta}{r} \frac{\partial E_{0z}}{\partial \phi} - \omega\mu \frac{\partial H_{0z}}{\partial r}\right) \qquad (2.24)$$

$$E_{0r} = -\frac{j}{k_T^2}\left(\beta \frac{\partial E_{0z}}{\partial r} + \frac{\omega\mu}{r} \frac{\partial H_{0z}}{\partial \phi}\right). \qquad (2.25)$$

2.1.2 Circular waveguide modes

The electric and magnetic fields inside a uniform (symmetric) waveguide can be expressed mathematically as a sum of modal functions or modes, since waves reflected at the walls of the guide will naturally form a set of resonant modes in the transverse plane. There are two types of propagating modes in hollow metal waveguides: transverse electric (TE) and transverse magnetic (TM). TE modes are so-called due to the fact that the entire electric field is in the plane perpendicular to the propagation direction i.e. $E_z = 0$. TM modes then have the property that $H_z = 0$. Using (2.18), (2.19) and (2.22) - (2.25) we can derive expressions for the transverse fields:

TM modes:

$$H_{0r} = \frac{jm\omega\epsilon}{k_T^2 r}\left[A_1'J_m(k_T r)\big(C_1\sin(m\phi) + C_2\cos(m\phi)\big)\right] \tag{2.26}$$

$$H_{0\phi} = -\frac{j\omega\epsilon}{k_T^2 r}\left[A_1'J_m'(k_T r)\big(C_1\sin(m\phi) + C_2\cos(m\phi)\big)\right] \tag{2.27}$$

$$E_{0r} = -\frac{j\beta}{k_T^2}\left[A_1'J_m'(k_T r)\big(C_1\sin(m\phi) + C_2\cos(m\phi)\big)\right] \tag{2.28}$$

$$E_{0\phi} = -\frac{jm\beta}{k_T^2 r}\left[A_1'J_m(k_T r)\big(C_1\sin(m\phi) + C_2\cos(m\phi)\big)\right]. \tag{2.29}$$

TE modes:

$$H_{0r} = -\frac{j\beta}{k_T^2}\left[A_1J_m'(k_T r)\big(C_1\sin(m\phi) + C_2\cos(m\phi)\big)\right] \tag{2.30}$$

$$H_{0\phi} = -\frac{j\beta m}{k_T^2 r}\left[A_1J_m(k_T r)\big(C_1\sin(m\phi) + C_2\cos(m\phi)\big)\right] \tag{2.31}$$

$$E_{0r} = -\frac{j\omega\mu m}{k_T^2 r}\left[A_1J_m(k_T r)\big(C_1\sin(m\phi) + C_2\cos(m\phi)\big)\right] \tag{2.32}$$

$$E_{0\phi} = \frac{j\omega\mu}{k_T^2}\left[A_1J_m'(k_T r)\big(C_1\sin(m\phi) + C_2\cos(m\phi)\big)\right]. \tag{2.33}$$

2.1.3 Mode characteristics

If we consider the waveguide to be a perfect electrical conductor (PEC), then the electric field components parallel to the walls of the waveguide and magnetic field component perpendicular to the walls of the waveguide ($E_{0z}, E_{0\phi}$ and H_{0r}) must be zero at the walls. This will be true if

$$J_m(k_T r_a) = 0 \text{ (TM modes)} \tag{2.34}$$

$$J_m'(k_T r_a) = 0 \text{ (TE modes)} \tag{2.35}$$

where r_a is the radius of the waveguide. In other words the argument $k_T r_a$ must be one of the roots of a Bessel function for TM modes and one of the roots of the first derivative of a Bessel function for TE modes (there are infinitely many roots). The subscript *n* will be used to represent the root in question, with $n = 1$ representing the root nearest the origin. So we can represent the roots of a Bessel function with the variable p_{mn} where *m* is the order of the Bessel function and *n* is the root:

$$k_T r_a = p_{mn},$$

$$k_T = \frac{p_{mn}}{r_a}. \tag{2.36}$$

Similarly for TE modes we call the roots of the derivative of a Bessel function p'_{mn}:

$$k_T r_a = p'_{mn},$$

$$k_T = \frac{p'_{mn}}{r_a}.$$

(2.37)

Table 2-1 lists some values of p_{mn} and p'_{mn}. We can now re-express the transverse fields as

TM modes:

$$H_{0r} = \frac{jm\omega\epsilon}{k_T^2 r}\left[A'_1 J_m\left(\frac{p_{mn}}{r_a}r\right)\left(C_1\sin(m\phi) + C_2\cos(m\phi)\right)\right]$$

(2.38)

$$H_{0\phi} = -\frac{j\omega\epsilon}{k_T^2}\left[A'_1 J'_m\left(\frac{p_{mn}}{r_a}r\right)\left(C_1\sin(m\phi) + C_2\cos(m\phi)\right)\right]$$

(2.39)

$$E_{0r} = -\frac{j\beta}{k_T^2}\left[A'_1 J'_m\left(\frac{p_{mn}}{r_a}r\right)\left(C_1\sin(m\phi) + C_2\cos(m\phi)\right)\right]$$

(2.40)

$$E_{0\phi} = -\frac{jm\beta}{k_T^2}\left[A'_1 J_m\left(\frac{p_{mn}}{r_a}r\right)\left(C_1\sin(m\phi) + C_2\cos(m\phi)\right)\right]$$

(2.41)

TE modes:

$$H_{0r} = -\frac{j\beta}{k_T^2}\left[A_1 J'_m\left(\frac{p'_{mn}}{r_a}r\right)\left(C_1\sin(m\phi) + C_2\cos(m\phi)\right)\right]$$

(2.42)

$$H_{0\phi} = -\frac{j\beta m}{k_T^2 r}\left[A_1 J_m\left(\frac{p'_{mn}}{r_a}r\right)\left(C_1\sin(m\phi) + C_2\cos(m\phi)\right)\right]$$

(2.43)

$$E_{0r} = -\frac{j\omega\mu m}{k_T^2 r}\left[A_1 J_m\left(\frac{p'_{mn}}{r_a}r\right)\left(C_1\sin(m\phi) + C_2\cos(m\phi)\right)\right]$$

(2.44)

$$E_{0\phi} = \frac{j\omega\mu}{k_T^2}\left[A_1 J'_m\left(\frac{p'_{mn}}{r_a}r\right)\left(C_1\sin(m\phi) + C_2\cos(m\phi)\right)\right].$$

(2.45)

Thus the modal solutions can be described in terms of two integers: m and n, leading to the notation TE_{mn} and TM_{mn} (sometimes TE_{nl} and TM_{nl}).

Now, by examining the exponential term in the expressions for E_z (2.18) and H_z (2.19) it is clear that if β (which is also known as the propagation constant) is real the field will be a sinusoidal travelling wave, and if β is imaginary the field will decay exponentially with distance z. Since $\beta = \sqrt{k^2 - k_T^2}$, k must be greater than k_T in order for β to be real i.e. $k > \frac{p_{mn}}{r_a}$ (TM modes) or $k > \frac{p'_{mn}}{r_a}$ (TE modes). This means that the cut-on wavelength, $\lambda_{c,mn}$ (the longest wave that will propagate) is given by:

$$\lambda_{c,mn} = \frac{2\pi r_a}{p_{mn}} \text{ (TM modes)} \tag{2.46}$$

$$\lambda_{c,mn} = \frac{2\pi r_a}{p'_{mn}} \text{ (TE modes).} \tag{2.47}$$

Some Bessel roots are given in Table 2-1.

Table 2-1: Some roots of the Bessel function and its derivative, in order of cut on.

TM$_{mn}$ modes			TE$_{mn}$ modes		
m	n	p_{mn}	m	n	p'_{mn}
0	1	2.405	1	1	1.841
1	1	3.832	2	1	3.054
2	1	5.136	0	1	3.832
0	2	5.520	3	1	4.201
3	1	6.380	4	1	5.317

We now also define the guide wavelength (effective wavelength of radiation in a waveguide) as

$$\lambda_{g,mn} = \frac{2\pi}{\beta} = \frac{\lambda}{\sqrt{\left(1 - \left(\frac{\lambda}{\lambda_{c,mn}}\right)^2\right)}} \tag{2.48}$$

A mode whose guide wavelength is greater than the cut-on wavelength will be attenuated exponentially with distance in the propagation direction; such a mode is known as an evanescent mode. These are important when dealing with waveguides whose structure changes over distances that are less than or equal to a wavelength. It is also useful to know what the waveguide impedance, defined as the ratio of transverse electric field to transverse magnetic field is. For TM$_{mn}$ modes:

$$Z_{mn}^{TM} = {E_{0r}}/{H_{0\phi}} = {E_{0\phi}}/{H_{0r}} = {\beta}/{\omega\epsilon} = Z_0\sqrt{1 - \left(\frac{\lambda p_{mn}}{2\pi r_a}\right)^2} \tag{2.49}$$

where, $Z_0 = \sqrt{{\mu}/{\epsilon}}$ is the characteristic impedance of the medium. For TE$_{mn}$ modes:

$$Z_{mn}^{TE} = {\omega\mu}/{\beta} = \frac{Z_0}{\sqrt{1 - \left(\frac{\lambda p'_{mn}}{2\pi r_a}\right)^2}} \tag{2.50}$$

Some plots of the electric field power distribution and direction for a circular waveguide of arbitrary radius are shown in Figure 2.2
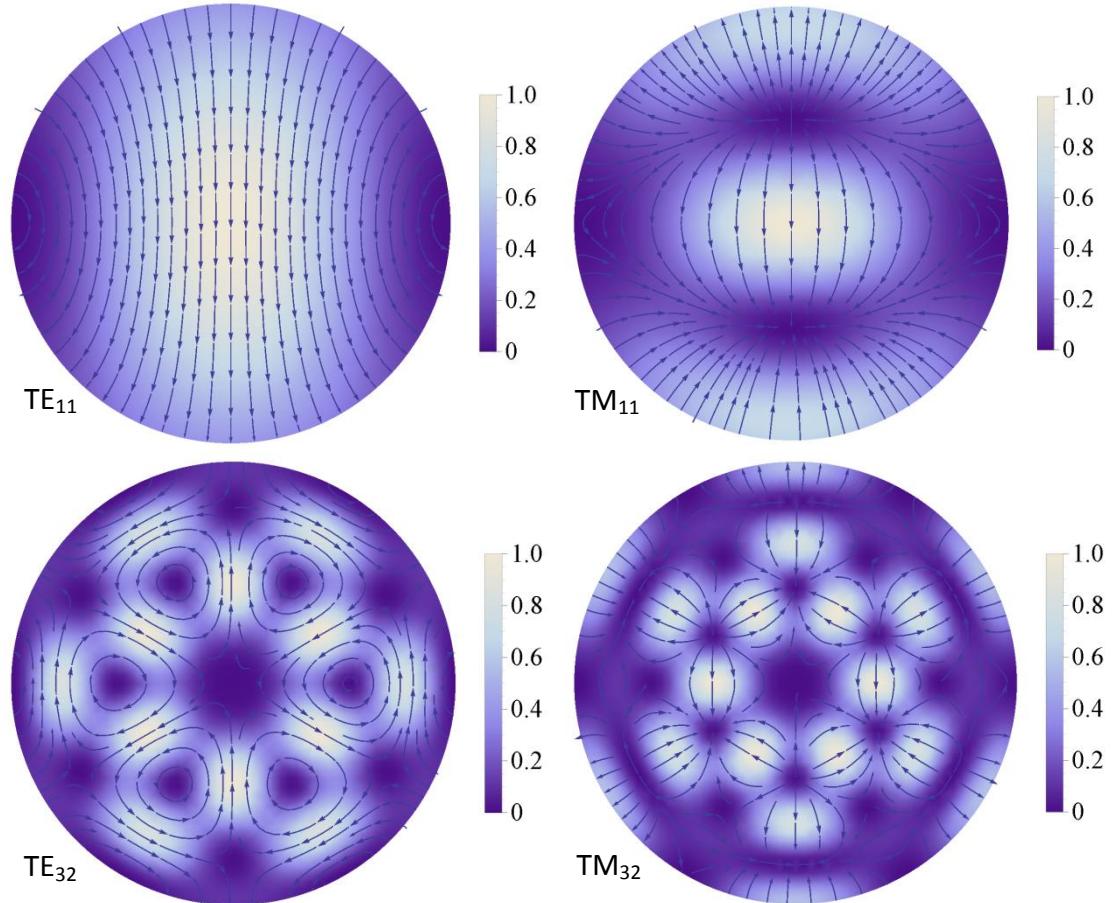

Figure 2.2: Transverse electric field patterns of some circular TE and TM modes showing field power (linear scale) and direction. The arrows are uniform in length and represent the direction of the field only.

In order to generate the plots in Figure 2.2 the x and y components of the fields were found using equations (3.11) to (3.18).

2.2 Rectangular waveguides

Fields in hollow metal rectangular waveguides can be found in a similar way to circular waveguides. By solving the wave equation for the longitudinal $\vec{E}$ and $\vec{H}$ fields as functions of the transverse components (in this case x and y) and applying boundary conditions, the transverse fields can be described as functions of the longitudinal fields (similar to equations (2.22) to (2.25)). Solving this leads to equations 2.31.1 to 2.31.4. Here the boundary conditions are defined by the guide dimensions a and b (see Figure 2.3).
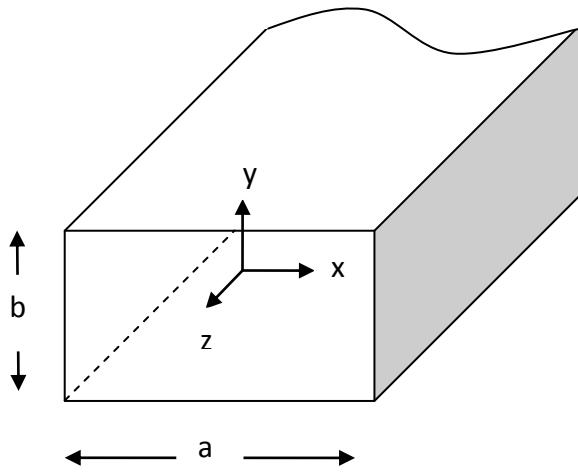
Figure 2.3: Geometry of a rectangular waveguide (by convention the longer side is always in the *x*-direction and called 'a').

The modal equations are given in (19) as:

TM modes:

$$H_{0x} = \frac{j\omega\epsilon n\pi}{k_T{}^2 a} C_{mn} \sin\left(\frac{m\pi x}{a}\right) \cos\left(\frac{n\pi y}{b}\right) \tag{2.51}$$

$$H_{0y} = -\frac{j\omega\epsilon m\pi}{k_T{}^2 b} C_{mn} \cos\left(\frac{m\pi x}{a}\right) \sin\left(\frac{n\pi y}{b}\right) \tag{2.52}$$

$$E_{0x} = -\frac{j\beta m\pi}{k_T{}^2 a} C_{mn} \cos\left(\frac{m\pi x}{a}\right) \sin\left(\frac{n\pi y}{b}\right) \tag{2.53}$$

$$E_{0y} = -\frac{j\beta n\pi}{k_T{}^2 b} C_{mn} \sin\left(\frac{m\pi x}{a}\right) \cos\left(\frac{n\pi y}{b}\right) \tag{2.54}$$

TE modes:

$$H_{0x} = \frac{j\beta n\pi}{k_T{}^2 a} A_{mn} \sin\left(\frac{m\pi x}{a}\right) \cos\left(\frac{n\pi y}{b}\right) \tag{2.55}$$

$$H_{0y} = -\frac{j\beta m\pi}{k_T{}^2 b} A_{mn} \cos\left(\frac{m\pi x}{a}\right) \sin\left(\frac{n\pi y}{b}\right) \tag{2.56}$$

$$E_{0x} = \frac{j\omega\mu n\pi}{k_T{}^2 b} A_{mn} \cos\left(\frac{m\pi x}{a}\right) \sin\left(\frac{n\pi y}{b}\right) \tag{2.57}$$

$$E_{0y} = -\frac{j\omega\mu m\pi}{k_T{}^2 a} A_{mn} \sin\left(\frac{m\pi x}{a}\right) \cos\left(\frac{n\pi y}{b}\right) \tag{2.58}$$

where,

$$\beta = \sqrt{k^2 - k_T{}^2}$$

$$k_T{}^2 = \left(\frac{m\pi}{a}\right)^2 - \left(\frac{n\pi}{b}\right)^2. \tag{2.59}$$

21

As before it is now possible to define a cut-on wavelength from the properties of β, which must be real for a mode to propagate:

$$\lambda_{c,mn} = \frac{2\pi}{\sqrt{\left(\frac{m\pi}{a}\right)^2 - \left(\frac{n\pi}{b}\right)^2}}. \tag{2.60}$$

Here m and n are the mode orders or the number of half wavelengths that fit across the guide in the *x* and *y* directions, respectively. It should be noted that since magnetic field lines must be a closed loop both H_{0x} and H_{0y} are needed for the TM modes, making the TM_{11} mode the lowest order TM mode. Since TE modes have a non-zero H_{0z} it is possible to have TE_{m0} modes and indeed TE_{10} is the fundamental propagating mode in a rectangular waveguide. Guide wavelength and modal impedance can be calculated as before (equations (2.48), (2.49) and (2.50)). Some transverse electric field patterns of a rectangular waveguide are shown in Figure 2.4.
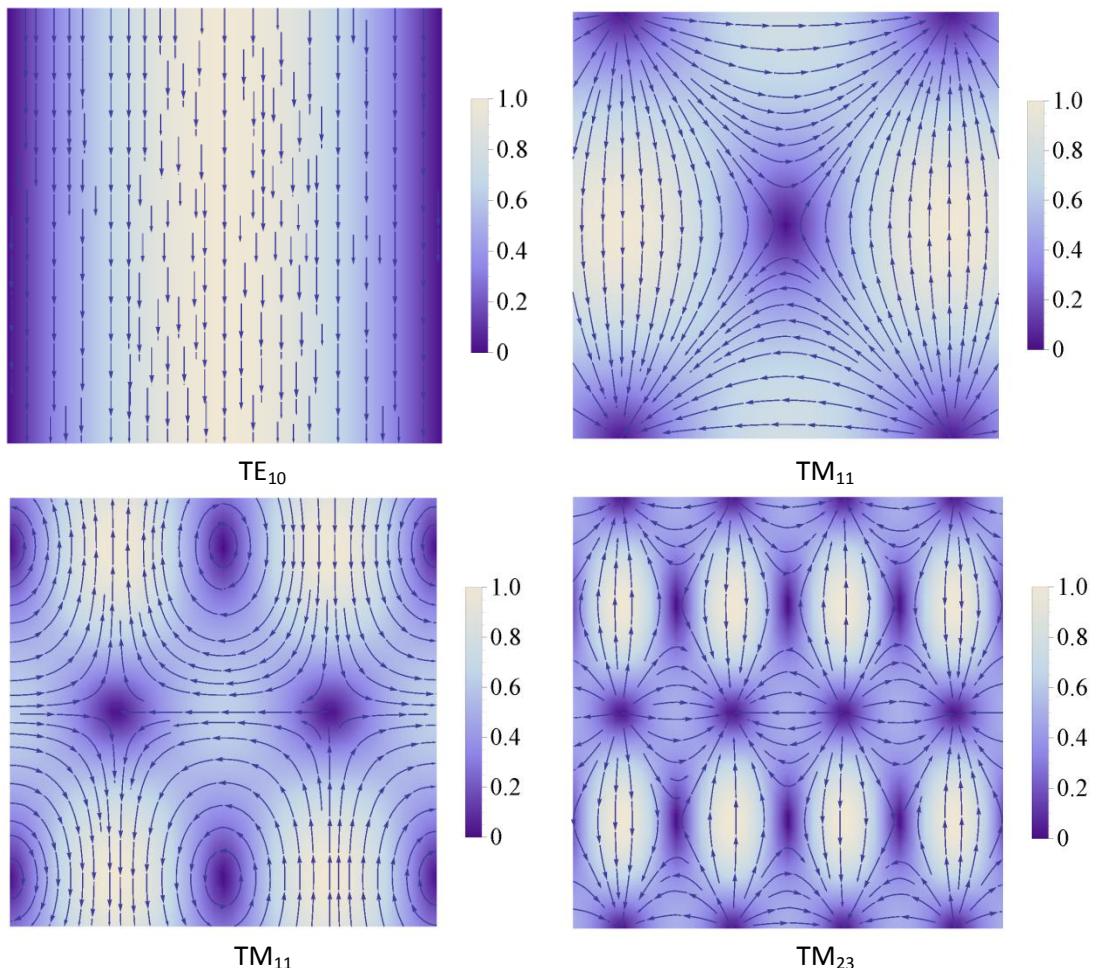

Figure 2.4: Transverse electric and transverse magnetic field patterns of some rectangular modes showing field power (linear scale) and direction.

2.3 Corrugated cylindrical waveguides & horn antennas

2.3.1 Waveguides as antennas

As well as being used as circuit elements to transfer high frequency signals waveguides have been widely used as antennas in scientific and telecommunications projects. By flaring out the waveguide to an aperture which is usually significantly larger than the normal waveguide dimensions, the guide-wavelength can be made to match the free-space wavelength, meaning there will be an insignificant amount of reflection at this junction. This allows a signal to be transmitted or received at specific frequencies. This idea is largely used in reflector telescopes where the antenna is used as a feed for the detector (Figure 2.5).
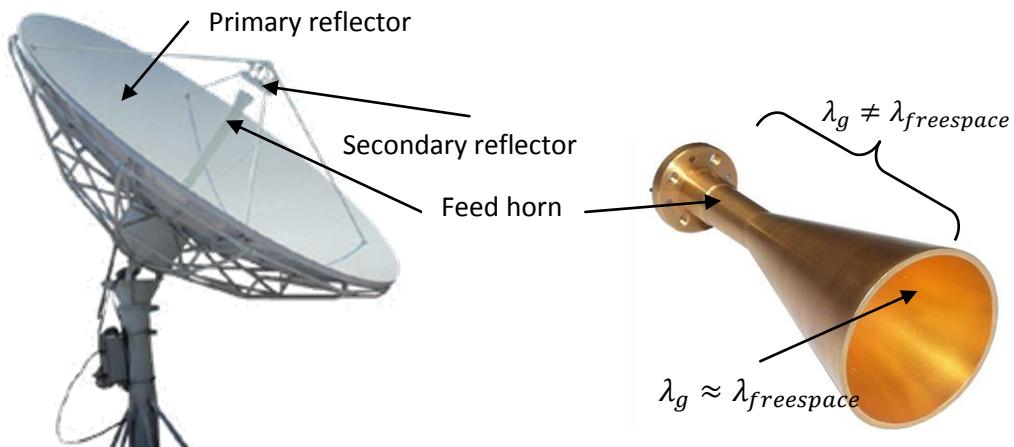
Figure 2.5: Example of a Cassegrain reflector antenna (left) and a standard smooth-walled conical horn antenna (right).

These antennas are commonly referred to as feed horns or horn antennas due to their resemblance to musical horns. The job of an antenna is to produce a beam which has a desired width, side-lobe level, beam symmetry and cross-polarization level. Due to the principle of reciprocity the beam produced by the antenna acting as a radiator is exactly the beam that will couple to the antenna acting as a receiver.

The aperture fields of horn antennas have the same power distribution as the fields inside a waveguide of the same shape, but with a phase curvature depending on the flare length of the horn. The far-field can be worked out, if the aperture field is known, by several methods, including via a Fourier-transform, using the Fresnel diffraction integral or the Gaussian beam mode approximation. A typical far-field

pattern is described by displaying a cut through the 0° and 90° (or E and H) planes and a 45° cut to show cross-polarization, with power (in dB) as the dependent variable and off-axis distance as the independent variable, as shown in Figure 2.6.
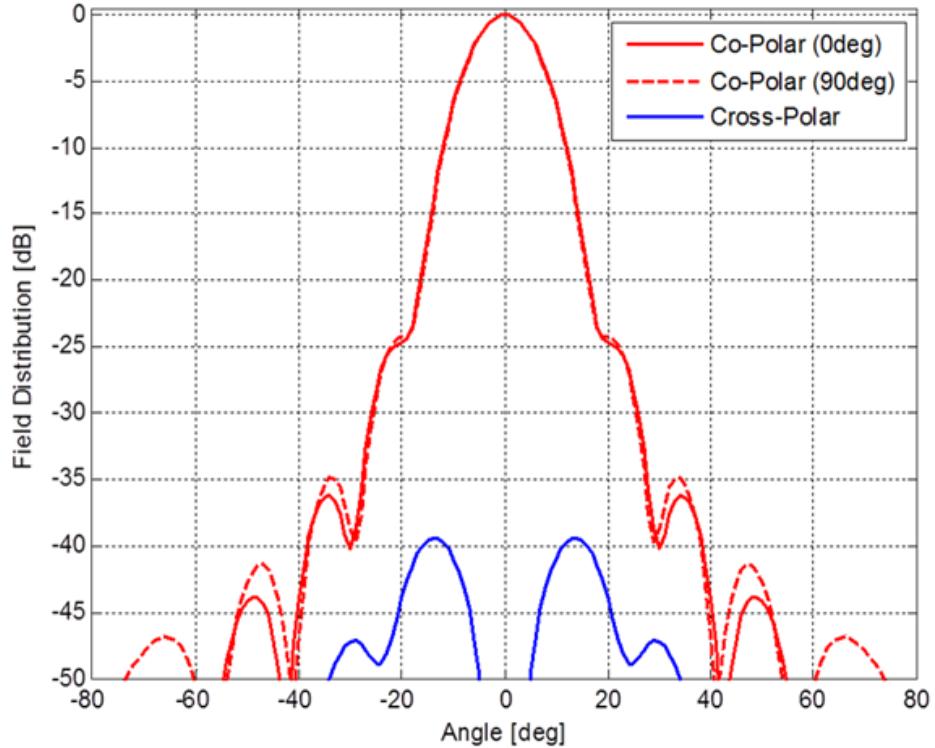
Figure2.6: Far-field beam pattern from a corrugated conical horn antenna designed by the author for the WR-10 band at 91.25GHz.

2.3.2 **Hybrid modes**

Hybrid modes are formed when both TE and TM modes are propagating in a waveguide, and are a coherent linear combination of them. Possibly the most important hybrid mode is the HE_{11} mode, which will feature heavily in this thesis. This mode is highly desirable due to its rotational symmetry, high level of on-axis power (which leads to low side-lobes in the far-field) and suppressed cross-polar content.

These properties of the HE_{11} mode depend on the relative power of TE_{11} and TM_{11} modes. It is often stated (22) that the ideal HE_{11} mode has 85% TE_{11} and 15% TM_{11} without explaining where these levels come from. However, great insight can be gained by simply examining the cross-polar content of a HE_{11} mode while varying

the ratio of TE_{11} power to TM_{11} power. This can be done using the functions in (2.61) and (2.62).

$$f_1(c) = \frac{\left(\sqrt{c^2}TE_{11}^y + \sqrt{(1-c^2)}TM_{11}^y\right)^2}{\left(\sqrt{c}TE_{11}^x + \sqrt{(1-c^2)}TM_{11}^x\right)^2 + \left(\sqrt{c^2}TE_{11}^y + \sqrt{(1-c^2)}TM_{11}^y\right)^2} \quad (2.61)$$

$$f_2(c) = \frac{\left(\sqrt{c^2}TE_{11}^x + \sqrt{(1-c^2)}TM_{11}^x\right)^2}{\left(\sqrt{c}TE_{11}^x + \sqrt{(1-c^2)}TM_{11}^x\right)^2 + \left(\sqrt{c^2}TE_{11}^y + \sqrt{(1-c^2)}TM_{11}^y\right)^2} \quad (2.62)$$

where TE_{11}^y is the total power in the $\vec{y}$-component of the TE_{11} field (cross-polar direction), c is a constant which is varied from 0.01 to 1 and represents the fraction of the total power in the TE_{11} mode. Assuming a perfect HE_{11} mode means that if there is a fraction, c, of the power in the TE_{11} mode there must be $1-c$ of the power in the TM_{11} mode. ($TE_{11}^y, TM_{11}^y, TE_{11}^x$ and TM_{11}^y are calculated using equations (3.11) to (3.18)). The denominator in equations (2.61) and (2.62) is the total power in the mode. $f_1(c)$ is therefore the fraction of cross-polar power and $f_2(c)$ the fraction of co-polar power. These are plotted, as functions of c in Figure 2.7.
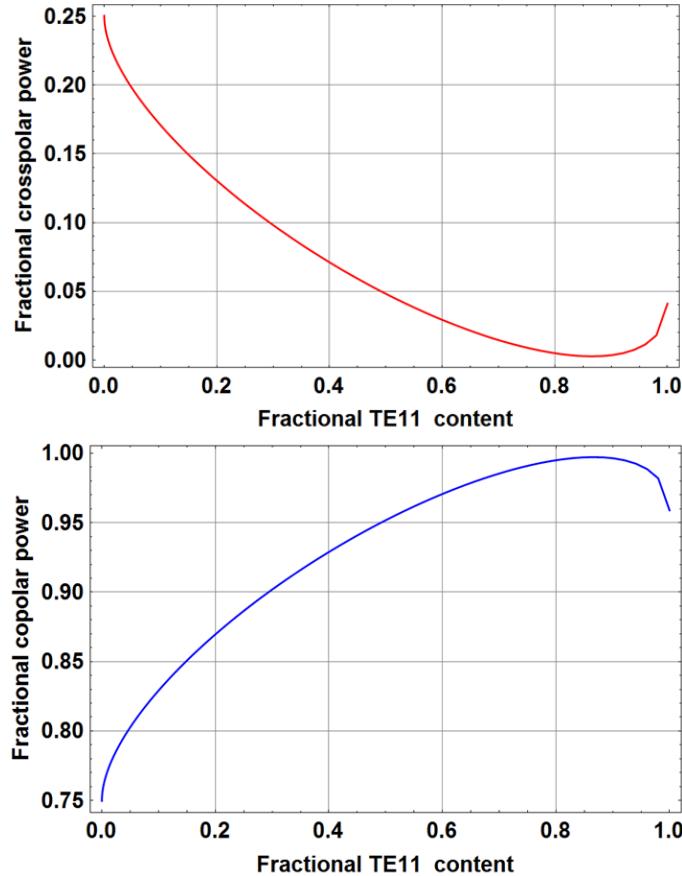

Figure 2.7: Plots illustrating the variation in crosspolar(top) and copolar power with ratio of TE_{11} to TM_{11}

Examining Figure 2.7 it is clear that, even in the worst case the crosspolar content of a HE_{11} mode (made up of TE_{11} and TM_{11} only) is only 25% of the total power, however by choosing the correct ratio of TE_{11} to TM_{11} this can be reduced to around 1% or less. The top plot of this figure shows that the crosspolar content is minimized when the ratio of TE_{11} to TM_{11} power is in the range 0.85 to 0.90, conversely the copolar content is maximized in this scenario, clearly demonstrating that the ideal ratio of TE_{11} to TM_{11} power is in this range.

The original idea of using these two modes to produce the desired radiation pattern in a conical horn was conceived by P. D. Potter in 1963 (23). By using a smooth-walled conical horn, with initially only the TE_{11} mode excited in the throat and a sudden step (as shown in Figure 2.8) he allowed the TM_{11} to cut on (although the TE_{21} mode cuts on before the TM_{11}, no power will couple from a TE_{11} to a TE_{21} as they are of different azimuthal order and are therefore orthogonal). He achieved the desired beam characteristics of side-lobe suppression and beam symmetry in all planes (after allowing the two modes to come into phase).

TM_{11} excited here

Length of phasing section chosen to bring the two modes into phase.

Only TE_{11} can propagate here
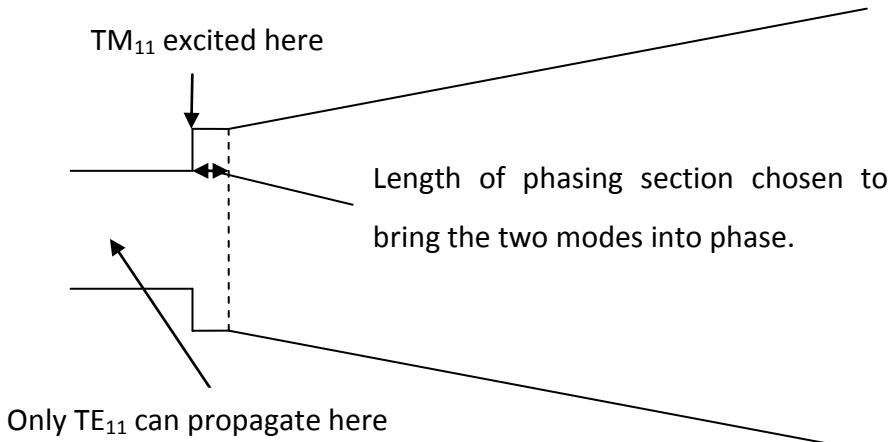
Figure 2.8: Geometry of a Potter horn

This idea was then refined (24) leading to what is now know as the Pickett-Potter horn, where, for ease of construction purposes, the slant length of the horn is used to bring the two modes into phase (Figure 2.9).
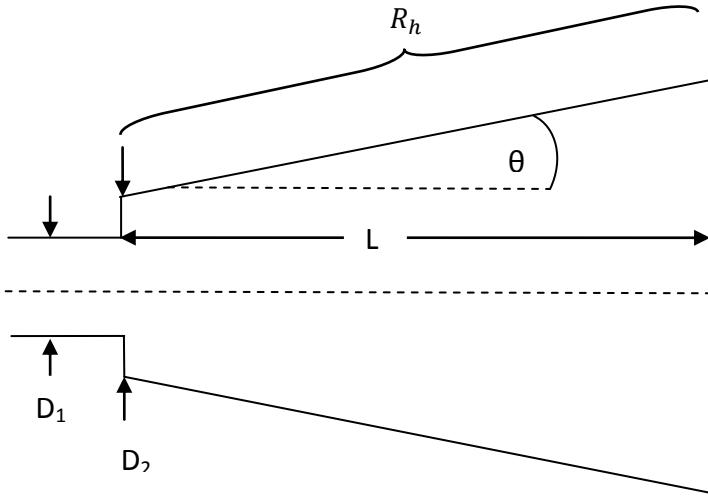
Figure 2.9: Pickett-Potter horn. D_1 = 1.036λ, D_2 = 1.295λ, L = 13.53λ, θ = 15°. θ is known as the flare angle of the horn and R_h is known as the slant length

It is possible to produce an ideal HE$_{11}$ mode using both of these horns, resulting in the field pattern shown in Figure 2.10, however they are limited to operation over a relatively small bandwidth compared to corrugated waveguides/horn antennas.
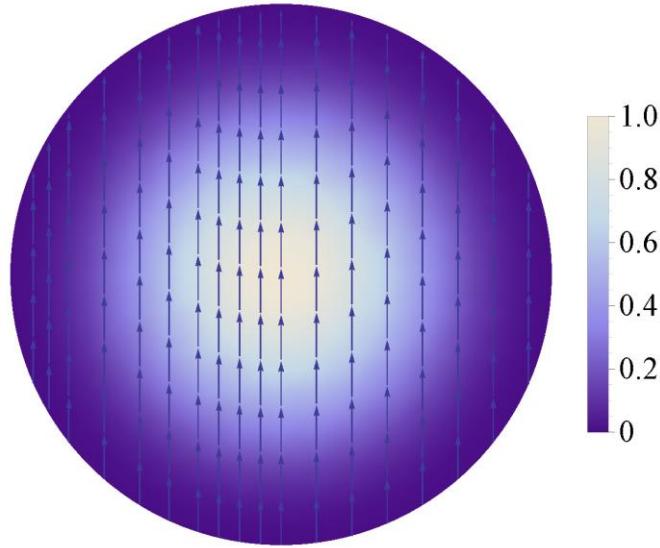
Figure 2.10: Electric field pattern (power (linear) and direction) for an ideal HE$_{11}$ mode. Plotted using equation (2.63) (25) with R_h set to 70 mm and λ set to 3 mm.

The electric field of a HE$_{11}$ mode is given by:

$$\vec{E}_{copolar} = J_0\left(\frac{2.405r}{a}\right)\exp\left(\frac{-j\pi r^2}{\lambda R_h}\right) \tag{2.63}$$

$$\vec{E}_{crosspolar} = 0. \tag{2.64}$$

where r is the off-axis distance, a is the aperture radius of the horn and R_h is the slant length of the horn.

2.3.3 **Corrugated waveguides**

Another, more broadband way to produce a HE_{11} mode is by adding corrugations to the inner wall of a circular waveguide (Figure 2.11). These corrugations, when designed correctly, can have the effect of creating equal boundary conditions for the electric and magnetic fields of an EM-wave, as will be discussed further in chapter 3, this leads to generation of a HE_{11} mode.
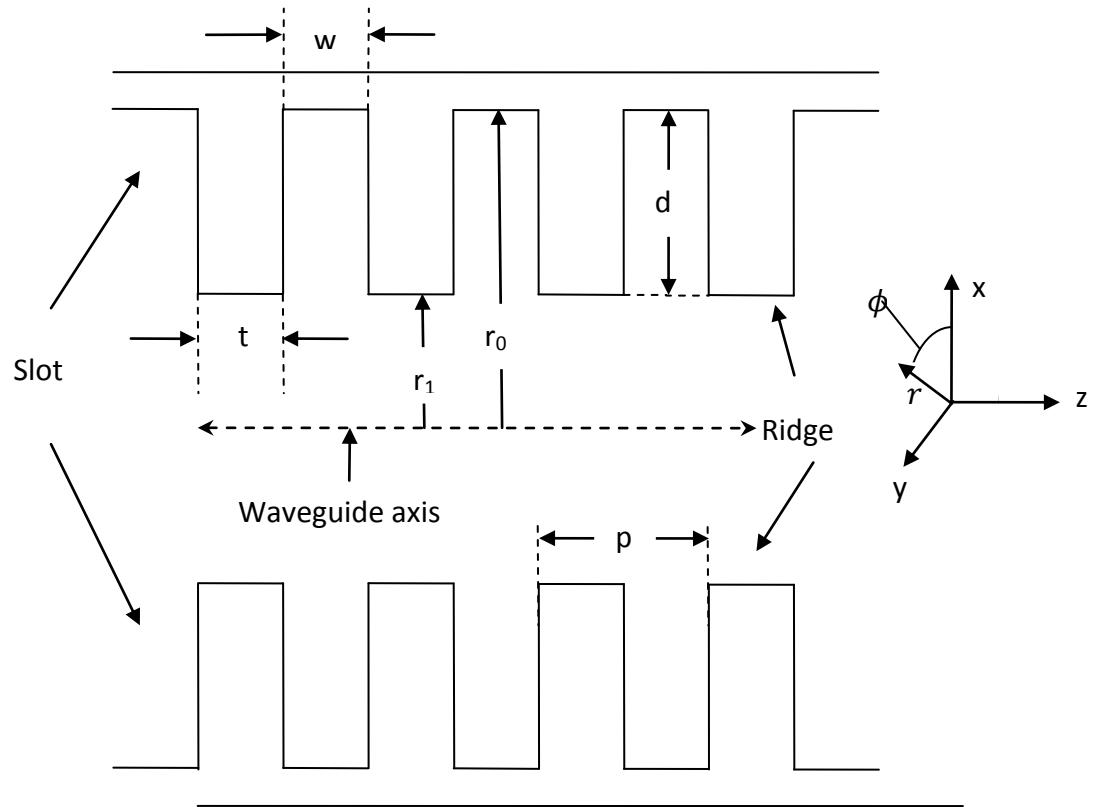
Figure 2.11: Corrugated waveguide geometry.

To understand how an EM wave propagates inside such a structure is not as simple as the previously described smooth-walled waveguide; the non-uniform boundary conditions due to the corrugations make the electric and magnetic field equations more difficult to derive in a corrugated waveguide. A derivation of the propagation equation for modes in such a guide is given in the appendix of(22). Various methods of analysing corrugated cylindrical waveguides will be discussed in chapter 3.

2.4 Summary

This chapter began with an introduction to the concept of waveguides as carriers of EM signals at wavelengths which are too small for standard circuitry due to limitations in the size of the circuits, yet too large to carry useful amounts of power via free-space propagation, due to diffraction. A detailed derivation of the properties of EM-fields in circular waveguides was given next, leading to the formulae for the TE and TM modes and their characteristics such as cut-on frequency, guide-wavelength and wave-impedance. The TE and TM modes of rectangular waveguides and their characteristics were described after this.

The use of waveguides as high-gain antennas (horn antennas) was then discussed, pointing out how the guide-wavelength must be made to match the free-space wavelength at the horn aperture in order to match the impedance at this point. Hybrid modes were then introduced as linear combinations of coherent TE and TM modes with emphasis placed on the HE_{11} mode, which has the desirable properties of rotational symmetry, on-axis power and linear-polarization. An analysis of the optimum ratio of TE_{11} to TM_{11} (85:15) for minimum cross-polarization was performed, resulting in the curves shown in Figure 2.7. The Potter horn and Pickett-Potter horn were then described as horns capable of generating a HE_{11} mode over small bandwidths. A simple equation describing an ideal HE_{11} mode at the aperture of a horn was then given along with a 2-dimensional plot of this mode. Finally corrugated waveguides were introduced as a more broadband way to generate a HE_{11} mode. These waveguides are the subject of the next chapter.

3. Conical horn analysis methods

In this chapter I will give a description of the various mathematical and computational techniques that I used for the analysis and design of corrugated horn antennas. There will first be a discussion of the surface impedance model which leads to formulation of the hybrid mode field equations and a characteristic equation for the propagation coefficients of these modes. Following this will be a description of the mode matching technique which was used most often for designing the horns due to its computational efficiency and relative simplicity. Finally the software package Computer Simulation Technology: Microwave Studio (CST) (26), which uses the finite element technique to model structures interacting with electromagnetic radiation, will be examined.

3.1 The surface impedance model

The surface impedance model of corrugated waveguides is useful for gaining an approximate understanding of how corrugations affect the electromagnetic fields inside the waveguide and for predicting radiation patterns. It works when there are enough corrugations per wavelength (3 or more is usually enough), so that the corrugated surface creates an anisotropic-impedance at the waveguide walls, and when the horn has a constant flare angle, or linear profile. It is also assumed that only the lowest order TM mode can exist in the slots. The azimuthal component of the reactance X_ϕ is approximately 0, i.e. the ridges look like a perfectly conducting surface in the azimuthal-direction, the longitudinal component of the reactance X_z depends on the depth of the slots and the size of the inner radius, r_1 in Figure 2.11. These boundary conditions lead to solutions for the fields which are ϕ independent. According to (27) the boundary conditions can also be stated as

$$\vec{E}_\phi = 0 \tag{3.1}$$

$$\frac{\vec{H}_\phi}{\vec{E}_z} = -\frac{1}{jX_z} \; at \; r = r_1 \tag{3.2}$$

where,
$$jX_z = jZ_0 \tan(kd)\left(1 - \frac{t}{p}\right) \tag{3.3}$$

and d, r_1, t and p are as shown in Figure 2.11.

To achieve beam symmetry in both principal planes we would also like $\vec{E}_r = 0$ at the waveguide walls. From equations (2.32) and (2.28) we know that $\vec{E}_r$ for a TE mode is a function of the $\vec{H}_z$ component only and for a TM mode is a function of $\vec{E}_z$ only. However since the corrugations allow only TM modes to be present at the walls $\vec{E}_r$ in a slot is controlled completely by $\frac{\partial \vec{E}_z}{\partial r}$ which at the top of the slots is proportional to the $\vec{H}_\phi$ of a TM mode. This is expressed in (3.4):

At $$r = r_1$$

$$\vec{E}_r \sim \vec{H}_\phi \sim \frac{\partial \vec{E}_z}{\partial r}$$

(3.4)

Also, from (3.2)

$$\vec{H}_\phi = -\frac{\vec{E}_z}{jX_z}$$

Examining equation (3.3) it is clear that when $d = \frac{\lambda}{4}$, $X_z \to \infty$ making $\vec{H}_\phi \to 0$. Now $\vec{H}_\phi$, $\vec{E}_\phi$ and $\vec{E}_r$ are all zero in the slots. This is known as the open-circuit condition, as in the theory of transmission lines any circuit element providing infinite reactance is called an open-circuit. Under this condition the azimuthal components of the electric and magnetic fields see similar boundary conditions and show a smooth beam edge-taper leading to desirable axial beam symmetry with low side-lobes and low cross-polarization. In general it is also assumed that the slot width is larger than the ridge width ($w > t$) in order to reduce frequency sensitivity, however as will be discussed in Chapter 4, in the narrow part of the horn this isn't always necessarily the best arrangement.

3.1.1 Hybrid mode analysis

Following on from the previous assumptions it is possible to treat a linear combination of TE and TM modes as a single hybrid mode. The longitudinal components of both sets of orthogonal mode for the electric and magnetic fields can be written as in (22).

$$\vec{E}_z = a_m J_m(k_T r) \begin{pmatrix} \cos(m\phi) \\ \sin(m\phi) \end{pmatrix} e^{-j\beta z}$$

(3.5)

$$\vec{H}_z = \frac{a_m}{Z_0} \overline{\Lambda} J_m(k_T r) \begin{pmatrix} \sin(m\phi) \\ -\cos(m\phi) \end{pmatrix} e^{-j\beta z} \qquad (3.6)$$

where $\overline{\Lambda}$ is known as the normalised hybrid factor and measures the relative strengths of TE to TM components of the hybrid modes. A hybrid mode is said to be balanced when $\overline{\Lambda} = \pm 1$, meaning that the conditions leading to $X_z \to \infty$ have been met (if X_z is non-zero hybrid modes can propagate and when X_z is infinite we get balanced hybrid modes). Solving for the transverse field components using these two values of $\overline{\Lambda}$ leads to two sets of modes corresponding to these values. When $\overline{\Lambda} = 1$ we call the modes HE$_{mn}$ and when $\overline{\Lambda} = -1$ we call them EH$_{mn}$. The majority of the work done for this thesis involved so-called "single-moded" horns where only one hybrid mode is propagating (namely the HE$_{11}$ mode), for this reason I will only describe the transverse fields for the HE$_{1n}$ and EH$_{1n}$ modes as written by (27):

HE$_{1n}$ modes:

$$\vec{E}_t =$$

$$-\frac{jka}{u_{0n}} A \left[J_0 \left(\frac{r}{a} u_{0n} \right) \vec{\imath}_x + \frac{1}{4} u_{0n}^2 \frac{y}{ka} J_2 \left(\frac{r}{a} u_{0n} \right) \cdot \left(\cos(2\phi) \vec{\imath}_x + \sin(2\phi) \vec{\imath}_y \right) \right] e^{-j\beta z} \qquad (3.7)$$

EH$_{1n}$ modes: $\qquad (3.8)$

$$\vec{E}_t = -\frac{jka}{u_{2n}} A \left[J_2 \left(\frac{r}{a} u_{2n} \right) \left(\cos(2\phi) \vec{\imath}_x + \sin(2\phi) \vec{\imath}_y \right) \right] e^{-j\beta z}$$

where u_{0n} are the (n = 1, 2, 3...n) roots of J_0 and u_{2n} are the (n = 1, 2, 3...n) roots of J_2. In this case $y = -\frac{Z_0}{X_z}$ so now the condition that $X_z = \infty$ forces $y = 0$. Examination of (3.7) shows that this eliminates the cross-polar ($\vec{\imath}_y$) component of the HE field. The characteristic equation for the propagation constant β (assuming no space-harmonics, i.e. only the fundamental TM mode) as given by (22) can be used to plot dispersion curves for the hybrid modes. This equation is

$$F_m(Kr_1) - \frac{(m\bar{\beta})^2}{F_m(Kr_i)} = \left(\frac{Kr_i}{kr_i} \right)^2 S_m(kr_i, kr_o) \qquad (3.9)$$

where

$$K = \sqrt{k^2 - \beta^2},$$

$$\bar{\beta} = \frac{\beta}{k},$$

r_i and r_o are the inner and outer radii, respectively, and

$$S_m(x, y) = x \frac{J_m'(x)Y_m(y) - J_m(y)Y_m'(x)}{J_m(x)Y_m(y) - J_m(y)Y_m(x)}.$$

In order to determine the hybrid modes that are able to propagate in a particular corrugated horn, r_i and r_o values for the narrowest part of the structure (filter section) can be used (see Figure 3.1). Equation (3.9) was solved using the half interval search method to find allowed values of kr_i at a given βr_i. Plotting βr_i against kr_i shows how many modes can propagate for a given frequency. Each mode will have a unique dispersion pattern (relationship between β and k). An example of such dispersion curves is shown in Figure 3.2:
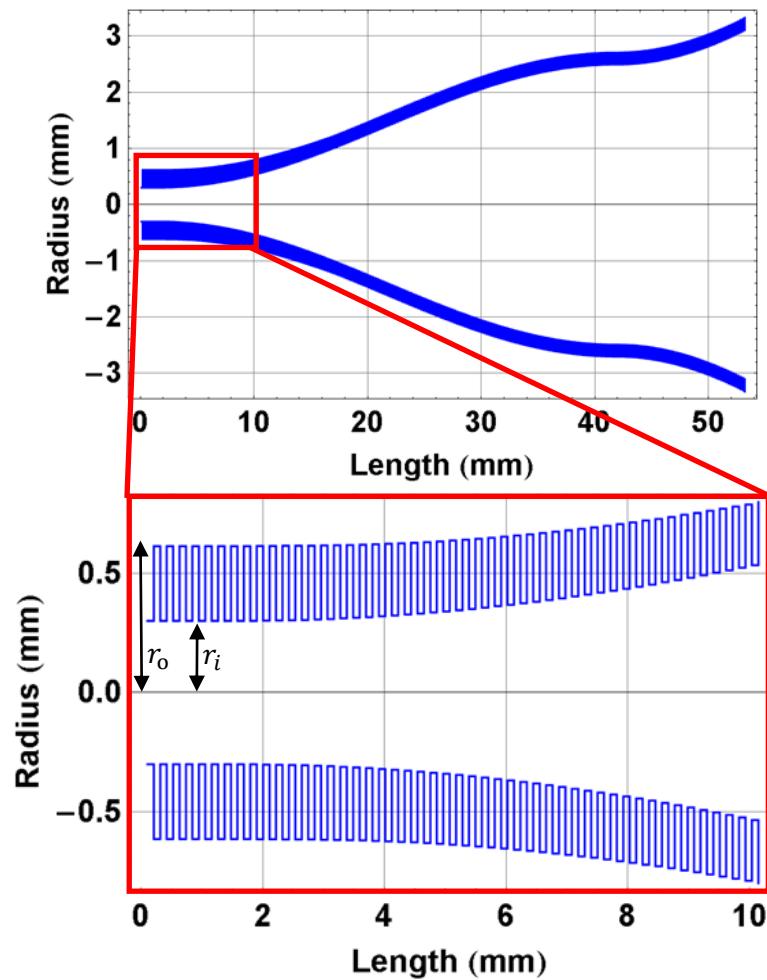

Figure 3.1: Geometry of Planck 353 GHz horn.

An analysis of the 353-GHz channel of the Planck Surveyor HFI (high frequency instrument) was performed using this method to determine whether the horn for this channel was single- or multi-moded across its frequency band of operation. The

term multi-moded means more than one hybrid mode is propagating. Multi-mode antennas can produce an antenna reception pattern close to a top-hat function and are desirable in many applications due to their high sensitivity/ higher power throughput.
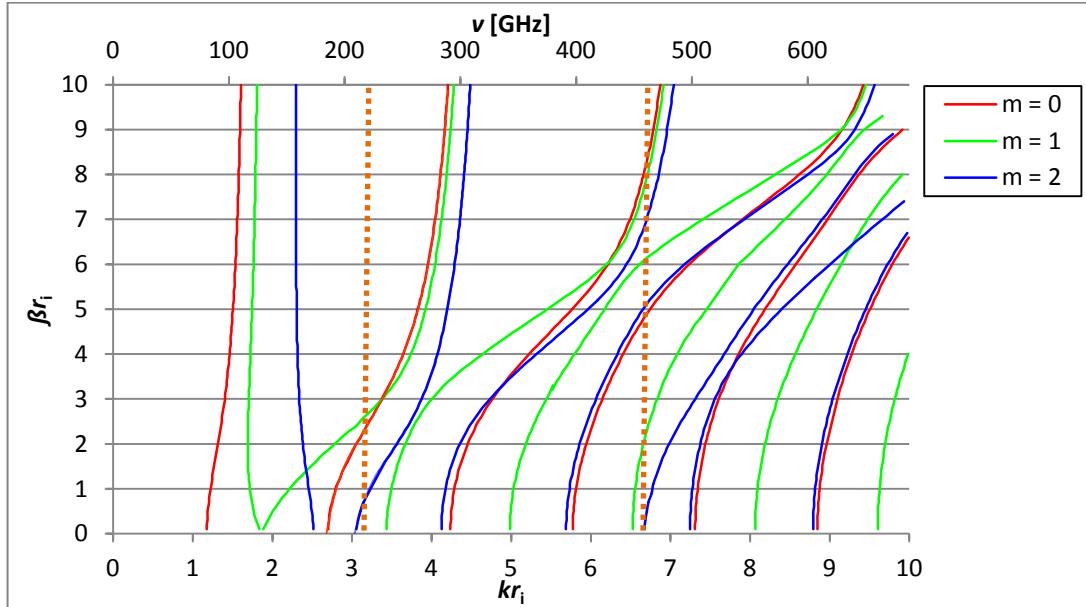

Figure 3.2: Dispersion curves for the Planck 353 GHz channel m is the azimuthal order of a mode. Dashed orange lines show the edges of the band. (This plot was done in conjunction with Stephen Scully of Maynooth University).

Figure 3.2 shows the results for the 353 GHz channel of the ESA Planck Surveyor, which was a mission to measure the cosmic microwave background radiation. According to the hybrid mode model a varying number of modes will propagate at different frequencies in the band, a total of 10 modes can propagate, with the maximum number of 7 propagating modes occurring at approximately 460 GHz. The hybrid mode model is quick and very useful for the initial stages of horn design and verification. In order to fully account for more complex horn profiles, however, other more detailed methods should be used. These are described next.

One interesting thing to note from these dispersion diagrams is that unlike smooth-walled horns (see e.g. (2.59)), corrugated horns have a high frequency cut off as well a low frequency cut off, which makes them better filters than smooth-walled horns.

3.2 Mode matching: SCATTER

A very powerful method for analysing corrugated horn antennas is the mode-matching technique, also known as eigenmode expansion. It is advantageous over the surface impedance approach as it does not need to make the same assumptions about the number of sections per wavelength and it can take account of profiled horns. It can be applied either to rectangular or circular, smooth-walled or corrugated horns; the technique is the same for rectangular and circular geometries. However, as the equations governing the fields in each are different, only one geometry can be simulated at a time. I will describe it in terms of a cylindrical horn as this was the main geometry of interest for this thesis. At Maynooth University the in-house mode matching software is called SCATTER. The original code written to perform mode matching analysis on cylindrical horns was written by Ruth Colgan (28) in Wolfram Mathematica version 3.0, this was then updated for efficiency by Emily Gleeson (29) in Mathematica 6.1, since than it has also been written in Matlab and C. The version used by the author was in Mathematica version 9.0. In essence this method models a horn as a series of alternating cylindrical waveguides of very short length (Figure 3.3). At each discontinuity (change in waveguide radius) power will scatter between various reflected and transmitted TE and TM modes; this scattering can be modelled using a scattering matrix approach, as described by (30).
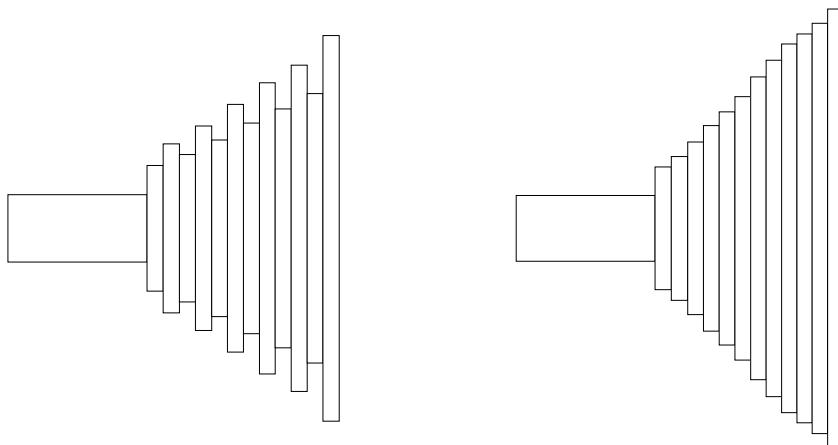

Figure 3.3: Corrugated (left) and smooth-walled (right) horn antennas modelled using a series of alternating cylinders

3.2.1 Mode normalisation and conversion to Cartesian coordinates

The principle of mode matching requires that the total complex power at a scattering junction is conserved; this requirement can be used to find exact solutions to the transverse modal field equations. By setting $\int \vec{E} \times \vec{H}^* \, \overrightarrow{dS} = 1$, where $\vec{E} \times \vec{H}^*$ is the Poynting vector and gives the magnitude and direction of energy flow at any point in the waveguide, the complex power is normalised to unity over a cross-section of the waveguide.

Since cross-polarization is something antenna designers are very interested in it makes sense to write the modal equations in terms of Cartesian coordinates as opposed to cylindrical polar coordinates which have been used until now. Using the transformation relations given in (3.10) and the above normalisation condition the Cartesian components of the transverse modal fields (given in (2.38) to (2.45)) used for mode matching are given in (3.11) to (3.18), see e.g. (29).

$$y = r\sin(\phi)$$
$$x = r\cos(\phi)$$
(3.10)

TE$_{nl}$ modes

$$
\vec{E}_{0x} = \sqrt{\frac{|Z_{nl}^{TE}|(2 - \delta_{n0})}{4\pi a^2 \left(1 - \left(\frac{n}{p_{nl}}\right)^2 J_n^2(p_{nl})\right)}} \left(J_{n-1}\left(\frac{p_{nl}r}{r_a}\right) \begin{bmatrix} \cos\left((n-1)\phi\right) \\ -\sin((n-1)\phi) \end{bmatrix} \right.
$$
$$
\left. + J_{n+1}\left(\frac{p_{nl}r}{r_a}\right) \begin{bmatrix} \cos\left((n+1)\phi\right) \\ -\sin((n+1)\phi) \end{bmatrix} \right)
$$
(3.11)

$$
\vec{E}_{0y} = \sqrt{\frac{|Z_{nl}^{TE}|(2 - \delta_{n0})}{4\pi a^2 \left(1 - \left(\frac{n}{p_{nl}}\right)^2 J_n^2(p_{nl})\right)}} \left(J_{n-1}\left(\frac{p_{nl}r}{r_a}\right) \begin{bmatrix} \sin\left((n-1)\phi\right) \\ \cos((n-1)\phi) \end{bmatrix} \right.
$$
$$
\left. + J_{n+1}\left(\frac{p_{nl}r}{r_a}\right) \begin{bmatrix} \sin((n+1)\phi) \\ \cos((n+1)\phi) \end{bmatrix} \right)
$$
(3.12)

$$\vec{H}_{0x} = \sqrt{\frac{2 - \delta_{n0}}{|Z_{nl}^{TE}|4\pi a^2 \left(1 - \left(\frac{n}{p_{nl}}\right)^2 J_n^2(p_{nl})\right)}} \left(J_{n-1}\left(\frac{p_{nl}r}{r_a}\right)\begin{bmatrix}\sin((n-1)\phi)\\ \cos((n-1)\phi)\end{bmatrix} \right.$$
$$\left. + J_{n+1}\left(\frac{p_{nl}r}{r_a}\right)\begin{bmatrix}\sin((n+1)\phi)\\ \cos((n+1)\phi)\end{bmatrix}\right)$$

(3.13)

$$\vec{H}_{0y} = \sqrt{\frac{(2 - \delta_{n0})}{|Z_{nl}^{TE}|4\pi a^2 \left(1 - \left(\frac{n}{p_{nl}}\right)^2 J_n^2(p_{nl})\right)}} \left(J_{n-1}\left(\frac{p_{nl}r}{r_a}\right)\begin{bmatrix}\cos((n-1)\phi)\\ -\sin((n-1)\phi)\end{bmatrix} \right.$$
$$\left. + J_{n+1}\left(\frac{p_{nl}r}{r_a}\right)\begin{bmatrix}\cos((n+1)\phi)\\ -\sin((n+1)\phi)\end{bmatrix}\right)$$

(3.14)

TM$_{nl}$ modes

$$\vec{E}_{0x} = \sqrt{\frac{|Z_{nl}^{TM}|(2 - \delta_{n0})}{4\pi a^2 \left(J_{n+1}^2(p_{nl})\right)}} \left(J_{n-1}\left(\frac{p_{nl}r}{r_a}\right)\begin{bmatrix}\cos((n-1)\phi)\\ -\sin((n-1)\phi)\end{bmatrix} \right.$$
$$\left. - J_{n+1}\left(\frac{p_{nl}r}{r_a}\right)\begin{bmatrix}\cos((n+1)\phi)\\ -\sin((n+1)\phi)\end{bmatrix}\right)$$

(3.15)

$$\vec{E}_{0y} = \sqrt{\frac{|Z_{nl}^{TM}|(2 - \delta_{n0})}{4\pi a^2 \left(J_{n+1}^2(p_{nl})\right)}} \left(J_{n-1}\left(\frac{p_{nl}r}{r_a}\right)\begin{bmatrix}\sin((n-1)\phi)\\ \cos((n-1)\phi)\end{bmatrix} \right.$$
$$\left. + J_{n+1}\left(\frac{p_{nl}r}{r_a}\right)\begin{bmatrix}\sin((n+1)\phi)\\ \cos((n+1)\phi)\end{bmatrix}\right)$$

(3.16)

$$\vec{H}_{0x} = \sqrt{\frac{2 - \delta_{n0}}{|Z_{nl}^{TM}|4\pi a^2 \left(J_{n+1}^2(p_{nl})\right)}} \left(J_{n-1}\left(\frac{p_{nl}r}{r_a}\right)\begin{bmatrix}\sin((n-1)\phi)\\ \cos((n-1)\phi)\end{bmatrix} \right.$$
$$\left. + J_{n+1}\left(\frac{p_{nl}r}{r_a}\right)\begin{bmatrix}\sin((n+1)\phi)\\ \cos((n+1)\phi)\end{bmatrix}\right)$$

(3.17)

$$\vec{H}_{0y} = \sqrt{\frac{(2 - \delta_{n0})}{|Z_{nl}^{TM}|4\pi a^2 \left(J_{n+1}^2(p_{nl})\right)}} \left(J_{n-1}\left(\frac{p_{nl}r}{r_a}\right)\begin{bmatrix}\cos((n-1)\phi)\\ -\sin((n-1)\phi)\end{bmatrix} \right.$$
$$\left. + J_{n+1}\left(\frac{p_{nl}r}{r_a}\right)\begin{bmatrix}\cos((n+1)\phi)\\ -\sin((n+1)\phi)\end{bmatrix}\right)$$

(3.18)

δ_{n0} is a Kronecker delta function (3.19):

$$\delta_{n0} = \begin{cases} 0, & n \neq 0 \\ 1, & n = 0 \end{cases}$$

(3.19)

3.2.2 Scattering matrix formalisation

At the transition between each cylindrical section of the waveguide, power scattering between modes will take place due to the sudden change in guide-wavelength. This process can be described by a scattering matrix, as will now be shown.

A set of column matrices $[A]$ and $[B]$ contain the transmission and reflection coefficients for the fields coming into a section, similarly $[C]$ and $[D]$ contain the transmission and reflection coefficients for the fields coming out of a section (see Figure 3.4).
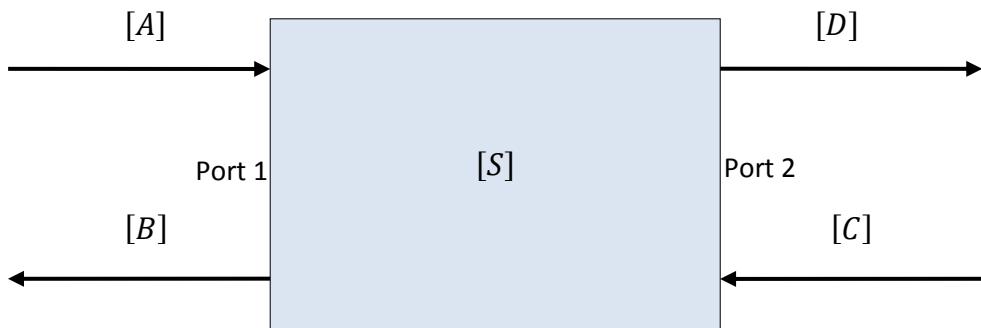
Figure 3.4: Diagram illustrating the relationship between forward and backwards propagating matrices

In Figure 3.4 $[S]$ is called the scattering matrix; each junction has a unique scattering matrix and these matrices can be cascaded to form a single scattering matrix for the whole horn, which can be used to determine its radiation characteristics. The forward and reflected scattering matrices are related in the following way

$$\begin{bmatrix} [B] \\ [D] \end{bmatrix} = [S] \begin{bmatrix} [A] \\ [C] \end{bmatrix}.$$

(3.20)

For a two port system $[S]$ can be written as

$$[S] = \begin{bmatrix} [S_{11}] & [S_{12}] \\ [S_{21}] & [S_{22}] \end{bmatrix}$$

(3.21)

where S_{12} refers to the scattering of power from port 2 to port 1, etc.

The elements of $[S]$ are square matrices containing the power coupling coefficients between all modes at the input with all modes at the output.

Consider the junction in Figure 3.5, for cylindrically symmetric geometries such as this it turns out that we can consider different azimuthal orders independently, as modes of different azimuthal order are orthogonal, meaning no power will couple between them. The scattering matrix $[S_{BA}]$ for the first azimuthal order can then be expressed as shown in (3.22)
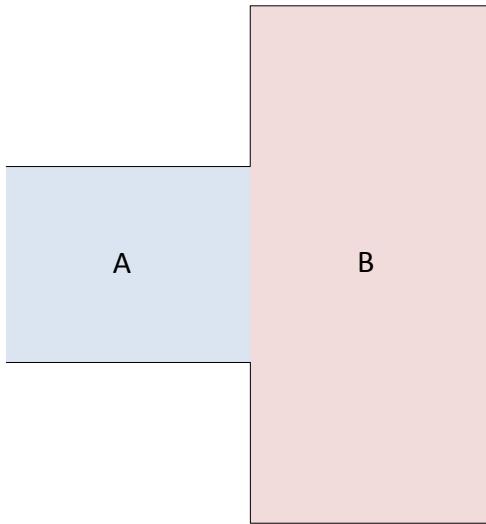

Figure 3.5: Example of a typical waveguide junction

(3.22)

$$[S_{BA}] = \begin{bmatrix} TE_{11,B} \leftarrow TE_{11,A} & TE_{11,B} \leftarrow TE_{12,A} & \cdot & \cdot & TE_{11,B} \leftarrow TM_{11,A} & TE_{11,B} \leftarrow TM_{12,A} & \cdot & \cdot \\ TE_{12,B} \leftarrow TE_{11,A} & TE_{12,B} \leftarrow TE_{12,A} & \cdot & \cdot & TE_{12,B} \leftarrow TM_{11,A} & TE_{12,B} \leftarrow TM_{12,A} & \cdot & \cdot \\ TE_{13,B} \leftarrow TE_{11,A} & TE_{13,B} \leftarrow TE_{12,A} & \cdot & \cdot & TE_{13,B} \leftarrow TM_{11,A} & TE_{13,B} \leftarrow TM_{12,A} & \cdot & \cdot \\ \cdot & \cdot & \cdot & \cdot & \cdot & \cdot & \cdot & \cdot \\ \cdot & \cdot & \cdot & \cdot & \cdot & \cdot & \cdot & \cdot \\ TM_{11,B} \leftarrow TE_{11,A} & TM_{11,B} \leftarrow TE_{12,A} & \cdot & \cdot & TM_{11,B} \leftarrow TM_{11,A} & TM_{11,B} \leftarrow TM_{12,A} & \cdot & \cdot \\ TM_{12,B} \leftarrow TE_{11,A} & TM_{12,B} \leftarrow TE_{12,A} & \cdot & \cdot & TM_{12,B} \leftarrow TM_{11,A} & TM_{12,B} \leftarrow TM_{12,A} & \cdot & \cdot \\ TM_{13,B} \leftarrow TE_{11,A} & TM_{13,B} \leftarrow TE_{12,A} & \cdot & \cdot & TM_{13,B} \leftarrow TM_{11,A} & TM_{13,B} \leftarrow TM_{12,A} & \cdot & \cdot \\ \cdot & \cdot & \cdot & \cdot & \cdot & \cdot & \cdot & \cdot \\ \cdot & \cdot & \cdot & \cdot & \cdot & \cdot & \cdot & \cdot \end{bmatrix}$$

Each column contains the coupling from a given mode of a particular azimuthal and radial order to every other mode of the same azimuthal order.

The nature of the waveguide mode model means that there could be an infinite number of possible modes to consider in each section (including evanescent modes), clearly this is computationally impossible so the number of modes to be considered is chosen such that a specified amount of the total scattered power is recovered upon addition of the coupling coefficients. Typically for the examples in this thesis 30 modes (1 azimuthal order) were sufficient. Combining (3.20) and (3.21) gives (3.24)

$$\begin{bmatrix} [B] \\ [D] \end{bmatrix} = \begin{bmatrix} [S_{11}] & [S_{12}] \\ [S_{21}] & [S_{22}] \end{bmatrix} \begin{bmatrix} [A] \\ [C] \end{bmatrix}$$

(3.23)

$$\Rightarrow \qquad [B] = [S_{11}][A] + [S_{12}][C], \quad [D] = [S_{21}][A] + [S_{22}][C].$$

At the input of the horn (usually chosen to be the smaller aperture) it is assumed that there is no power flowing from the inside of the horn, so $[C]$ is set to zero. For scattering inside the horn $[C]$ will clearly not be zero. When considering the final scattering matrix the reflection and transmission coefficients are given by $[B] = [S_{11}][A]$ and $[D] = [S_{21}][A]$. The form of the input matrix $[A]$ will vary depending on the excitation to be simulated. Only single moded operation was considered in this work, meaning that the first value in $[A]$ was 1 and all others were 0. In this case the reflection and transmission coefficients are completely characterised by the $[S_{11}]$ and $[S_{21}]$ matrices, respectively.

This approach is useful as scattering matrices produced at consecutive junctions in the horn can easily be cascaded together in the following way (30). Consider two such matrices:

$$[S^a] = \begin{bmatrix} [S_{11}^a] & [S_{12}^a] \\ [S_{21}^a] & [S_{22}^a] \end{bmatrix} \text{ and } [S^b] = \begin{bmatrix} [S_{11}^b] & [S_{12}^b] \\ [S_{21}^b] & [S_{22}^b] \end{bmatrix}$$

(3.24)

The cascaded matrix elements are given by:

$$[S_{11}^c] = [S_{12}^a]\left[[I] - [S_{11}^b][S_{22}^a]\right]^{-1}[S_{11}^b][S_{21}^a] + [S_{11}^a]$$

$$[S_{12}^c] = [S_{12}^a]\left[[I] - [S_{11}^b][S_{22}^a]\right]^{-1}[S_{12}^b]$$

(3.25)

$$[S_{21}^c] = [S_{21}^b]\left[[I] - [S_{22}^a][S_{11}^b]\right]^{-1}[S_{21}^a]$$

$$[S_{22}^c] = [S_{21}^b]\left[[I] - [S_{22}^a][S_{11}^b]\right]^{-1}[S_{22}^a][S_{12}^b] + [S_{22}^b]$$

There are essentially two types of section scattering matrix that need to be considered: 'scattering' along a uniform section and scattering at a discontinuity.

3.2.3 Mode scattering along a uniform section of waveguide

For a uniform section of waveguide power will not scatter between modes, however the power in a particular mode can change depending on whether it has cut on or not. Here it is important to consider a large number of evanescent modes since if the length of the section is very short evanescent modes can still have significant amplitude at the end of the section. The scattering matrix elements are given in (30) as:

$$[S_{11}] = [S_{22}] = [0]$$ (3.26)

$$[S_{12}] = [S_{21}] = [V]$$ (3.27)

where $[V]$ is a $2n \times 2n$ diagonal matrix (n is the number of TE and TM modes) whose diagonal elements are calculated by:

$$V_{mn} = e^{-j\beta_n L}$$ (3.28)

where β_n is the propagation constant for the nth mode being considered and is purely real for propagating modes and purely imaginary for evanescent modes. L is the length of the section.

3.2.4 Mode scattering at a waveguide discontinuity

Any sudden change in the geometry of a waveguide (e.g. Figure 3.6) causes a change in guide wavelength which results in reflections and power scattering

between modes. To calculate this power scattering we need to consider the electric and magnetic fields on either side of the junction (Figure 3.6). These are given by (30) as:

$$\overrightarrow{E_L} = \sum_{n=1}^{N}\left\{A_n e^{-j\beta_n z} + B_n e^{j\beta_n z}\right\}\overrightarrow{e_n} \tag{3.29}$$

$$\overrightarrow{H_L} = \sum_{n=1}^{N}\left\{A_n e^{-j\beta_n z} - B_n e^{j\beta_n z}\right\}\overrightarrow{h_n} \tag{3.30}$$

$$\overrightarrow{E_R} = \sum_{n=1}^{N}\left\{D_n e^{-j\beta_n z} + C_n e^{j\beta_n z}\right\}\overrightarrow{e_n} \tag{3.31}$$

$$\overrightarrow{H_R} = \sum_{n=1}^{N}\left\{D_n e^{-j\beta_n z} - C_n e^{j\beta_n z}\right\}\overrightarrow{h_n} \tag{3.32}$$

where the subscripts L and R indicate the field is on the left or right side of a junction, respectively, N is the number of modes being considered and $\overrightarrow{e_n}e^{\mp j\beta_n z}$ and $\overrightarrow{h_n}e^{\mp j\beta_n z}$ are the transverse fields of the nth mode, positive β_n indicates propagation in the negative z direction and negative β_n indicates propagation in the positive z direction. (We take for the moment the left hand side (LHS) as the narrower of the two sections).
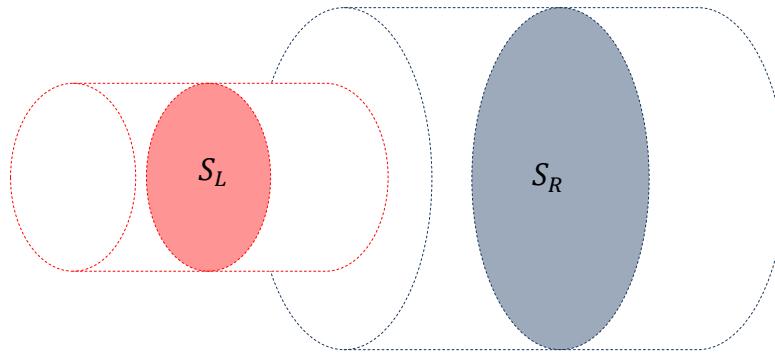

Figure 3.6: Waveguide discontinuity. S_L represents a cross sectional area on the LHS of the junction and S_R an area on the RHS.

Recognizing that the fields must be equal at the interface and setting z to be zero at this position leads to the equations (3.33) and (3.34)

$$\sum_{n=1}^{N} (A_n + B_n)\,\overrightarrow{e_{nL}} = \sum_{n=1}^{N} (C_n + D_n)\,\overrightarrow{e_{nR}} \tag{3.33}$$

$$\sum_{n=1}^{N} (A_n - B_n)\,\overrightarrow{h_{nL}} = \sum_{n=1}^{N} (C_n - D_n)\,\overrightarrow{h_{nR}} \tag{3.34}$$

Taking the electric field on the right side of the junction to be zero outside of the common area ($S_R - S_L$ in Figure 3.6) and considering also the parallel metallic walls and the orthoganality relationship between modes on the same side of the junction leads to the simultaneous matrix equations in (3.35) and (3.36):

$$[P]\big[[A] + [B]\big] = [Q]\big[[C] + [D]\big] \tag{3.35}$$

$$[P]^T\big[[D] - [C]\big] = [R]\big[[A] + [B]\big] \tag{3.36}$$

The elements of $[P]$ (which is an $N \times N$ square matrix) represent the power coupling between modes on either side of the junction and are calculated using equation (3.37)

$$P_{ij} = \int_{S_l} \left(\vec{e}_{iL} \times \vec{h}_{jR}\right)\overrightarrow{dS_L} \tag{3.37}$$

The matrix $[Q]$ is an $N \times N$ diagonal matrix whose diagonal elements are the self coupling between mode on the right hand side o f the junction, these elements are given by equation (3.38)

$$Q_{ij} = \int_{S_l} (e_{iR} \times h_{iR})\,dS_R \tag{3.38}$$

Similarly the matrix $[R]$ is a diagonal matrix whose diagonal elements are given by equation (3.39) and represent the self coupling between mode on the left hand side of the junction.

$$R_{ij} = \int_{S_l} (e_{iL} \times h_{IL})\,dS_L \tag{3.39}$$

From equations (3.35) and (3.36) we can write down what the scattering matrix elements are in terms of $[P], [Q]$ and $[R]$:

$$[S_{11}] = \big[[R] + [P]^T[Q]^{-1}[P]\big]^{-1}\big[[R] - [P]^T[Q]^{-1}[P]\big] \qquad (3.40)$$

$$[S_{12}] = 2\big[[R] + [P]^T[Q]^{-1}[P]\big]^{-1}[P]^T \qquad (3.41)$$

$$[S_{21}] = 2\big[[Q] + [P][R]^{-1}[P]^T]\big]^{-1}[P] \qquad (3.42)$$

$$[S_{22}] = \big[[Q] + [P][R]^{-1}[P]^T\big]^{-1}\big[[Q] - [P][R]^{-1}[P]^T\big] \qquad (3.43)$$

Due to the different forms of TE and TM modes, P_{ij} will be different when considering coupling between TE/TE, TE/TM, TM/TE and TM/TM. This is not a problem for Q_{ij} or R_{ij} as there is no scattering between modes upon reflection since the waveguide radius is constant for incident and reflected modes. Analytical solutions to these integrals are used in SCATTER to increase computational efficiency; these solutions are given in Chapter 3 of (29). It should be noted that these solutions are for propagation from a smaller to larger radius section of waveguide, going from larger to smaller radius (as is the case for every second junction in a corrugated horn) will result in a different scattering matrix, Figure 3.7. However we can consider the case where a > b equivalent to the case when b > a with the radiation propagating in the opposite direction.
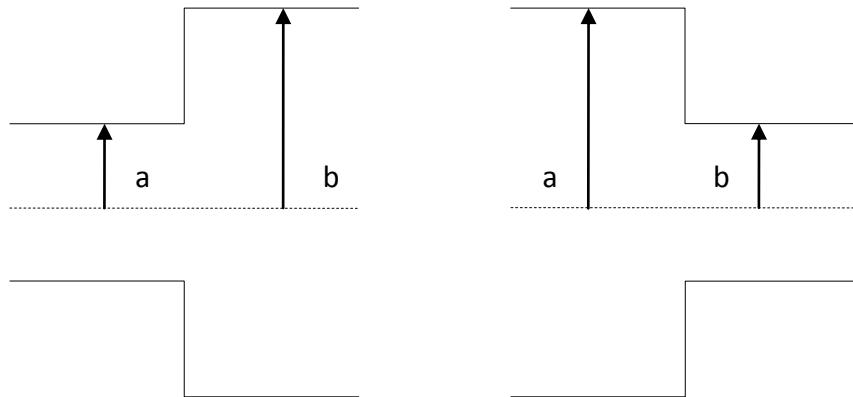

Figure 3.7: Two kinds of junction

3.2.5 SCATTER algorithm.

In this section the main algorithm used by SCATTER will be discussed. The first step in running SCATTER is define a horn's geometry. This is done by creating a list of the

radii and lengths of each cylindrical section. The standard input format adopted is shown in Table 3-1.

Table 3-1: SCATTER Geometry file input format

Line	Column 1	Column 2
1	Operating frequency in GHz	
2	Maximum azimuthal order	
3	Number of sections (N)	
4 → N + 3	Length of nth section	
N + 4 → 2N + 3	Radius of nth section	Number of modes considered for this section

Using this table SCATTER can cascade the scattering matrices from one section to the next in the correct order. The number of modes being considered, *modenum* in the SCATTER code, is split evenly between TE and TM modes with the TE modes making up the first half of the scattering matrix (as in (3.22)).

In order to produce a horn's beam patterns the radiation is considered to be moving from the small aperture to the large aperture. The main SCATTER algorithm can be described in the following steps ('a' and 'b' here will refer to the radius on the left and right side of a junction, respectively):

1. Load in a geometry file. (define total number of section and frequency)

2. This defines the initial radius 'ao' and length 'LLinit'.

3. Populate a diagonal matrix 'VVinit' based on equation (3.28).This represents the scattering along the initial uniform section of the horn.

4. Define initial scattering parameters, $[S_{11}^a], [S_{12}^a], [S_{21}^a]$ & $[S_{22}^a]$, as in equations (3.26) and (3.27).

5. Set $a = b$, set b = radius corresponding to $(index + 1)^{th}$ section, set $dell$ = length corresponding to $(index + 1)^{th}$ section.

6. If{ $a > b$, $rbig$ = a , $rsmall$ = b } else If{ $b > a$, $rbig$ = b, $rsmall = a$}.(Determines left and right sections, bigger is always on the left).

7. Calculate $[P], [Q]$ and $[R]$ for the junction.

8. Calculate the new $[VV]$ for the right-hand section.

9. Calculate $[S_{11}], [S_{12}], [S_{21}]$ & $[S_{22}]$ using equations (3.40) to (3.43) to get $[S]$.

10. Combine this $[S]$ with $[VV]$ to get $[S^b]$ (represents propagation of field through the current section).

11. Cascade $[S^a]$ with $[S^b]$ using equations (3.25) to find $[S^c]$.

12. Set $[S^a] = [S^c]$.

13. Increment 'index'.

14. If{'index' < 'sections-1'; return to step 7} else{exit loop}.

For each azimuthal order

For index = 1 → sections−1

3.2.6   Radiation patterns

Once the preceding algorithm has been completed for all sections of the horn and all azimuthal orders, the modal content at the aperture is known and the aperture field can be calculated using (3.44):

$$E_A(r, \phi) = \sum_{n=1}^{Azi} \sum_{j=1}^{N} \sum_{i=1}^{N} S_{21_{ij}}^n (E_{TE_{ni}}(r, \phi) + E_{TM_{ni}}(r, \phi)) \qquad (3.44)$$

where, Azi is the number of azimuthal orders, N is the number of TE and TM modes and i and j specify the row and column of the $[S_{21}]$ matrix.

The majority of corrugated horn antennas are in what is called single mode operation meaning that only the fundamental HE_{11} hybrid mode will be propagating (this mode can be made up of any number of waveguide section TE and TM modes so long as they are propagating coherently). However at frequencies well above the cut on for the fundamental mode more than one hybrid mode can propagate, as was the case in Figure 3.2 for the Planck 353–GHz horn. Carrying out a singular value decomposition (SVD) of the full scattering matrix to determine its non-zero singular values allows the number of true independent orthogonal fields (i.e. the hybrid HE and EH modes) to be found (see e.g.(31)) The rest of this thesis deals with single mode horns however.

3.3 Finite Integration Technique, CST: Microwave Studio

CST Microwave Studio is a commercially available electromagnetic simulation package based on the finite integration technique (FIT). It is a very powerful, complex package with many capabilities. The only facet of CST used for this work was the antenna simulation tool.

The numerical approach to calculating electric and magnetic field values requires a spatial-discretisation of the element being modelled in order to define a finite calculation domain. In CST this is done by dividing the structure into a series of discrete volume elements called "mesh cells". These can be hexahedral or tetrahedral depending on the solver type. Maxwell's grid equations (32) are then used to calculate the electric voltages and corresponding magnetic fluxes along the edges and through the faces of these shapes, respectively (Figure 3.8). There is also an orthogonal set of mesh cells where the magnetic voltage and electric fluxes are calculated. Consider the integral form of Faraday's law (3.45):

$$\int \vec{E}.d\vec{S} = -\frac{\partial}{\partial t}\iint \vec{B}.d\vec{A}$$
(3.45)

For a mesh cell the closed integral $\int \vec{E}.d\vec{S}$ can be rewritten as the sum of four "grid voltages" $(e_i + e_j - e_k - e_l)$, see Figure 3.8. The magnetic flux on the cell face (b_n) is equal to $\iint \vec{B}.d\vec{A}$, leading to (3.46)

$$e_i + e_j - e_k - e_l = -\frac{\partial}{\partial t} b_n \qquad (3.46)$$
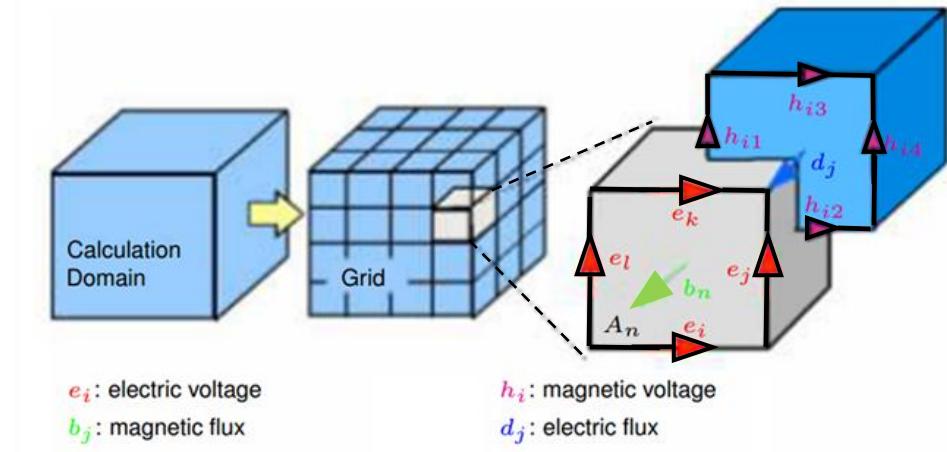
Figure 3.8: CST mesh system. Source: CST documentation centre.

Repeating this for all of the cell faces leads to a matrix formulation as shown in equation (3.47).

$$\begin{pmatrix} \vdots & \vdots & \vdots & \vdots \\ 1 & 1 & -1 & -1 \\ \vdots & \vdots & \vdots & \vdots \end{pmatrix} \begin{pmatrix} e_i \\ e_j \\ e_k \\ e_l \end{pmatrix} = -\frac{\partial}{\partial t} \begin{pmatrix} \vdots \\ b_n \\ \vdots \end{pmatrix} \qquad (3.47)$$

Applying a similar scheme to Ampère's law and Gauss's divergence laws leads to a full set of discretised Maxwell's equations.

3.3.1 Solver Types

CST includes three methods of simulation, or solvers. These are the transient, frequency domain and eigenmode solvers. Transient is a time domain solver, which makes it useful for wideband simulations as the effect of a structure on multiple frequencies can be simulated in a single calculation. Both the transient and frequency domain solvers make use of the Maxwell's grid equations as discussed above, however the transient solver was the only one used in this work.

3.3.2 Setting up a simulation

When setting up a simulation in CST the first step is to create a 3D representation of the structure you wish to model. The CST user interface (UI) allows for the creation of several standard 3D shapes (e.g. brick, sphere cone) and implements

Constructive Solid Geometry for the Boolean addition of shapes, in this way arbitrary shapes can be created. This is done in the modelling tab of the UI.

There are several options for material type, which effectively change the value of μ_r and ϵ_r where the mesh intersects the material of the structure being modelled. However for this work the material was assumed to be a perfect electrical conductor (PEC), which has the properties $\mu_r = 1$, $\epsilon_r = 1$ and $\sigma = \infty$. It is also possible to create an element of vacuum (free-space) which can be Boolean subtracted from another element to create, for example, a hollow brick (Figure 3.9).


PEC brick   PEC brick with vacuum brick   Hollow PEC brick
                   to be subtracted
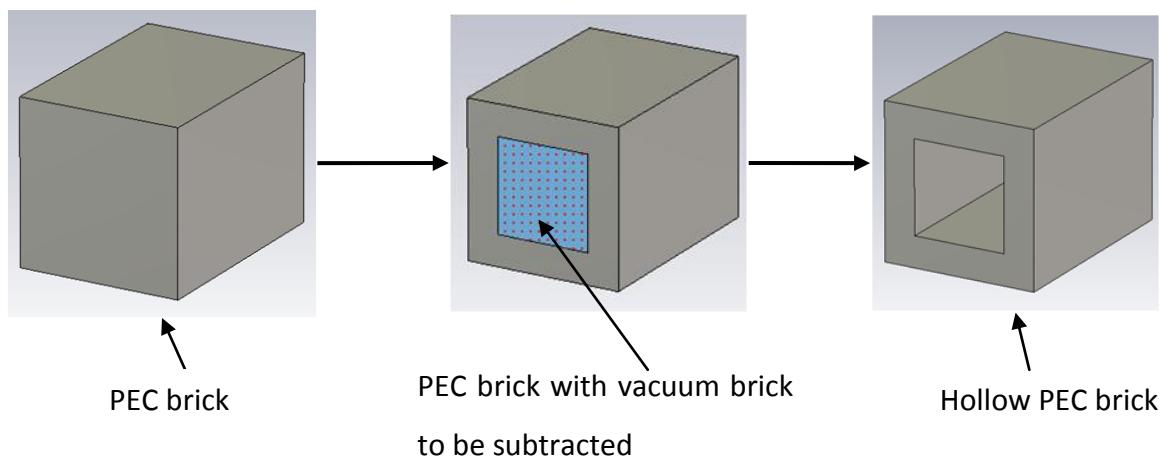
Figure 3.9: Creating a hollow brick in CST

Once the structure has been built in the 3D modeller, a frequency range must be defined before the simulation begins. There are several methods for exciting the structure with an electromagnetic signal. These include plane-wave excitation and excitation at a waveguide port. The waveguide port method works by generating a field comprised of the modes in an infinitely long, lossless waveguide of equivalent geometry at a defined port. Taking the example of the brick in Figure 3.9, two edges of the entrance to the hollow part of the brick are selected, to define the shape of the port. CST allows the properties of the port, such as the number of considered modes, to be chosen and an excitation field will then be generated at this point. A waveguide port is indicated by a 2D plane coloured red, as seen in Figure 3.10.
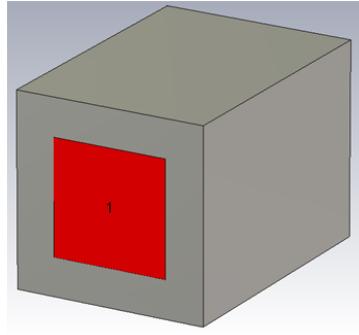
Figure 3.10: Waveguide port shown in red.

The accuracy of a simulation can be greatly affected by the number of sample points, too few and the results will be inaccurate, however choosing too many will increase the run time of the simulation unnecessarily. The number of sample points in CST is the number of mesh-cells being used to represent the structure. This can be altered by the user (the number of lines per wavelength will define the dimensions of the mesh-cells with respect to the highest frequency considered). For structures with very small parts, such as a corrugated horn where the slots and ridges can be less a tenth of a wavelength, it is important to consider many lines per wavelength, typically $20 - 30$. If the accuracy of a simulation is in doubt CST provides an adaptive meshing option whereby the size of the mesh is changed locally by performing multiple runs and reducing the mesh-size until a steady-state, to certain accuracy, is reached. The waveguide port method also naturally allows for S-Parameter calculation, as more than one port can be created.

In order to reduce calculation time it is possible to take advantage of symmetries in a system. Each exploited symmetry reduces the memory requirements by a factor of 2, leading to a reduced computation time. One practical example is a conical horn fed by a rectangular waveguide. This is rotationally symmetric about 180°. We can therefore define two symmetry planes, namely the yz-plane and the xz-plane (see Figure 3.11).
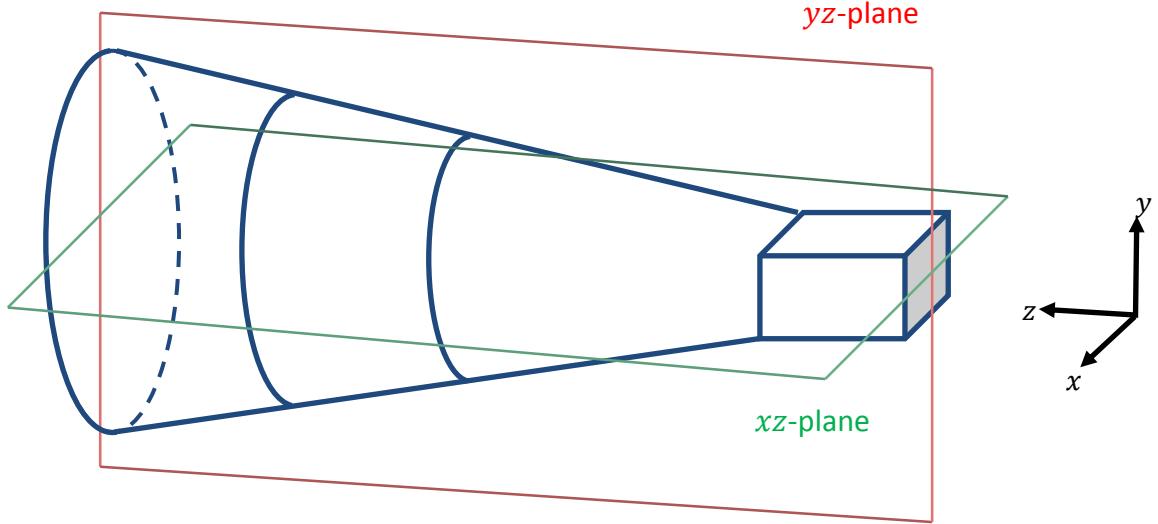
Figure 3.11: Conical horn with rectangular waveguide feed. Symmetry planes shown in red and green

There are two types of symmetry plane: electric boundary and magnetic boundary. Electric fields tangential to, and magnetic fields normal to, an electric boundary symmetry plane go to zero at the plane and are symmetric about the plane. The converse is true for magnetic symmetry. In the case of Figure 3.12, the field in the rectangular WG is y-polarized so we set the xz-plane to have an electric boundary and the yz-plane to have a magnetic boundary. This feature can be accessed in the simulation tab by pressing the boundaries button and in the pop-up menu selecting symmetry planes. An example of setting this up is shown in Figure 3.12).
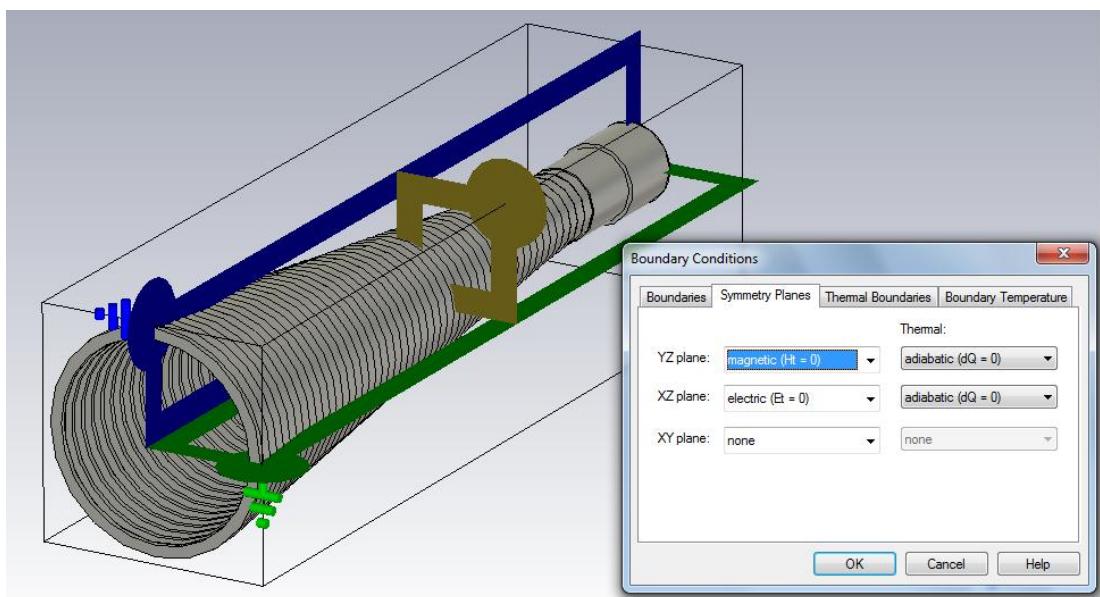

Figure 3.12: Setting up symmetry planes in CST

It is also possible to define certain boundary conditions, and in fact for antenna simulations it is important that an open boundary condition is defined at the aperture to enable far-field calculation.

3.3.3 Field monitors

When modelling an antenna what we are usually most interested in are the properties of the far-field, and near-field (aperture field) of the antenna. In CST these are calculated using 'field monitors'. There are several field monitor options such as far-field, E-field and H-field. For each of these fields the frequency of interest must be specified. The far-field monitor will calculate the far-field radiation pattern as a function of angle, while E-field will calculate the E-field pattern at a user defined plane, this is especially useful for looking at the aperture field of an antenna. In Figure 3.13 the placement of an E-field monitor and resulting simulated field amplitude are shown for a corrugated conical horn.
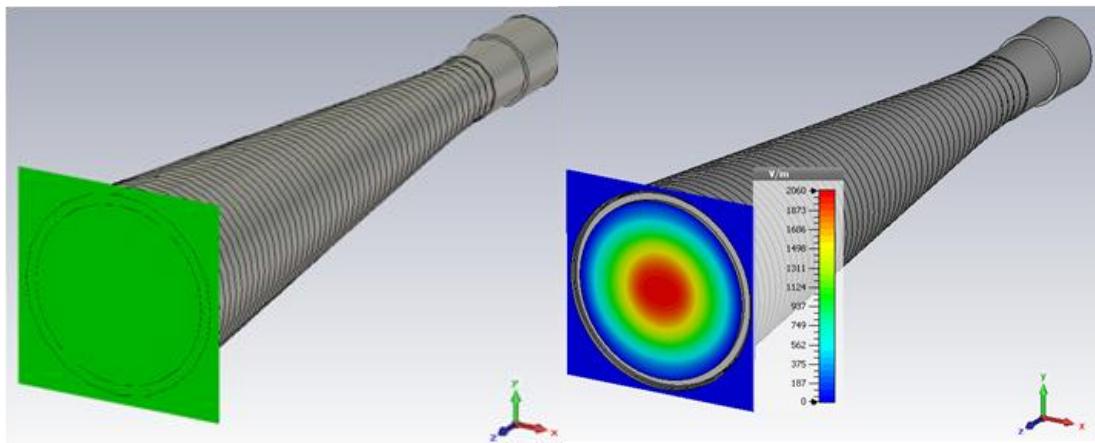

Figure 3.13: Placement of E-field monitor at horn aperture (left) and calculated field (right) in CST for a WR-10 band horn.

To further illustrate the power of CST a field monitor in the yz-plane was set-up for the same horn. This allows us to gain an understanding of not only the power distribution in a corrugated horn, but also the direction of the electric vector field, as seen Figure 3.14.
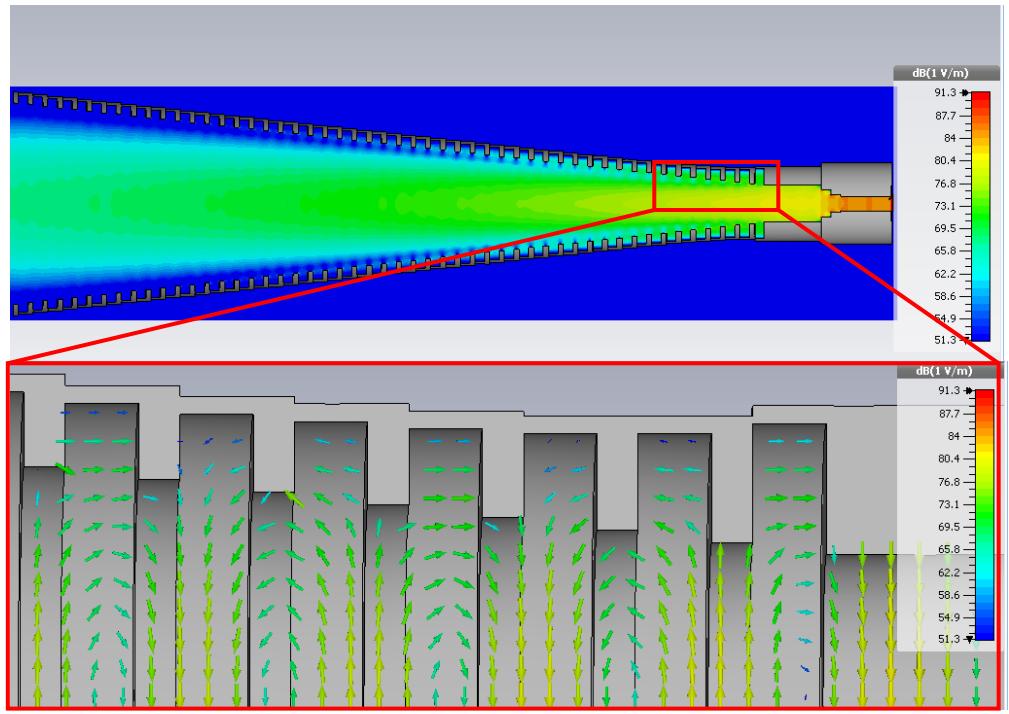
Figure 3.14: Power distribution in the yz-plane (x = 0) (top) and direction of the electric field lines in a corrugated horn (bottom).

3.4 Comparison of SCATTER and CST

Clearly, SCATTER and CST are very different methods of simulation and this is extremely useful for cross-verification of results. SCATTER and CST have been shown to give good agreement in situations where both techniques are applicable, for examples of far-field comparisons see, for example, (33). There is also a comparison of the near-fields calculated for a corrugated conical horn shown in Figure 3.15. The advantages and disadvantages of the two software packages are listed in Table 3-2.

Table 3-2: Comparison of SCATTER and CST

SCATTER	CST
Fast	Slow
Computationally easy	Computationally intensive
Symmetric systems only (current version)	Allows for any shape
One type of geometry (rectangular or circular)	All geometries
In-house	Commercial ("black box")

In summary, for symmetric systems employing only one geometry SCATTER is the preferred choice due to its computational speed. However more complicated asymmetric systems with multiple shapes can be catered for by CST as FIT is a much more general simulation technique.

One of the main advantages of SCATTER is that it is in-house which mean we have access to the code itself and so can have complete control over a simulation and can customise automation and optimization. I have made use of both simulation techniques for the work in this thesis.
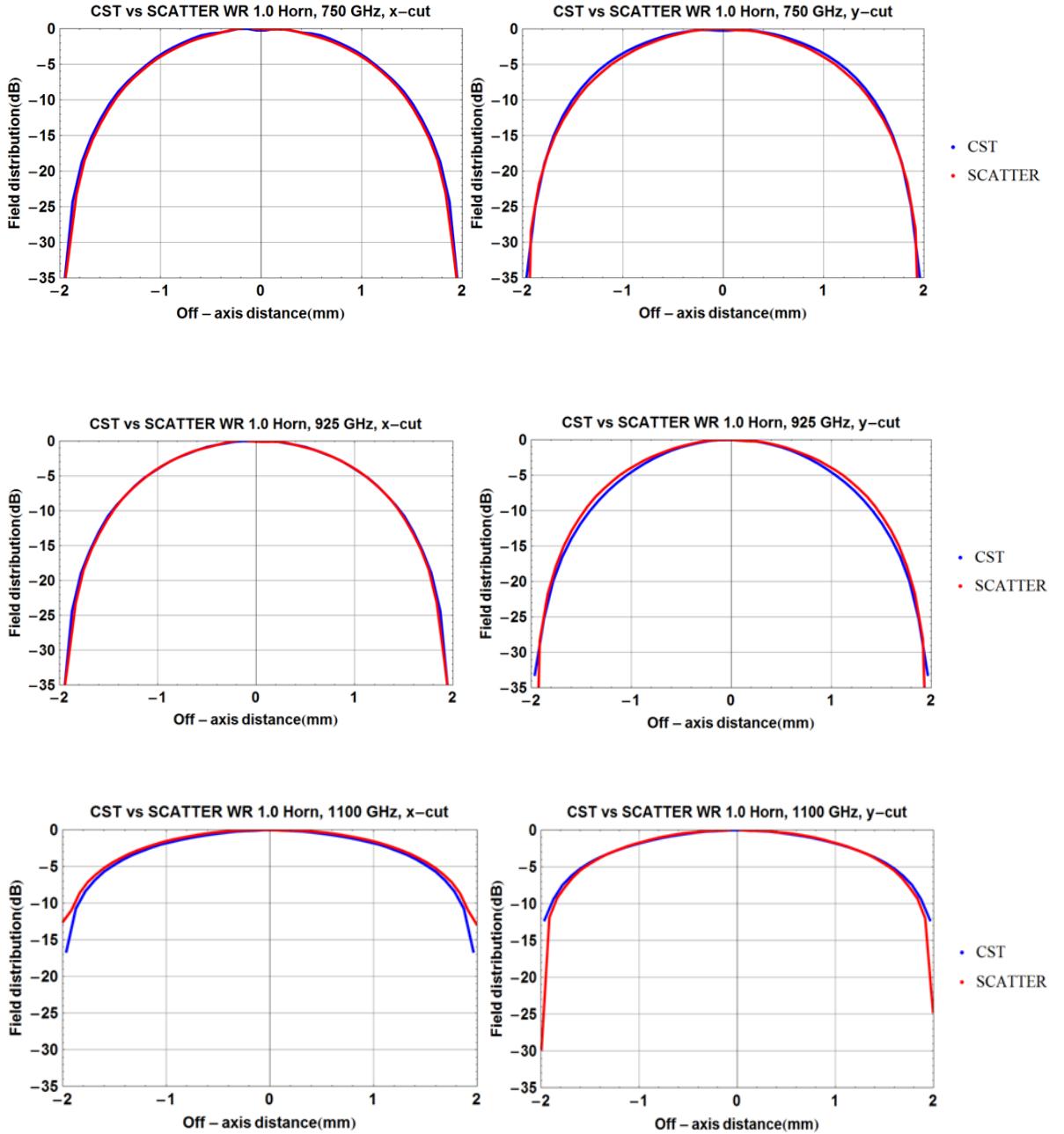

Figure 3.15: SCATTER vs. CST aperture fields for a WR 1.0 horn. (The small discrepancies are likely due to the fact that SCATTER does not account for the step to free-space at the aperture but CST does).

3.5 Summary

In this chapter I have introduced three methods of analysis for corrugated horn antennas. I began by describing the surface impedance model, which treats the corrugation like a uniform surface impedance at the inner walls of a corrugated waveguide or horn antenna. This model allows us to derive a mathematical description for the behaviour of an electric field inside such a corrugated waveguide and provides an explanation as to why choosing quarter-wavelength deep corrugations lead to a desirable on-axis, rotationally symmetric, linearly polarized beam (HE_{11} mode). Using this model it is also possible to calculated the hybrid (HE or EH) mode modal dispersion curves at a given section of a corrugated horn (i.e. specific values of the inner and outer radii (r_i and r_o)). This is an approximate but useful way of determining the number of possible propagating hybrid modes at the narrowest part of a corrugated horn which behaves as a bandpass-filter. An example of this technique was given for the Planck surveyor 353-GHz channel horn antenna.

The second method that was described was the mode-matching technique, specifically in relation to Maynooth University's in-house code, SCATTER. The mode-matching technique is extremely useful for simulating the antenna properties (reflection, transmission and radiation patterns) of corrugated horns. Each section of the horn, i.e. each corrugation, is treated like a waveguide supporting TE and TM modes, these modes will be either reflected or transmitted at the interface between two sections. Power will also be scattered between the modes for the transmitted field. These effects can be modelled using a two-port scattering matrix approach. The method used by SCATTER for these simulations was outlined in detail and the method of calculating the radiation pattern was given. There was also a brief discussion on simulating a multimode horn using SCATTER using singular value decomposition.

The final simulation approach was the finite integration technique. This is the method used by CST: Microwave Studio, a commercially available electromagnetic simulation software package. There was a description of this technique, as it is employed by CST, followed by an outline of how to set up a simulation. Some of the

capabilities of CST were also discussed, including the usefulness of field monitors. Finally there was a comparison of CST and SCATTER along with their advantages and disadvantages for different situations.

4. Designing corrugated conical horn antennas

In this section I describe much of the work I have done in the design and analysis of corrugated horn antennas, which are used to couple EM radiation from a rectangular waveguide to either free-space or to a large diameter corrugated cylindrical waveguide. There are three main design steps involved, at each step the goal is to couple radiation between two regions with different propagation properties: (1) the transition from rectangular to circular waveguide (2) the transition from circular waveguide to the corrugated horn throat and (3) the transition from throat to aperture (this is the main body of the horn), at this point in the system there will be a transition to either free-space or to a corrugated circular waveguide.

4.1 System design requirements

As discussed in Chapter 1, SWISSto12 would like to manufacture a series of corrugated horn antennas to function as free-space radiators or to be used in conjunction with their material characterisation kits (MCKs). Each horn is to be designed to work across one of the industry standard WR waveguide bands. Table 4-1 describes the properties of the WR bands and corresponding rectangular smooth-walled waveguides which will be referred to as "WR guides".

Table 4-1: WR waveguide bands, frequencies and dimensions. Source: Virginia Diodes (virginiadiodes.com)

Internal Band Designation	EIA Band Designation	Internal Dimensions (mils)	Internal Dimensions (mm)	Frequency Range (GHz)
WR- 51.0	WR- 51	510 x 255	12.954 x 6.477	15.0 - 22.0
WR- 42.0	WR- 42	420 x 170	10.668 x 4.318	17.5 - 26.5
WR- 34.0	WR- 34	340 x 170	8.636 x 4.318	22.0 - 33.0
WR- 28.0	WR- 28	280 x 140	7.112 x 3.556	26.5 - 40.0
WR- 22.4	WR- 22	224 x 112	5.690 x 2.845	33.0 - 50.5
WR- 18.8	WR- 19	188 x 94	4.775 x 2.388	40.0 - 60.0
WR- 14.8	WR- 15	148 x 74	3.759 x 1.880	50.5 - 75.0
WR- 12.2	WR- 12	122 x 61	3.099 x 1.549	60.0 - 90.0
WR- 10.0	WR- 10	100 x 50	2.540 x 1.270	75.0 - 110.0
WR- 8.0	WR- 8	80 x 40	2.032 x 1.016	90.0 - 140.0
WR- 6.5	WR- 6	65 x 32.5	1.651 x 0.826	110.0 - 170.0
WR- 5.1	WR- 5	51 x 25.5	1.295 x 0.648	140.0 - 220.0
WR- 4.3	WR- 4	43 x 21.5	1.092 x 0.546	170.0 - 260.0
WR- 3.4	WR- 3	34 x 17	0.864 x 0.432	220.0 - 330.0
WR- 2.8	n/a	28 x 14	0.711 x 0.356	260.0 - 400.0
WR- 2.2	n/a	22 x 11	0.559 x 0.279	330.0 - 500.0
WR- 1.9	n/a	19 x 9.5	0.483 x 0.241	400.0 - 600.0
WR- 1.5	n/a	15 x 7.5	0.381 x 0.191	500.0 - 750.0
WR- 1.2	n/a	12 x 6	0.305 x 0.152	600.0 - 900.0
WR- 1.0	n/a	10 x 5	0.254 x 0.127	750.0 - 1100.0
WR- 0.8	n/a	8 x 4	0.203 x 0.102	900.0 - 1400.0
WR- 0.65	n/a	6.5 x 3.25	0.165 x 0.083	1100.0 - 1700.0
WR- 0.51	n/a	5.1 x 2.55	0.130 x 0.065	1400.0 - 2200.0

The horns designed in this thesis will be used as part of a vector network analyser (VNA) laboratory measurement system. Measurements at GHz and THz frequencies are often made using VNAs which can measure both the amplitude and phase of an EM wave. VNAs use a port system similar to SCATTER and CST and the measurements are described in terms of S-parameters in exactly the same way.

The VNA itself can generate an oscillating signal (state of the art VNAs can reach up to 40 GHz), however to reach the frequencies of interest a frequency multiplier (frequency extension module) is used to step up the frequency into the correct band. These mixers are designed to operate across the WR frequency bands and output their signal through a rectangular WR waveguide. A fuller description of VNA and frequency extension module operation will be given in chapter 5.

The the VNA frequency extension modules output their signal via rectangular WR guides and therefore the corrugated horns must be connected to these. This is a common transition for many millimetre-wave systems and is usually achieved by connecting the corrugated horn throat to the rectangular WG through a piece of smooth-walled circular WG, as seen in Figure 4.1.
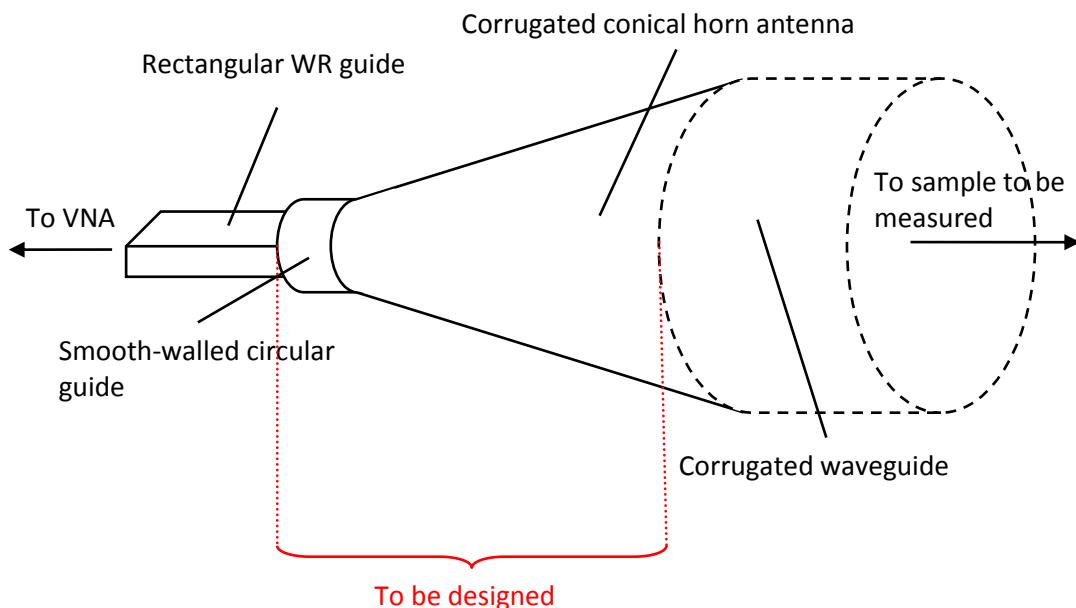

Figure 4.1: Waveguide network to be designed. The dashed cylinder represents the optional corrugated wave, which would be used as part of the material characterisation kit.

From this we can define three design stages as follows:

1. Transition from rectangular to circular smooth walled WG.

2. Transition from circular smooth walled WG to corrugated horn.

3. Transition from small diameter "throat" of horn to larger aperture.

4.1.1   **Design goals**

The design goals for these horns are shown in Table 4-2:

Table 4-2: Design goals for SWISSto12 horns.

Parameter	Goal
Peak S_{11}	< -20 dB across the band
Peak cross-polar power	< -20 dB across the band
HE_{11} modal purity	> 92 % across the band

In some cases only the S_{11} and HE_{11} were examined in detail as performance metrics, this is justified as the HE_{11} is a linearly polarized field and strong coupling to it implies low levels of cross-polarization. There were also some mechanical limitations that needed to be taken into account, such as the manufacturing precision and keeping the horn as short as possible to reduce the building cost. The aperture size was also pre-determined by SWISSto12®, but this was flexible in some cases.

4.2 Rectangular to circular transition

The most critical factor when designing a rectangular to circular transition is the reflection at the junction, which we want to minimize. In electrical engineering the reflection coefficient on a transmission line is written in the following way:

$$|\rho| = \frac{Z_2 - Z_1}{Z_2 + Z_1}$$
(4.1)

where Z_2 is the load impedance and Z_1 is the source impedance.

The reflection coefficient ρ will be minimized when the source and load impedance are equal, they are then said to be 'matched'. The waveguide impedance expressions in (2.49) and (2.50) can be generalized for any shape waveguide to the equations in (4.2):

$$Z_{TE} = \frac{Z_0}{\sqrt{1 - \left(\frac{\lambda}{\lambda_c}\right)^2}} = \frac{Z_0 \lambda_g}{\lambda}$$
(4.2)

59

$$Z_{TM} = Z_0 \sqrt{1 - \left(\frac{\lambda}{\lambda_c}\right)^2} = \frac{Z_0 \lambda}{\lambda_g}$$

where Z_0 is free-space impedance, λ_c and λ_g are cut-on and guide wavelength.

Combining the equations in (4.2) with (4.1) leads to (4.3) (bearing in that mind that only the fundamental modes are being considered here, due to the fact that higher order modes are close to cut-on so not a lot of power will be scattered to them):

$$|\rho| = \frac{\lambda_{g2} - \lambda_{g1}}{\lambda_{g2} + \lambda_{g1}} \tag{4.3}$$

Therefore, in order to minimize reflections at a waveguide junction we want to match the impedance or guide-wavelengths on either side of a junction. This will clearly become more complicated when considering broadband systems propagating multiple modes as there is a non-linear relationship between mode guide-wavelengths and waveguide dimensions.   For this reason only the fundamental TE_{01} rectangular mode and TE_{11} circular mode are considered, which is an oversimplification at higher frequencies but makes a good first approximation.

In practice, guide-wavelength can be expressed in terms of cut-on wavelength, so by matching the cut on wavelengths of these two modes (4.4) we can achieve impedance matching. We set

$$\lambda_c^{\square} = \lambda_c^{\circ},$$

$$\frac{2\pi}{\sqrt{\left(\frac{m\pi}{a}\right)^2 - \left(\frac{n\pi}{b}\right)^2}} = \frac{2\pi r_a}{p'_{xl}} \tag{4.4}$$

where $\lambda_c^{\square}$ and λ_c° are the cut-on wavelengths for rectangular and circular modes ((2.46) & (2.60)), a, b and r_a are as shown in Figure 4.2, m and n are the nearest whole numbers of half wavelengths that fit in the a and b dimensions, respectively and x and l are radial and azimuthal orders of the circular TE modes.

Substituting $m = 1, n = 0$ and $p'_{xl} = 1.84$ (see Table 2-1) which are the values for the fundamental $TE_{01}^{\square}$ and TE_{11}° modes leads to (4.5).

$$r_a = \frac{1.841 a}{\pi} \tag{4.5}$$
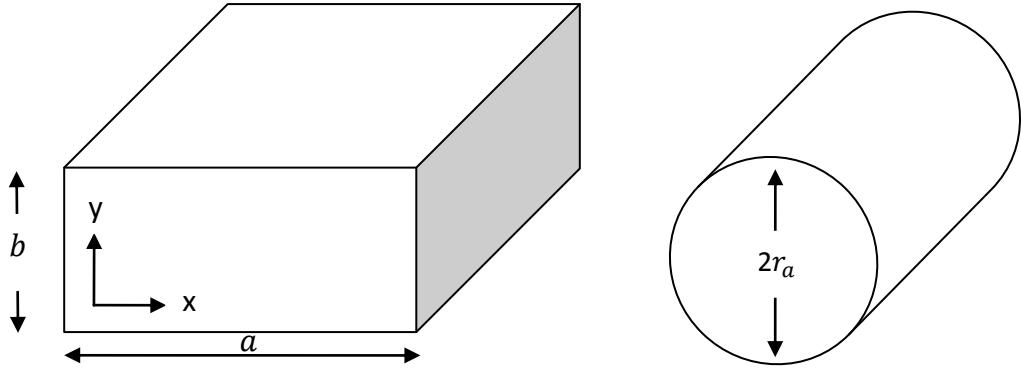
Figure 4.2: Rectangular and circular waveguide geometries.

where a is predefined for a given frequency band as shown in Table 4-1, so the only variable is r_a which can be easily calculated.

4.2.1 Two step transition

Once a first order solution for the transition i.e. the radius of the circular WG has been found there are methods to further improve the impedance matching. Two such techniques will be discussed, the first of which is the two-step transition. This involves placing two non-standard pieces of rectangular waveguide between the WR guide and circular WG of radius r_a, as seen in Figure 4.3.
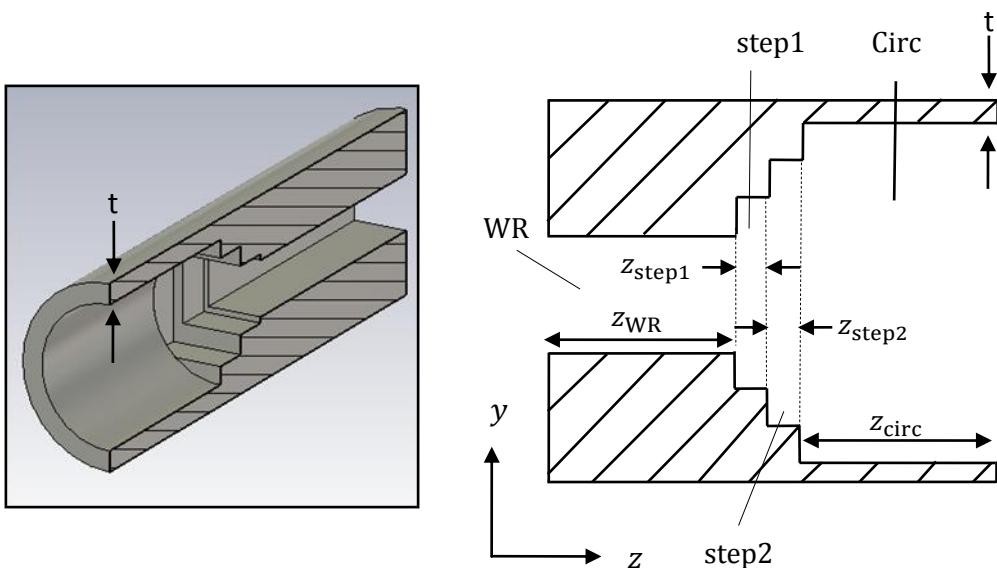

Figure 4.3: Two-step transition in CST (left) and schematic diagram (right).

Simulating a shape like this is not currently possible in SCATTER so this stage of the design was done in CST. Such a structure can be created in CST by first creating a solid cylinder of length $L = z_{\mathrm{WR}} + z_{\mathrm{step1}} + z_{\mathrm{step2}} + z_{\mathrm{circ}}$ and radius of $r_a + t$ where z_{WR}, z_{step1}, z_{step2} and z_{circ} are as shown in Figure 4.3; z refers to the

dimension of the component and t is the thickness of the waveguide walls. This t must be greater than the skin depth of the material being used. We are using a perfect electrical conductor (PEC) for the simulation and the skin depth of a PEC is 0 m, however the real components will stainless steel coated in gold, which has a skin depth on the order of nm at THz frequencies, so t is usually, somewhat arbitrarily, set to be approximately one fifth of a wavelength. Following the method outlined in chapter 3 it is possible to subtract the appropriate shapes from this cylinder. By defining the dimensions of the shapes as variables, in the way shown in Figure 4.4 for example, it is possible in CST to perform a parameter sweep analysis or to implement an optimization for the transition.
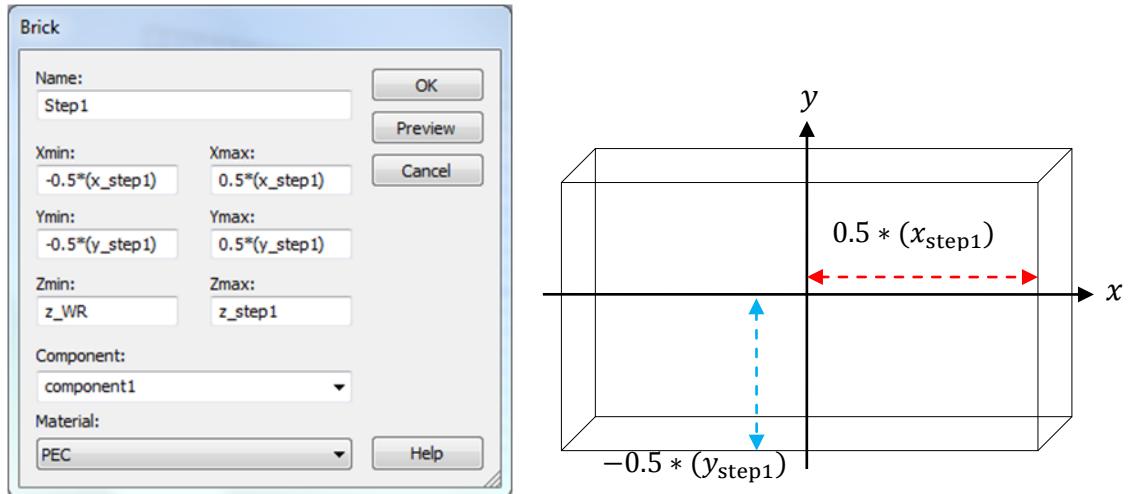

Figure 4.4: Defining a brick using variables in CST, with the centre of the brick on the axis of CST's coordinate system.

The longitudinal dimensions of step1 and step2 were initially chosen to be about a quarter of a guide wavelength at the central frequency of the band. This will have the same effect as the quarter-wavelength films used for anti-reflective coatings. Radiation reflected at the junction between step1 and step2 will be coherent and π radians out of phase with radiation reflected at the $\text{WR} - \text{step1}$ junction, producing destructive interference between the reflected waves at this point. The transverse dimensions are chosen initially so the steps between the WR guide and the circular guide are all equal by using the relationships shown in (4.6).

$$x_{\text{step1}} = x_{\text{WR}} + \frac{r - x_{\text{WR}}}{3}$$

$$y_{\text{step1}} = y_{\text{WR}} + \frac{r - y_{\text{WR}}}{3}$$

$$z_{step1} = 0.25\lambda_g(x_{\text{step1}}, y_{\text{step1}})$$

$$x_{\text{step2}} = x_{\text{WR}} + 2\left(\frac{r - x_{\text{WR}}}{3}\right)$$

$$y_{\text{step2}} = y_{\text{WR}} + 2\left(\frac{r - y_{\text{WR}}}{3}\right)$$

$$z_{\text{step2}} = 0.25\lambda_g(x_{\text{step2}}, y_{\text{step2}})$$

(4.6)

Once these initial values are set an optimization routine was usually implemented, as described next.

CST offers several optimization routines; the one used for this work was Trust Region Framework. This routine requires an initial guess range from the user for all included parameters (in this case all 3 dimensions of step1 and step2), with a target which can also be set by the user. Since the most important quantity of interest here was return loss, the S_{11} parameter was chosen as the figure of merit with a goal of being less than -20 dB, or less than 1% of power being reflected. The Trust Region optimization algorithm relies on a good initial guess within a relatively small range, if the chosen range is not close to the optimum parameter-space there are a couple of options for improving the guess. One option is to reduce the number of parameters being optimized and iteratively change them until a suitable result is found. Another option is perform a parameter sweep on one parameter at a time. This allows the designer to find a relationship (if one exists) between a parameter's value and performance. The final transitions designed by the author are described in detail in section 4.8.

One constraint when designing the two-step transitions made by SWISSto12® was that step2 was required to have greater transverse dimensions than step1 due to SWISSto12's manufacturing methods. Since these designs were completed by the author it has become possible to build transitions without this constraint. This will potentially lead to better designs.

4.2.2 **Tapered transition**

The other method to transition between rectangular and circular waveguides that was considered is more standard among horn antenna designers. It involves placing a piece of waveguide which tapers in cross section from having the rectangular WR waveguide dimensions on one side to a circular cross section of radius r_a on the other. This will produce a smooth change in guide wavelength with axial distance and therefore provide very good impedance matching, depending on the length of the section, which is the only variable in this scenario. This leads to a structure as seen in Figure 4.5.
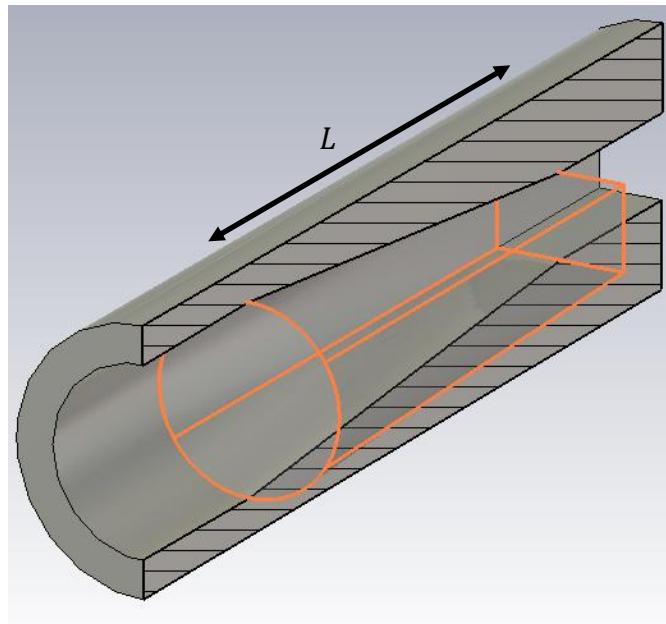

Figure 4.5: Tapered transition between circular and rectangular geometries highlighted in orange.

The only parameter to vary here is the length of the transition, defined by the variable L. The results of a parametric sweep for a tapered transition designed for the WR 10+ band is shown in Figure 4.6.
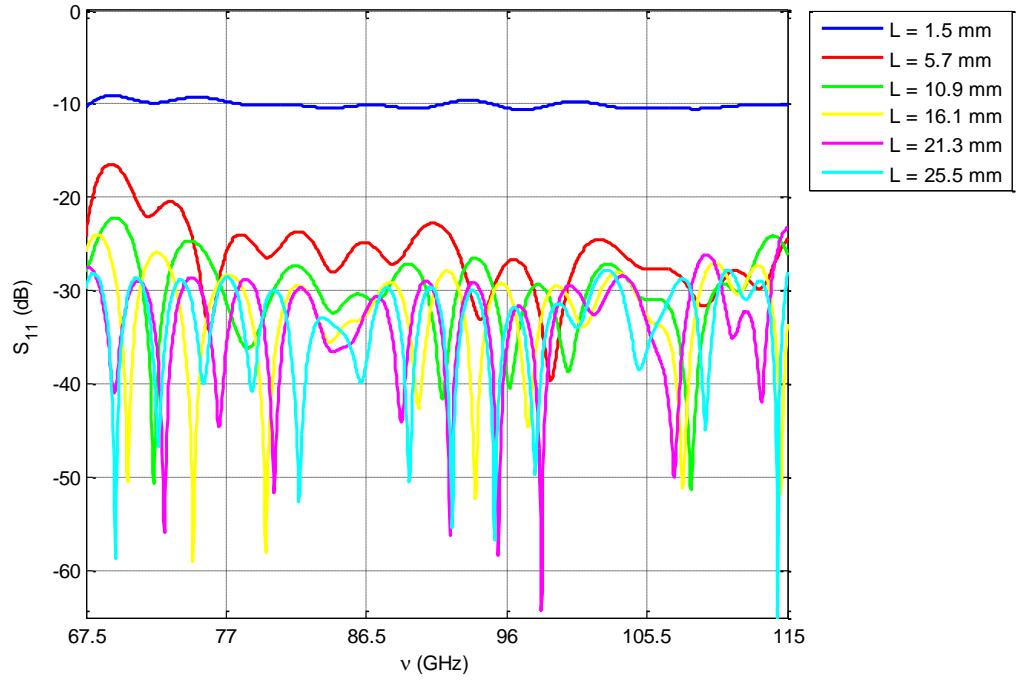
Figure 4.6: Parametric plot of return loss for varying L across the WR 10+ band.

This plot demonstrates how S_{11} is improved with increasing transition length L, although with diminishing return above a length of 20 mm. It is worth noting that the plot in Figure 4.6 is for an extended WR frequency band (WR+), yet it still produces return losses less than around -26 dB across the band, while the average results achieved for the step transition were approximately -20 dB across a standard WR band. Interestingly, when designing a transition for a *square* to circular waveguide transition for the Onsola Space Observatory in Chalmers, Sweden, the author achieved very good results using much shorter transitions (approximately 5 mm). This is suspected to be due to higher order modes propagating in the square waveguide leading to higher power throughput.

One clear advantage of tapered transitions is that they are a lot more straightforward to design than the step transitions. SWISSto12 is planning to 3D print the tapered transitions and machine the step transitions. So far the step transitions have been the favoured method chosen for manufacture, however two designs for the extended WR-10+ and WR-6.5+ bands were investigated using the tapered transition. These will be discussed in section 4.8.

4.3 Circular waveguide to corrugated horn transition

Once a suitable radius (r_a) for the smooth-walled circular waveguide has been found using (4.5) it is possible to begin designing the transition to a corrugated horn throat. The goal here is not only to match the impedance between the smooth walled and corrugated sections but to launch the balanced HE_{11} mode in the horn. For this reason the throat of the horn is sometimes referred to as the mode convertor or mode launching section (34). Again, two design strategies were examined, the first of which was outlined in (22) and will be referred to as the 'Claricoats throat'. The second was described in (27) and will be referred to as the 'Zhang throat'.

The first step in this design, which is the same for both throat types, is to include at least one half of a wavelength of smooth-walled cylindrical waveguide before stepping into the corrugated section. This is to ensure that any evanescent modes which may be propagating are at sufficiently low amplitude at the junction to the corrugated section that they won't couple to higher order modes or contribute detrimental amounts of power to the return loss.

4.3.1 Claricoats throat

The two main issues with this transition are reflections caused by a sudden change in guide wavelength, but also the excitation of undesirable modes in the corrugated section. The HE_{11} and EH_{11} modes have very close cut-on points so it is easy to excite the EH_{11} mode when trying to attain the HE_{11}. The EH_{11} has relatively high cross-polarization and is a "surface-wave" which means most of the power is at the edge of the waveguide walls, the opposite of what is desired for these horns. We can overcome the problem of high levels of reflection by considering the boundary conditions in both types of waveguide, which determine the properties of the waveguide modes. In an ideal smooth walled waveguide the surface reactance $X_z = 0$ and in a corrugated waveguide $X_z = Z_0 \tan(kd)\left(1 - \frac{t}{p}\right)$ as seen in equation

(3.3). Examining the corrugated waveguide surface reactance equation it can be seen that setting the slot depth $d = \frac{\lambda}{2}$ leads to a surface reactance of zero. Now the boundary

conditions and therefore the guide-wavelengths in the smooth-walled and corrugated WGs are matched.

The next thing we want to achieve is a balanced HE_{11} mode propagating in the horn. As outlined in section 3.1 the balanced hybrid condition will be met when the slot depths are equal to $\frac{\lambda}{4}$. The clear answer here is to taper the depth of the slots from $\frac{\lambda}{2}$ to $\frac{\lambda}{4}$ over a number of periods, which will serve the dual purpose of launching a balanced HE_{11} mode without exciting higher order modes and slowly changing the guide-wavelength to achieve good impedance matching and minimize reflections. According to (34) performing this tapering over 5 periods in a linear variation is sufficient for the transition between a smooth-walled and corrugated WG. However, we are trying to transition to a corrugated horn, which has a changing inner radius. A rigorous analysis of this transition and a good method of design has been outlined by (22) and it is this method which was implemented for these designs (Figure 4.10).
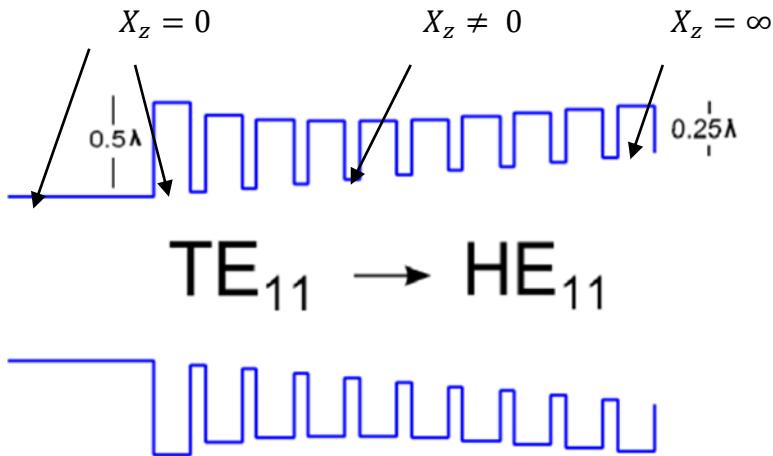

Figure 4.7: Claricoats throat.

The wavelength dependence of the corrugations has negative implications for broadband systems however, as will be discussed, the right choice of horn parameters can reduce the wavelength sensitivity of the horn. By examining the relationship between guide wavelength, inner radius and slot depth as seen in Figure 4.11 (a) it is possible to find a trajectory for the slot depths that will produce a smooth change in guide wavelength, Figure 4.11 (b). These plots are produced by

67

taking account of space harmonic effects of the corrugations and solving for β using equation (3.9) in order to calculate the guide-wavelength for a given value of r_1 and d for a particular mode (22).
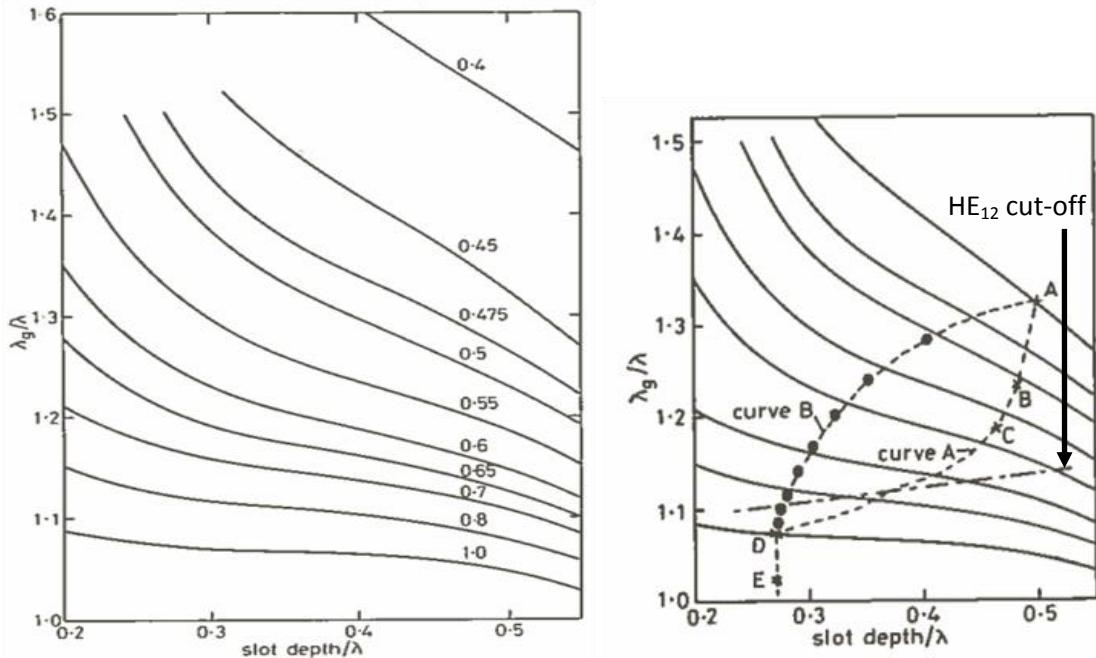

Figure 4.8: (a) Normalized guide wavelength against normalised slot depth for various values of $\frac{r_1}{\lambda}$.

(b) The same as (a), depicting the trajectory of the slot depths. Taken from (21)

In Figure 4.11 (b) two possible trajectories are shown, curve A and curve B, the dashed line represents the HE_{12} cut-off. Curve A represents the trajectory produced by a linear variation in slot depth, Curve B is less conventional and chosen by trial and error to produce a slow variation in guide-wavelength. The idea here is that after the HE_{12} cut-off point the depth of the slots on curve B change very slowly, which prevents this mode from being excited, while they change more rapidly for curve A. Excitation of this mode promotes greater reflections, so curve B is more ideal. Indeed the points on curve B are what were used when producing the throat geometry for the majority of these designs. These points are given in Table 4-3.

Table 4-3: Slots depths for Claricoats throat

Slot number	Slot depth (λ_{design})
1	0.500
2	0.410
3	0.360
4	0.330
5	0.310
6	0.290
7	0.283
8	0.278
9	0.273
10	0.270

It is worth noting that these values are calculated for a slot width of 0.1λ and a ridge width of 0.05λ (w and t respectively in Figure 2.11). It is assumed that these values have little effect on the guide-wavelength, and a choice of ridge-width-to-slot-width ratio of about 0.5 is usually required to produce the desired balanced hybrid condition at the aperture of the horn. Using this design it is typical to achieve return loss of less than -20 dB and HE_{11} modal purity of greater than 92% across a WR band with an optimized horn design, with better results for a narrow band. The return loss for a horn designed using the Claricoats throat for the WR 5.1 band is shown in Figure 4.9.
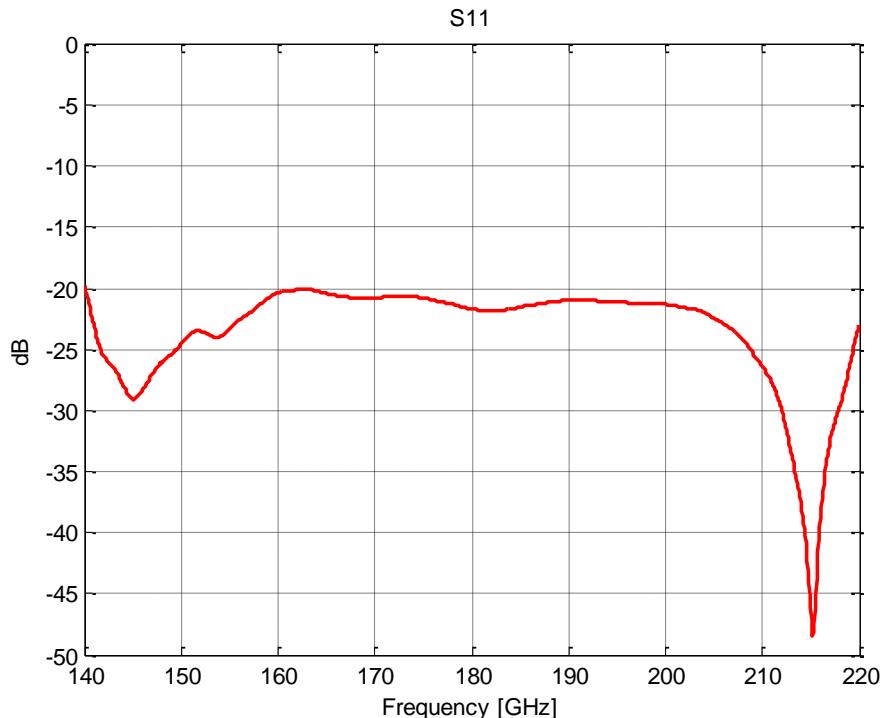

Figure 4.9: Return loss for a horn designed for the WR-5.1 band using the Claricoats throat.

69

The effect of the Claricoats throat on cross-polarization is clearly illustrated in Figure 4.13
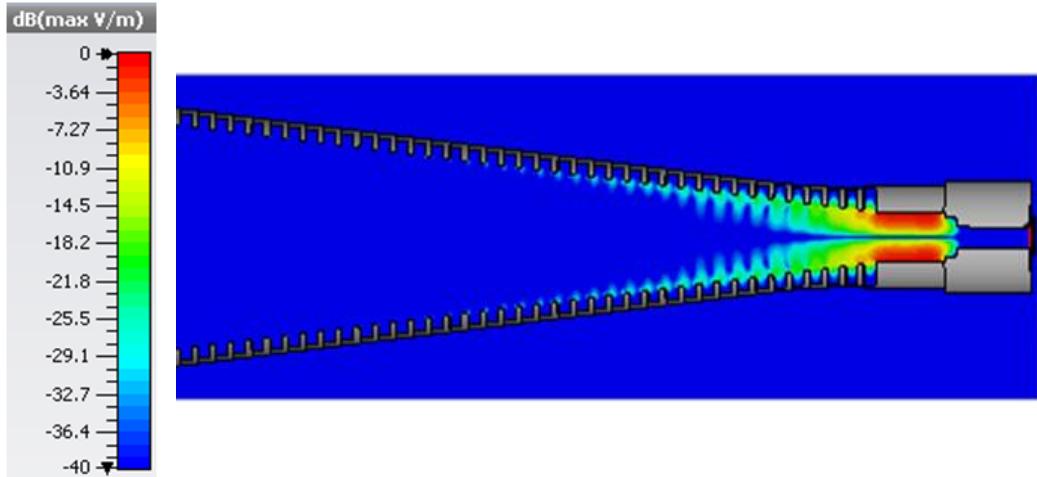

Figure 4.10: Cross-polarisation amplitude at 91.25 GHz in a corrugated horn designed using the Claricoats throat and a two-step transition for the WR-10 band, simulated in CST using the time-domain solver.

Figure 4.13 shows, beginning on the right hand side, that there is no cross-polarization in the rectangular waveguide section, as expected, since only the rectangular TE_{01} mode is supported here and it is linearly polarised (see Figure 2.4). Entering the second transition-step some cross-polar power is present as a higher order mode has cut-on here. Then, in the smooth-walled circular waveguide section, there is a high level of cross-polarization due to the propagation of the circular TE_{11} mode (see Figure 2.2). Stepping into the corrugated section, for the first period the cross-polar power is still relatively high, but quickly diminishes with distance along the axis until reaching a very low value (-40 dB), where it remains to the antenna aperture. It is interesting to note that, once passed the throat, the highest levels of cross-polarization are around the tips of the corrugation ridges. These occur because the open-circuit condition hasn't quite been reached at these radii, and so the radial component of the electric field doesn't terminate completely on the ridges.

4.3.2 Zhang throat

From section 4.3.1 it is clear that the Claricoats design provides very good performance in terms of return loss for the WR-5.1 band, similar performance (less

than -20 dB) was achieved for the rest of the design bands. SWISSto12 was examining the possibility of building a system for two extended WR bands: the WR 6.5+ and the WR 10+ band. This is a change from the standard 110 – 170 GHz to 105 – 180 GHz and 75 - 110 GHz to 67.5 – 115 GHz respectively which represents a significant increase in bandwidth from 40% to 52%. The possibility of achieving return losses of less than -25 dB was also requested for these bands. Figure 4.9 demonstrates that the Claricoats throat is at its limits keeping the return loss less than -20 dB across a standard WR band; this is clearly going to be insufficient for the new design goal across an extended band. For this reason an alternative throat design was considered, this is the Zhang design.

The key difference between the Zhang and Claricoats designs is the attention paid to the ratio of ridge width to slot width. Due to the fact that a low ratio (thinner ridges than slots) is required for the open-circuit condition to occur in the wider part of the horn, it was assumed by Claricoats and Olver that this would be sufficient in the throat of the horn as well. However, close examination of the effect of this value in the narrow part of the horn by Zhang revealed that this was not the case, Figure 4.11 demonstrates this.
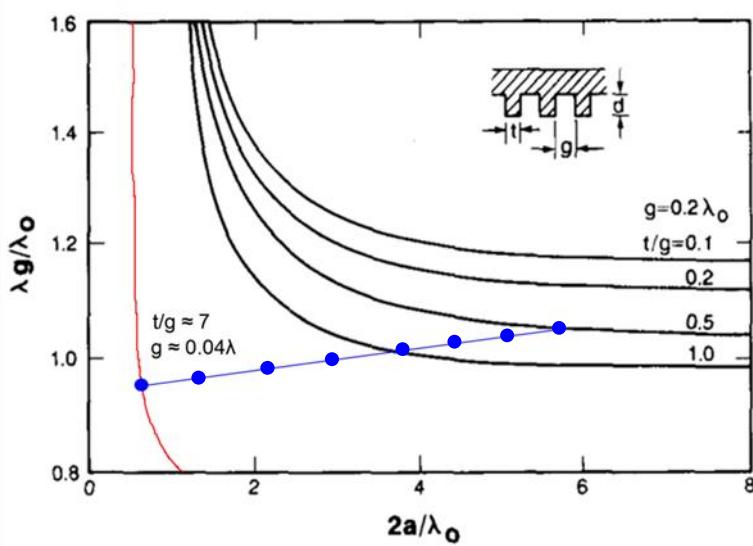

Figure 4.11: Guide-wavelength as a function of inner radius a for various values of $\frac{t}{w}$. (In Zhang's paper w is referred to as g). Taken from (27). (Red and blue lines added by the author)

The graph can be interpreted as the x-axis representing the horn flaring out and the y-axis is simply the guide-wavelength written in terms of the free-space wavelength.

In the narrow part of the horn the guide wavelength is changing very rapidly with inner-radius, this is detrimental to return loss. However, as noticed by Zhang, varying the ratio of ridge with to slot width produces different curves. So, similarly to the way the slot depths were designed in Figure 4.11 by varying $\frac{t}{w}$ it is possible to have a much smoother change in guide wavelength, leading to a much better impedance transformer. An example of this is shown in Figure 4.11, the red and blue lines have been drawn over Zhang's plot to illustrate the idea. The red line represents the curve for a ridge-to-slot-width ratio of approximately 7 with a slot width of approximately 0.04λ. The blue line with dots represents a possible trajectory followed by a linear change in $\frac{t}{w}$. Initial simulations were performed following the design outlined by Zhang, i.e. beginning with a $\frac{t}{w}$ of 7 but tapering this over 11 periods to 0.25 instead of 0.5 following a linear trend, leading to the values show in Table 4-4. The resulting throat geometry is shown in Figure 4.12

Table 4-4: Zhang throat ridge-width-to-slot-width ratios

Corrugation No.	$\dfrac{t}{w}$
1	7
2	6.38
3	5.77
4	5.16
5	4.55
6	3.93
7	3.32
8	2.70
9	2.09
10	1.48
11	0.86
12	0.25

The slots depth were also tapered in a linear fashion here, this had no effect on the HE_{11} modal purity, showing that the effect of changing $\frac{t}{w}$ dominates the performance of the Zhang throat.

$$\frac{t}{w} = 7 \longrightarrow \qquad \longleftarrow \frac{t}{w} = 0.25$$
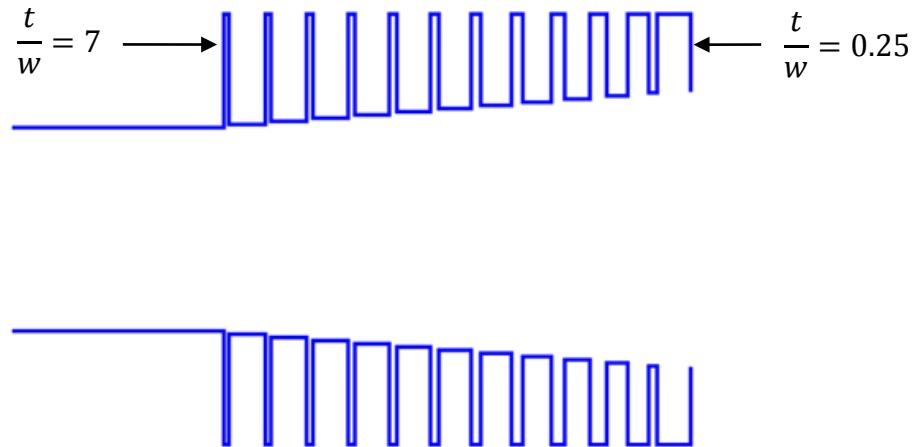
Figure 4.12: Zhang throat geometry

A comparison of the performance, in terms of S_{11} for the WR-6.5+ band is given in Figure 4.13 for two optimized horns, one with a Claricoats and one with a Zhang throat.
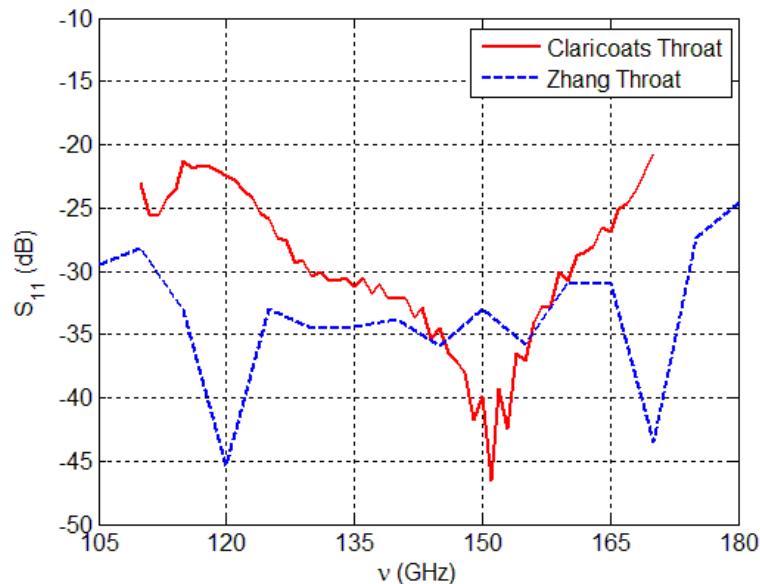

Figure 4.13: Return loss of Zhang and Claricoats throats for WR6.5+/WR6.5 bands.

Although the horn parameters (see Table 4-5 for list) are not exactly the same for these two horns, this graph illustrates the difference between the two throats. Over the full band the performance, in terms of S_{11}, of the Zhang throat is superior. In the end the variable thickness rings needed by SWISSto12 to construct the Zhang throat were deemed too cost ineffective for mass production and the Claricoats throat was used for all final designs.

73

4.4 Throat to aperture transition

This transition can be thought of as including the definition of the final corrugation parameters as well as the geometry of the horn. The important quantities for the horn's geometry include the large aperture radius and the length of the horn. The aperture must be large enough to ensure that the guide wavelength is close to the free-space wavelength at this point (or in the case of the MCK it must match the guide wavelength of a corrugated waveguide of the same diameter). The length of the horn must provide the right taper so that there is a smooth change in guide wavelength along the axis of the horn to provide good impedance matching and prevent power scattering into higher order modes.

For a lot of feedhorn applications (e.g. reflector antennas) the far-field beam pattern is of greater interest than the near-field. The application of these horns as waveguide convertors for the MCKs however meant that the aperture fields were just as important and, as stated in Table 4-2, they should couple strongly to a HE_{11} mode, as this is the desired mode of propagation in the MCK's corrugated waveguide.

The standard linearly tapered corrugated horn should provide the required performance in terms of HE_{11} coupling, however there are other profiles worth considering. These non-linear profiled horns are often referred to simply as "profile horns" (30) and are defined as such when the radius of the horn as a function of the horn's length is a non-linear function, Figure 4.15.
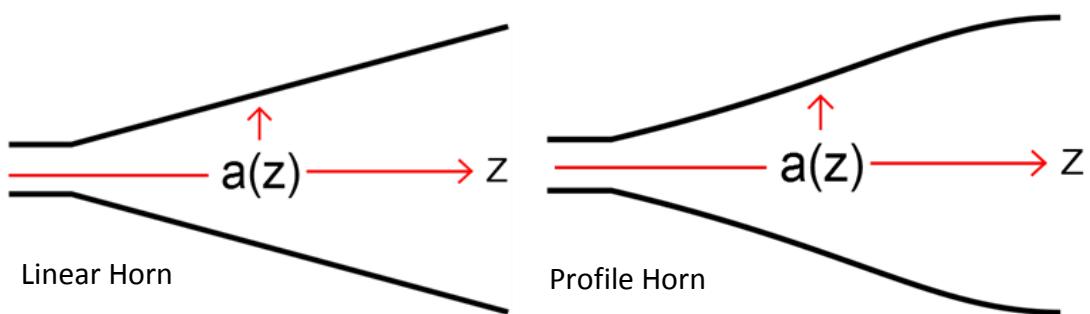

Figure 4.17: Linear and Profile horns

There have been many profiles considered by horn designers, each with their own advantages and disadvantages, the main positive aspects of profile horns are (30):

1. The horn can be shorter while still having the same ratio of throat radius to aperture radius.

2. The flare-angle at the aperture of the horn can be close to zero, this reduces the spherical phase error.

3. The phase centre of the horn can be close to the aperture and is therefore relatively frequency-independent.

4. The small flare angle at the throat is ideal for achieving impedance matching.

Of particular interest is point 2, the spherical phase error refers to the flatness of the phase front at the aperture. For linear horns the phase-front is that of a locally-spherical wave with a phase-radius given by the slant-length of the horn. The phase error is the maximum phase difference across the aperture of the horn, it is usually taken as the difference between the phase at the centre and edge of the aperture and is given by (4.7), (25). Figure 4.17 shows this effect.
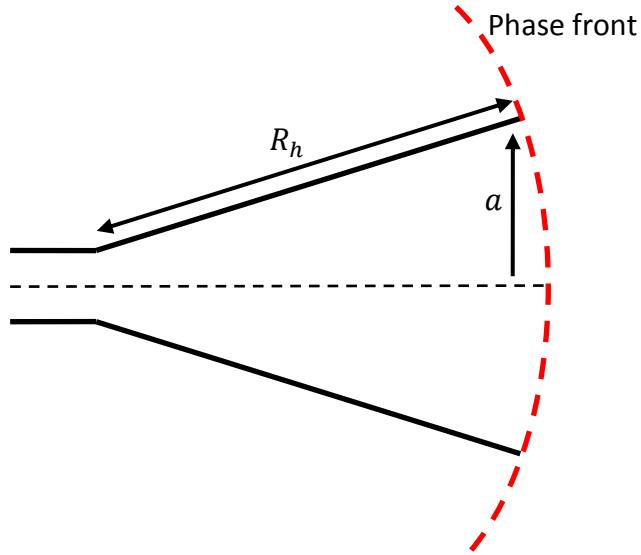

Figure 4.14: Illustration of the spherical phase front at the aperture of a horn.

$$\beta = \frac{\pi a^2}{\lambda R_h} \tag{4.7}$$

where a is the radius of the horn and R_h is the horn slant length. Reducing this quantity improves the gain and efficiency of an antenna. Related to this is the phase centre of the horn, mentioned in point 3 above. The phase centre is the position in the horn where the beam waist is located. The beam waist is the narrowest part of a beam, where the phase is flat, clearly is it advantageous if this is located close to the aperture of the horn as this leads to a reduction in β. Frequency independence

of the phase centre position is useful for broadband designs. Some examples of profile horn variations for corrugated horns are: Gaussian (35), Hyperbolic, Tangential, Exponential and more (36) which can be used depending on what the designer wants to achieve.

Not only will minimization of β improve the radiation properties of the horn, but it should also improve the coupling to a straight corrugated waveguide for the MCK applications. A straight corrugated waveguide can be thought of as being a horn with infinite slant length: $R_h \to \infty$, this leads to $\beta = 0$ or a perfectly flat phase front. For this reason a Sine-Squared profile (22) horn was examined as a candidate for this work. The Sine-Squared profile function is described in equation (4.8) and shown in Figure 4.15.

$$a(z) = a_1 + (a_2 - a_1)\left[\frac{z}{L}(1-A) + A\sin^2\left(\frac{z\pi}{2L}\right)\right] \tag{4.8}$$

where a_1 is the throat radius, a_2 is the aperture radius, L is the total axial length of the horn, z is the distance along the axis, $a(z)$ is the radius at z and A is the degree of the Sine-Squared profile. $A = 0$ is a linear taper and $A = 1$ is an extreme Sine-Squared profile.
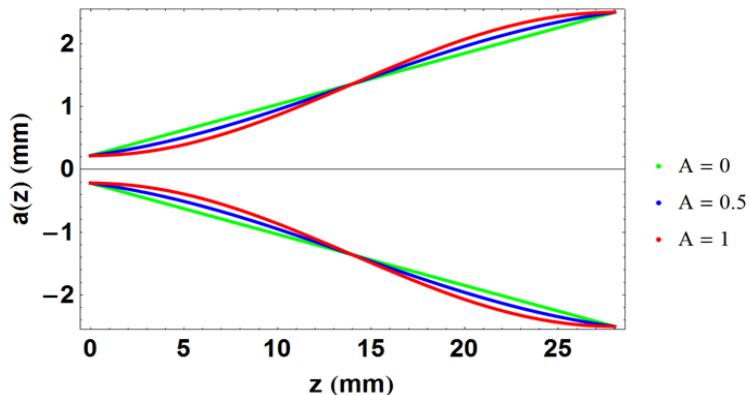

Figure 4.15: Sine-squared profile for various values of A.

The effect of using a sine-squared profile can be seen in Figure 4.16.
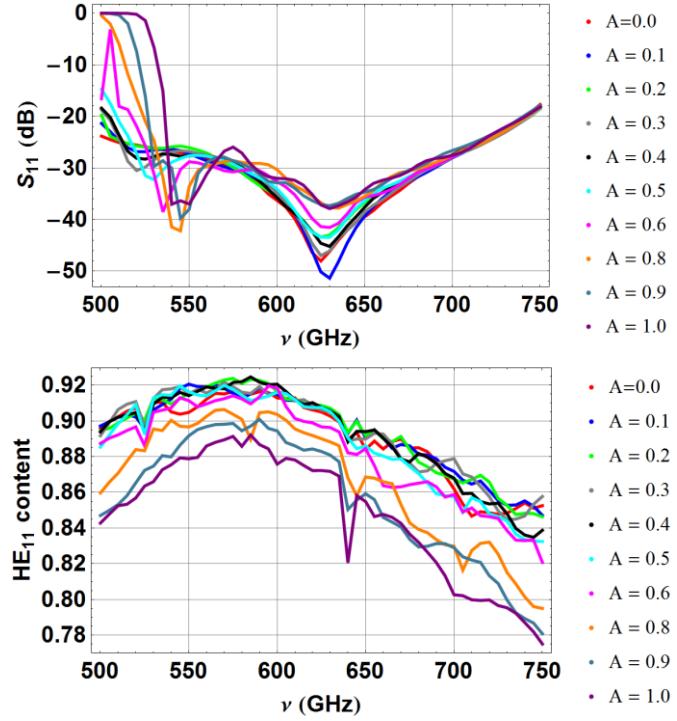
Figure 4.16: Return loss and HE11 content as functions of frequency for a WR=1.5 band horn, for various degrees of Sine-squared profile.

From Figure 4.16, both return loss and HE_{11} content are degraded for high values of A ($\geq$ 0.5). The return loss is especially bad at low frequencies for values of $A \geq 0.5$ and after around 700 GHz there is only a slight difference between the different profiles. There is a slight improvement in HE_{11} content for low, non-zero values of A ($A \leq 0.5$) at several points across the band, but on average there is no advantage to using a sine-squared profile. Values of A bigger than 0.5 produce a clear degradation in HE_{11} content. This degradation is due to excitation of higher order modes as the profile becomes more complex. In general a linear profile was seen to be just as good, or better than any sine-squared profiles, and so it was decided that, for this work, all horns would have a linear profile.

The other aspect of the horn is of course the corrugations. Their design, along with the general geometry of the horn and the throat region was done in a heavily customised version of SCATTER which allowed the user to generate a geometry file, or rather, define variables representing the information contained in a geometry file. Before beginning the discussion on the design procedure for this stage, it is important to describe the design parameters that must be considered.

4.5 Use of SCATTER in design process

The parameters controlling the geometry of the horn are listed in Table 4-5.

Table 4-5: Corrugated horn critical parameters

Parameter	Description
v_{design}	This is the design frequency of the horn. It is useful to define the depth of the slots in terms of this.
p	This is the period of the corrugations. Chosen to be at least 3 per λ. $p = w + t$.
w	The width of a slot.
t	The width of a ridge.
$\dfrac{t}{w}$	The ratio of ridge width to slot width is arguably more important that the values of w and t themselves.
L	The length of the horn.
R_{guide}	This is the radius of the large aperture of the horn. Together with L this defines the flare angle of the horn.
R_{in}	The small aperture radius.
L_{in}	The length of the initial section of smooth-walled waveguide.
A	The degree of the Sine-squared profile.

The choice of these parameters will determine the performance the horn. Once these parameters have been defined a geometry file is then created following the flow-chart in Figure 4.20. Is it now of interest to examine the effect of these parameters on the performance of the horn. This is done by creating another loop outside of the geometry file creation, which loops over a variable, termed $'ps'$. This variable can be used to represent one or more of the horn geometry parameters. The range and increment size of ps must be chosen appropriately for the parameter being examined. Finally, as these horns must operate over a broad bandwidth it is useful to perform a frequency sweep analysis. As SCATTER is a frequency domain simulator only one frequency can be examined at a time. Usually the parametric sweep analysis was done at three frequencies across a band: the lowest, centre and highest frequencies. Once a design was found to be acceptable at these three frequencies a full frequency sweep of the entire band was performed using this design. The results of this design work are documented in section 4.8.

Define horn parameters

Calculate the number of sections:
$$N = Floor\left[2\frac{L}{p}\right]$$

Create array defining the n throat slot depths and values of $\frac{w}{t}$.

Zhang

Claricoats or Zhang?

Claricoats

Create array defining the n throat slot depths.

Create two $1 \times N$ arrays for Radii and Lengths, set first elements as defined (R_{in}, L_{in}). Set $i = 1, j = 1, Z = 0$.

Is $i < n$?

Yes

Set the ith R(Z) using (4.8), set $Z = Z + t$. Set the $(i + 1)^{th}$ R(Z) using (4.8)+the jth slot depth, set $Z = Z + w$. Set the ith length to w and the $(i + 1)^{th}$ to t*. Set $i = i + 2, j = j + 1$.

No

Set the ith R(Z) using (4.8), set $Z = Z + t$. Set the $(i + 1)^{th}$ R(Z) using (4.8)+the nth slot depth, set $Z = Z + w$. Set the ith length to w and the $(i + 1)^{th}$ to t^*. Set $i = i + 2$.

Yes

Is i < N?

No

Finish

Figure 4.17: Flowchart describing how a corrugated horn geometry file was created

* For the Zhang design the first n values of w and t are changing, after the nth they remain constant.

4.6 Full design procedure

This section will describe the full design procedure considering a two-step transition with the Claricoats throat, as these were the chosen design concepts for all final designs.

4.6.1 Design parameters

The three sections just described (rectangular to circular transition, circular smooth to corrugated transition and the horn itself) are co-dependent and so cannot be designed in complete isolation. For example it was often necessary to include the throat of the horn in the CST simulation when designing the rectangular to circular two-step transition. The first stage of the design, which was usually the most time consuming, was designing the horn antenna itself (including the throat). The time-consuming nature of this is due to the fact that there are a large number of parameters which are all inter-related. Once a horn was finalised the transition section was designed. There were also some restrictions provided by SWISSto12 on which parameters could be varied and to what precision they could be produced, due to manufacturing limits. It was also more cost-effective to produce components with the least strict tolerance requirements. These limitations are shown in Table 4-6 and a diagram illustrating the components they refer to is shown in Figure 4.21.

Table 4-6: Limitations on the design parameters.

| Parameter	Free/Fixed	Tolerance
Corrugation depth d	Free	Max: $\pm 2\ \mu$m, Ideal: $\pm 10\ \mu$m
p	Free	$10 \pm 1\ \mu$m
w	Free	$10 \pm 1\ \mu$m
t	Free	$10 \pm 1\ \mu$m
$\dfrac{t}{w}$	Free	N/A
L	Fixed (Upper-limit)	$10N \pm \sqrt{N(1\mu m)^2}, N\ is\ number\ of\ sections$
$Rguide$	Fixed	Max: $\pm 2\ \mu$m, Ideal: $\pm 10\ \mu$m
Rin	Free	Max: $\pm 2\mu$m, Ideal: $\pm 10\ \mu$m
Lin	Free	$10 \pm 1\ \mu$m
A	Free	N/A
$WRx/y, box1x$ $/y, box2x/y$	Free	$\pm 3.5\ \mu$m
$WRz, box1z, box2z$	Free	$\pm 6\ \mu$m
Transition alignment	N/A	$\pm 2\ \mu$m
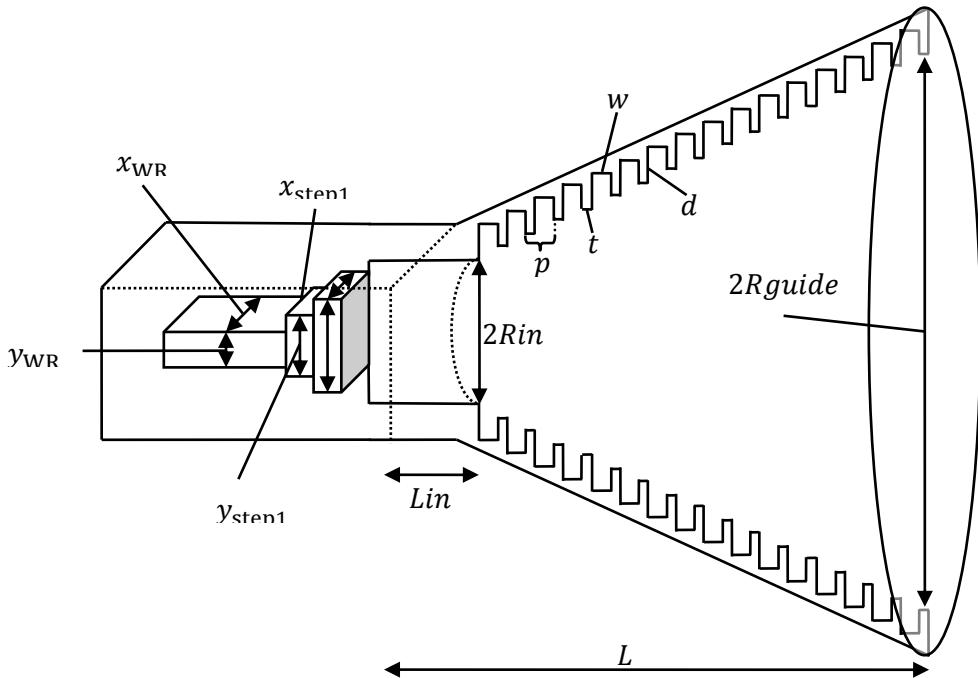
Figure 4.18: Schematic diagram showing the various design parameters (except for WRz, $box1z$ and $box2z$ which are shown in Figure 4.3).

The first step in the design was to calculate R_{in} using (4.5), generally the value found in this way is the optimum value for the band in question but occasionally it may be varied slightly. The values of R_{guide} were also defined by SWISSto12 before the design began, however for some designs it was necessary to alter this. To reduce the manufacturing costs it was beneficial to keep the length L as short as possible, however the large difference between R_{in} and R_{guide} meant L was generally over 50 periods. The period p of the corrugations was chosen so that there were at least 3 periods per wavelength. The slot width w and ridge thickness t are usually chosen so that $t < w$ (except of course in the case of the Zhang throat) with the exact ratio depending somewhat on R_{guide}. If p is predefined w can be calculated using $p = w + aw$, where $a = \frac{t}{w}$. As mentioned in Table 4-5 the corrugation slot depth d is defined in terms of the design frequency (converted to wavelength using $c = f\lambda$ with a value of $c = 299792458\ \text{ms}^{-1}$). Since the WR bands are characterized in terms of frequency it is convenient to design a horn with respect to the frequencies in the band. As the designs progressed the design procedure evolved. It was sometimes useful to define parameters other than the slot depth as a function of frequency in order to better understand how their

81

dimensions related to the frequency band. For example w was sometimes considered as a function of v_{design}. Another important change came upon the realisation that the ratio of t to w was a critical parameter.

There are no exact rules or even empirical equations for choosing the values of the parameters of a corrugated horn. Some guidelines do exist (see e.g. (22)) and make for good starting points. However, since every horn will have a somewhat unique application and performance criteria the method for design will be quite variable and generally will work by trial and error (this is why simulations are of extreme importance in this area, and fast simulations highly desirable). The key to creating a good design in a reasonable amount of time is to choose sensible ranges when performing parametric sweep analyses. At the beginning of this project it was quite difficult to decide on what these ranges should be. There are some hints given in chapter five of (22), mostly concerning cross-polarization and beam divergence angle characteristics. There will now be a review of the performance metrics before the specific design work is discussed in detail.

4.6.2 Performance metrics

The three main performance metrics were the peak far-field cross-polarization levels, the return loss and the aperture-field coupling to a HE_{11} mode. The cross-polarization levels are found by calculating the maximum value of the field component perpendicular to the excitation field. The circular symmetry of the horn makes this an arbitrary choice. The inherited SCATTER code set the x-component the co-polar direction and the y-component the cross-polar direction. Cross-polarization was the least troublesome performance metric. The return loss is given by the S_{11} matrix of the horn. The HE_{11} coupling is calculated by performing a numerical overlap integral between the horn's aperture field and an ideal HE_{11} mode (25). The expression for an ideal HE_{11} mode at the aperture of a horn is given in (2.63), however in this case the field being coupled to is inside a straight corrugated waveguide. A corrugated waveguide can be thought of as a horn with infinite slant length; $R_H = \infty$. This leads to (4.9):

$$\vec{E}_{HE_{11}} = J_0\left(\frac{2.405r}{R_{guide}}\right)\exp\left(\frac{-j\pi r^2}{\lambda\infty}\right)\hat{x} = J_0\left(\frac{2.405r}{R_{guide}}\right)\hat{x} \qquad (4.9)$$

The overlap integral for two functions:

$$\int_x \int_y \Psi_1(x,y)\Psi_2^*(x,y)\,dxdy \tag{4.10}$$

where * indicates the complex conjugate, can be evaluated numerically using a finite summation

$$\sum_{x=x_1}^{x_N} \sum_{y=y_1}^{y_N} \Psi_1(x,y)\Psi_2^*(x,y)\,\Delta x \Delta y \tag{4.11}$$

where the functions are evaluated at a grid of points (with step sizes Δx, Δy) over the area of interest. Decreasing the value of the step size will better approximate the real fields, hence increasing the accuracy of the results. A grid can be generated using either Cartesian (as in (4.11)) or circular-polar coordinates. It is also important to properly normalise the fields so that power is conserved and coupling is correctly calculated. In this case it was decided to make the grid using a Cartesian coordinate system, an example of this is shown in Figure 4.19.
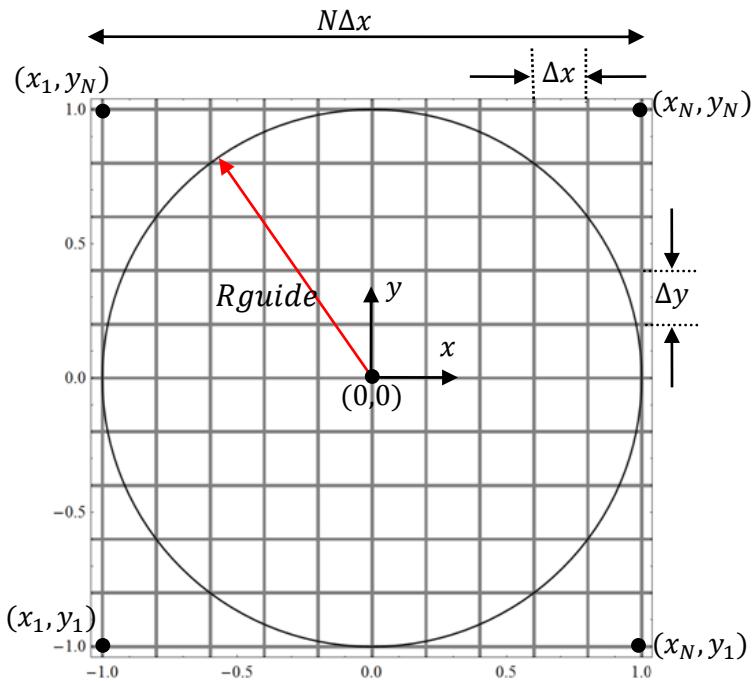
Figure 4.19: Gridding system used for plotting fields/calculating coupling.

The circle in Figure 4.19 represents the aperture of the horn and along this line the electric field must be zero. Just outside of it, in real systems there is a small electric

83

field, however for the purposes of calculating the aperture field coupling the electric field outside the circle is set to zero, as seen in (4.12):

$$\vec{E}(x,y) = \begin{cases} \vec{E}(x,y) \ \ if \ \sqrt{x^2 + y^2} \le R_{guide} \\ \ \ 0 \ \ if \ \sqrt{x^2 + y^2} > R_{guide} \end{cases} \tag{4.12}$$

Since the electric fields change with transverse position in the plane, each position in the grid is calculated independently and stored in a $N \times N$ square array, where the position in the array is mapped to the position in the plane of the electric field. In (3.11) to (3.18) the x and y components of the electric field are written as functions of r and ϕ, so in order to grid the field using Cartesian coordinates it was necessary to write r and ϕ in terms of x and y, this is done using (4.13):

$$r = \sqrt{x^2 + y^2},$$
$$\phi = \tan^{-1}\left(\frac{y}{x}\right) \tag{4.13}$$

so that $\vec{E}_x(r,\phi)$ and $\vec{E}_y(r,\phi)$ become $\vec{E}_x(\sqrt{x^2 + y^2}, \tan^{-1}\left(\frac{y}{x}\right))$ and $\vec{E}_y\left(\sqrt{x^2 + y^2}, \tan^{-1}\left(\frac{y}{x}\right)\right)$ respectively. Finally, the coupling coefficient is then calculated as shown (4.14):

$$\tag{4.14}$$

$$\eta_c = \frac{\sum_{i=1}^{N}\sum_{j=1}^{N} E_{co}(x_i,y_i)E_{HE_{11}}^*(x_i,y_i)}{\sqrt{\left(\sum_{i=1}^{N}\sum_{j=1}^{N}(E_{co}(x_i,y_i)E_{co}^*(x_i,y_i) + E_X(x_i,y_i)E_X^*(x_i,y_i))\right)} \ \sum_{i=1}^{N}\sum_{j=1}^{N} E_{HE_{11}}(x_i,y_i)E_{HE_{11}}^*(x_i,y_i)}$$

where E_{co} is the co-polar field, E_X is the cross-polar field and $E_{HE_{11}}$ is the HE_{11} field. The denominator is a normalisation factor and $N = \frac{2 \times R_{guide}}{\Delta x}$. If the normalisation is done correctly the coupling will always be between 0 and 1. It is worth noting that only the co-polar coupling is of interest here, as the balanced HE_{11} mode is purely linearly polarized, however the cross-polar antenna field must be included in the normalisation factor to account for the total power in the aperture beam.

4.7 Example of a design (WR-1.0)

To illustrate the design process I will describe the progress of the WR-1.0 band ($750 - 1100$ GHz) design. The initial parameters provided by SWISSto12 set

$R_{guide} = 2.5$ mm and $L \leq 35$ mm. R_{in} was calculated using (4.5) to be 0.15 mm. Beginning with nominal values of $w = 0.2\lambda_c$, $\frac{t}{w} = 0.45$, $L = 30$ mm the design wavelength was varied between $0.85\lambda_c - 1.05\lambda_c$ (λ_c is the central wavelength) resulting in the plots shown in Figure 4.21 and Figure 4.25. Examining these plots it is clear that a design with acceptable levels of peak cross-polar power (< -20 dB) and return loss (< -20 dB) has been found (by choosing $\nu_{design} = 1.05\nu_c$ for example), however the HE_{11} content at the central and upper frequency is below the required 92 % and is almost constant with ν_{design}. This is most likely due to the fact that the value of R_{guide} is equal to between 6 and 9 wavelengths, whereas all previous designs had been between ~ 2 and 6 wavelengths. This was a cause for concern as a horn with such a large aperture would be hard to keep single-moded without being very long.
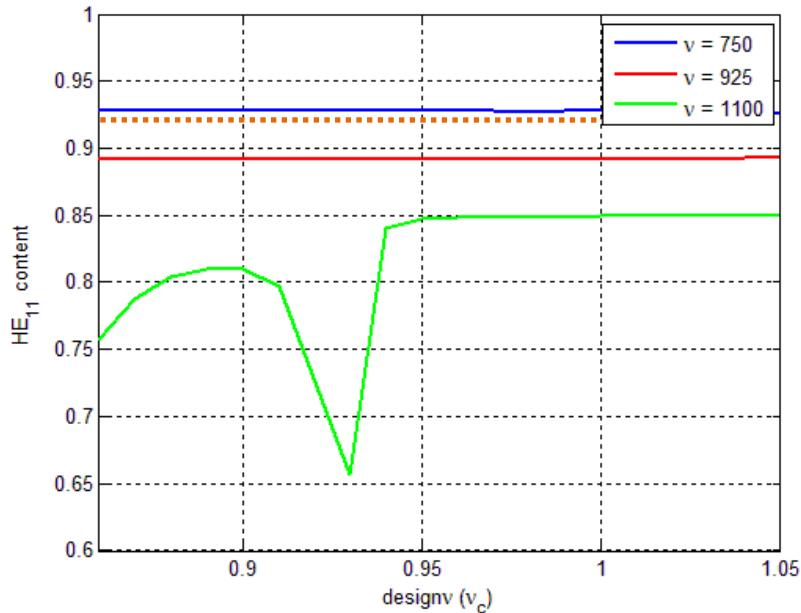
Figure 4.21: Parameter sweep of ν_{design} (here named $designv$)[1] as a function of central frequency for the WR-1.0 band. HE_{11} coupling was calculated at the centre and edges of the band. Dashed orange line shows the desired level of 92% HE_{11} coupling.

---

[1] Please note the use of "$designv$" in place of (ν_{design}) in many of the upcoming plots.
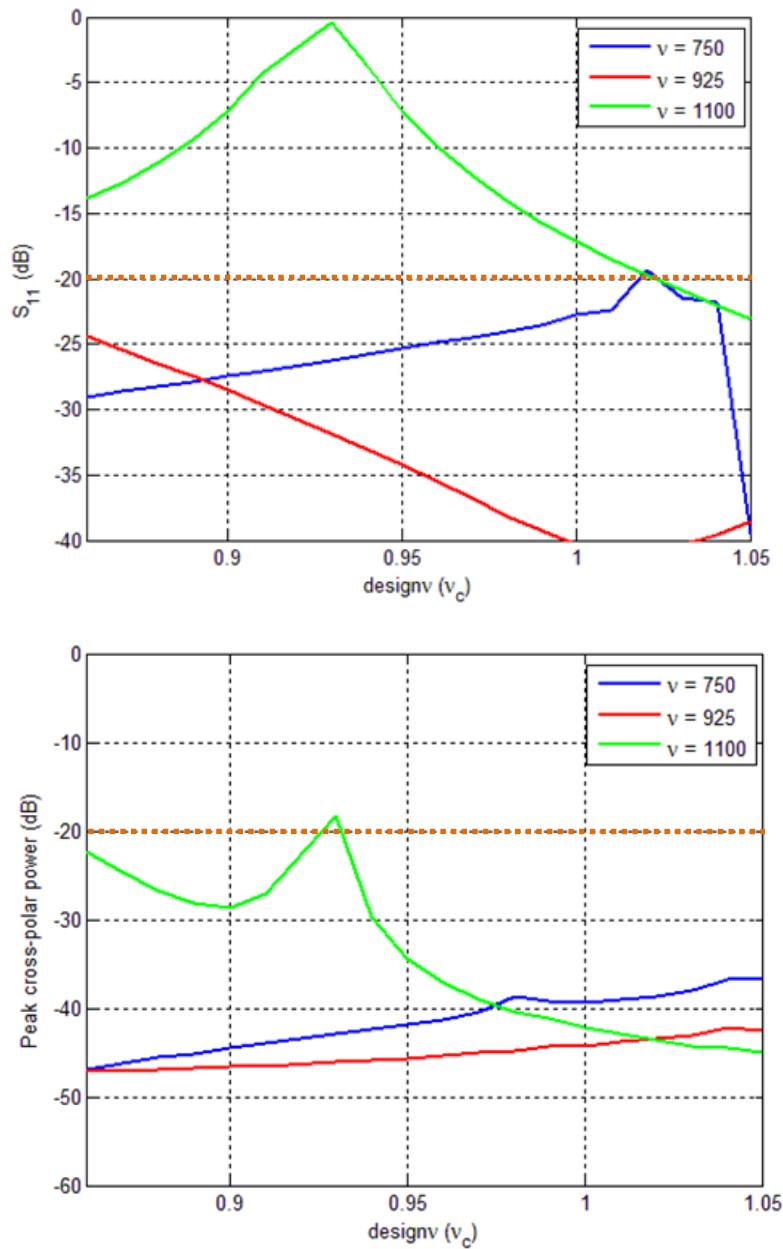
Figure 4.22: Parameter sweep of $designv(v_c)$ for the WR-1.0 band. Return loss (top) and peak cross-polar power (bottom) were calculated at the centre and edges of the band. Dashed orange lines show desired levels of -20 dB.

This is seen in the results of Figure 4.25 as at higher frequencies more higher-order modes have been excited than at the low frequencies. Two possible solutions were examined: increase the length of the horn or decrease the size of the aperture, the results of this are shown in Figure 4.26.
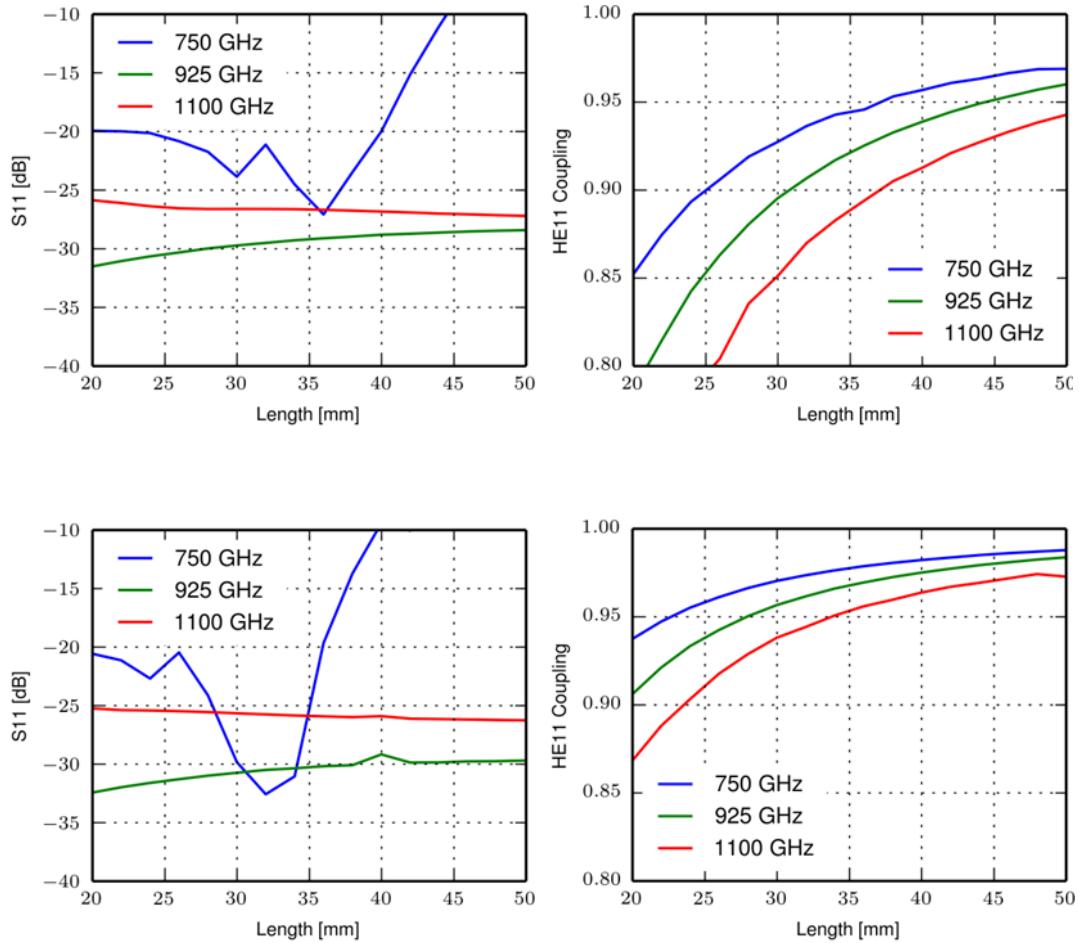
Figure 4.23: Return loss (S$_{11}$) and HE$_{11}$ content as a function of length for a WR-1.0 band horn with $Rguide = $ 2.5 mm (top) and 2 mm (bottom).

Considering Figure 4.26, when the aperture radius is 2.5 mm, acceptable HE$_{11}$ content is only achieved at lengths of over 40 mm; however at these lengths the return loss is at -20 dB and above for 750 GHz. When the aperture radius is 2 mm acceptable HE$_{11}$ content is achieved at lengths of 30 mm and the return loss is below -20 dB for all frequencies. Clearly the best choice is to reduce the aperture radius to 2 mm, which was done after consulting with SWISSto12.

At this point SWISSto12 also requested that the value of $\frac{t}{w}$ be set to unity, as the more rings there are of the same thickness, the cheaper the horn is to manufacture (the high frequencies in this band require very small period corrugations meaning that many rings will be needed (hundreds) for a horn of ~30 mm). Once the parameters had been found to work at 750, 915 and 1110 GHz, a full frequency

sweep was performed and the geometry was imported into CST in order to simulate the horn together with the rectangular to circular transition.

The results were found to vary rapidly with frequency, which lead the author to investigate the effect of the rounding of ring radii values on the horn performance. Up until now the values of the individual radii had been rounded to the nearest 10 μm for the purposes of reducing manufacturing costs. However this was being done *after* the SCATTER simulation when generating a geometry file for import to CST. The CST simulation was then producing results that were inconsistent with SCATTER. Quite an alarming consequence of this rounding can be seen in Figure 4.27, where 10 μm precision on the radii produces a jagged geometry profile.
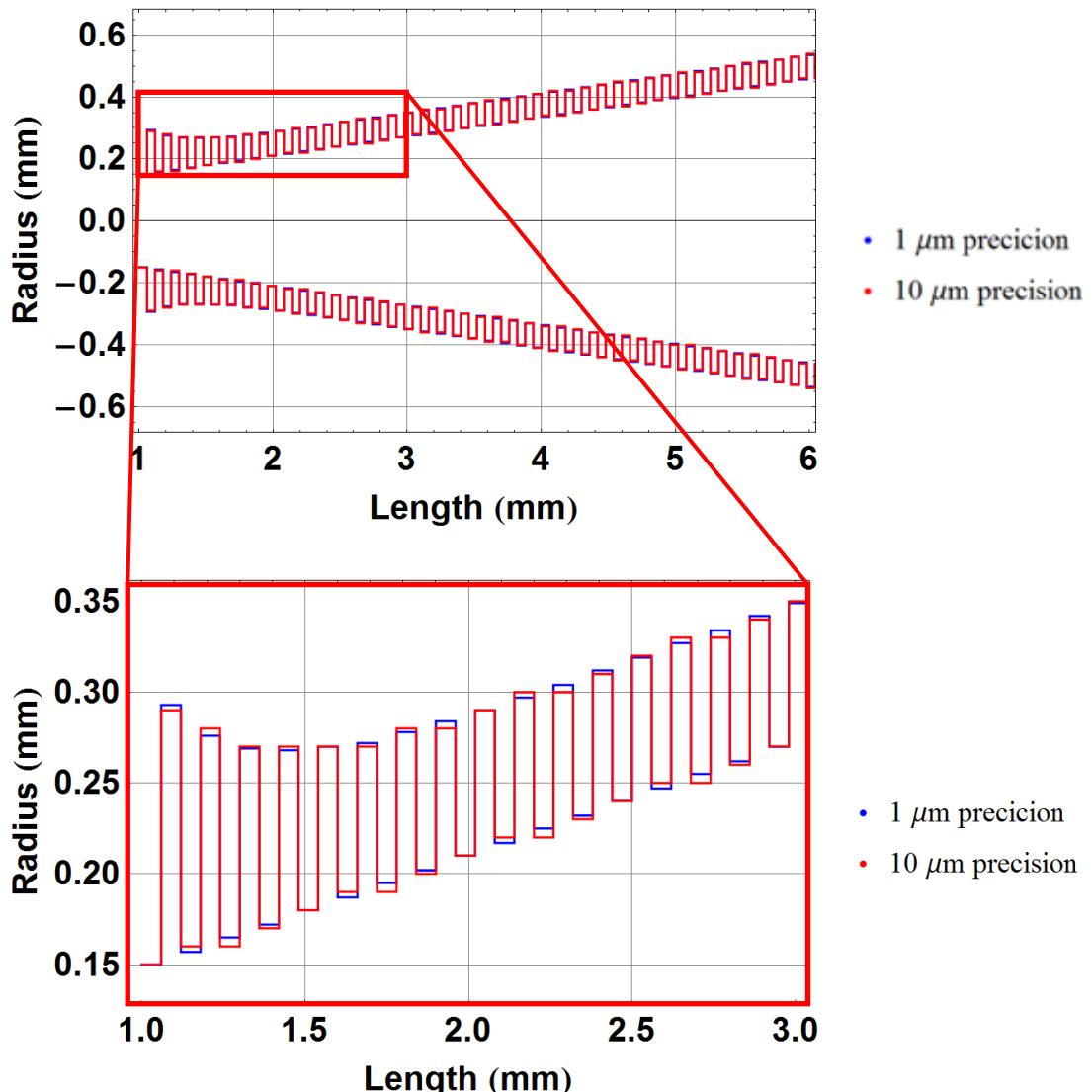
Figure 4.24: Comparison of 1 μm and 10 μm precision in radii values for the WR-1.0 horn. (Note only the first 6 mm of the total horn are shown here).

This clearly visible jaggedness must have a detrimental outcome on the horn's performance; it was decided to test this by comparing the performance with the same horn simulated to have a realistic precision of 1 μm (see Figure 4.27 for the profile). A performance comparison for each of these rounding values is shown in Figure 4.28 and Figure 4.29. (Note: these results were produced using SCATTER). A more general conclusion on the effect of manufacturing tolerance as a function of frequency is given in section 4.9.
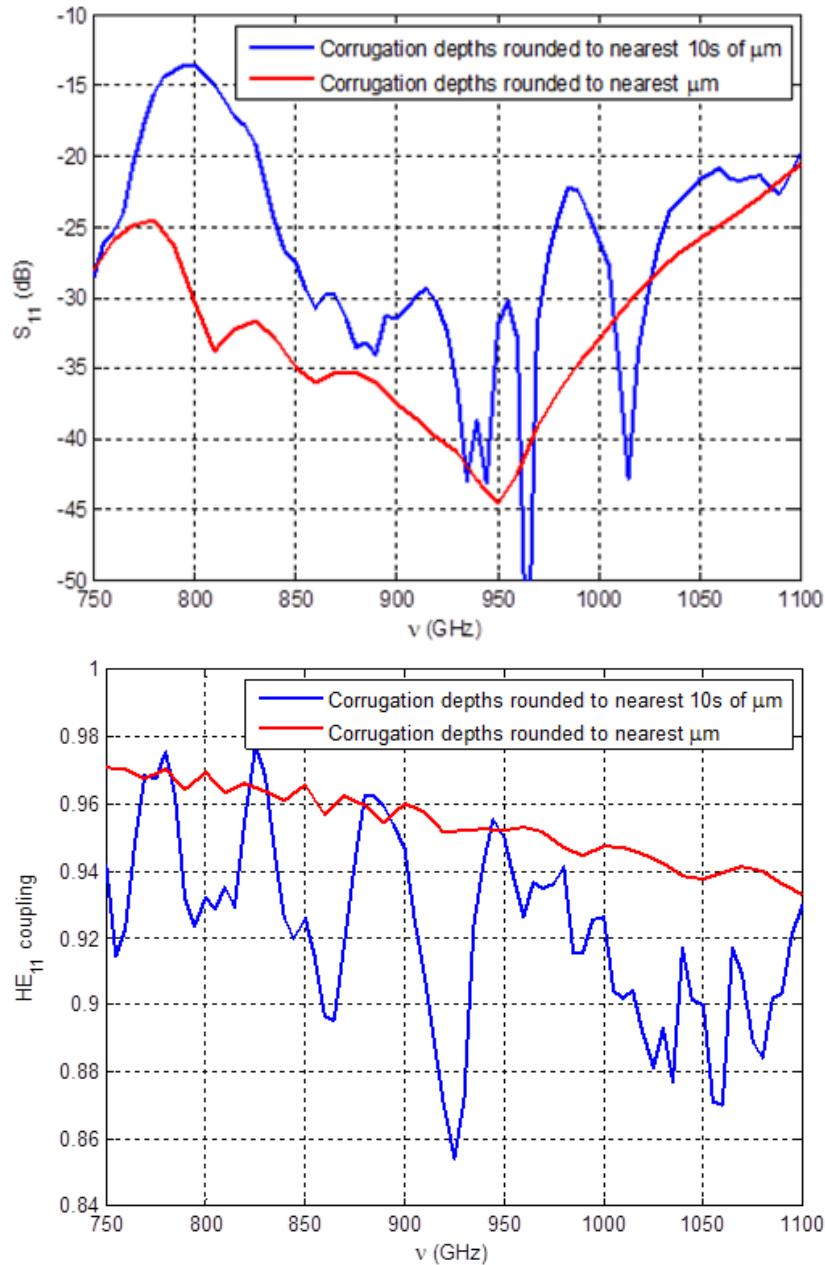
Figure 4.25: Effects of 10 μm and 1 μm precision radii values on return loss (top) and HE$_{11}$ coupling (bottom) as functions of frequency for a WR-1.0 band horn. (The cross-polar content was acceptable for both sets of corrugations)
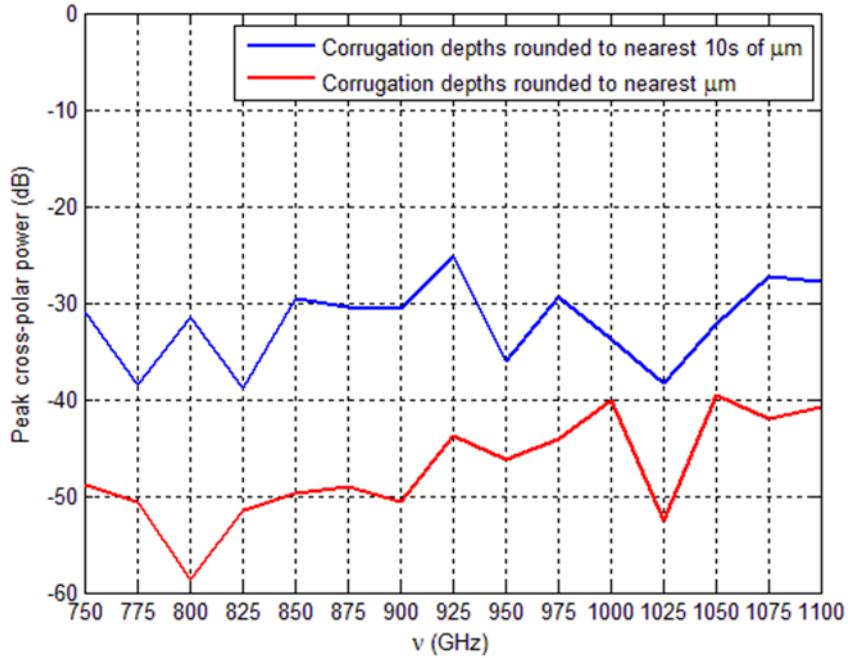
Figure 4.26: Effects of 10 μm and 1 μm precision radii values on peak cross-polar power. The highest value is less than the required -25 dB for both sets of corrugations.

Figure 4.29 shows that with ring radii values rounded to the nearest 1 μm, the designed horn meets the performance criteria (HE$_{11}$, return loss and cross-polar content) across the full WR-1.0 band (see Table 4-7 for parameters).

The values of w and t also have a precision of 10 μm, however the performance of the horn is not as frequency sensitive for these parameters. In this case 10 μm is equal to approximately 10 % of the slot depth and is equal to between 9 % and 10 % of a wavelength.

Table 4-7: Final horn parameters for WR-1.0 horn. (Tolerance of 1 μm required for ring radii).

Parameter	Value	Value (λ_c)
ν_{design}	971.25 GHz	$1.05\nu_c$
w	0.065 mm	$0.2\lambda_c$
$\dfrac{t}{w}$	1	1
L	32 mm	98.74
R_{guide}	2 mm	6.17
R_{in}	0.15 mm	0.46
L_{in}	1 mm	3.09
A	0	0

The only aspect left to be designed is the rectangular to circular transition; a two-step transition was requested by SWISSto12. The method for designing this transition was outlined in section 4.2.1, with the parameters being initially defined

using (4.6). A parametric sweep analysis was then used to improve these values and finally the Trust Region Framework optimization routine was used to optimize the return loss. In this case the optimized parameters that were found are shown in Table 4-8. This transition produced the return loss shown in Figure 4.29.

Table 4-8: WR-1.0 two-step transition, initial and final parameters.

Parameter	Initial Value (mm)	Final Value (mm)
x_{step1}	0.268	0.255
y_{step1}	0.183	0.163
z_{step1}	0.105	0.098
x_{step2}	0.283	0.324
y_{step2}	0.241	0.242
z_{step2}	0.105	0.098
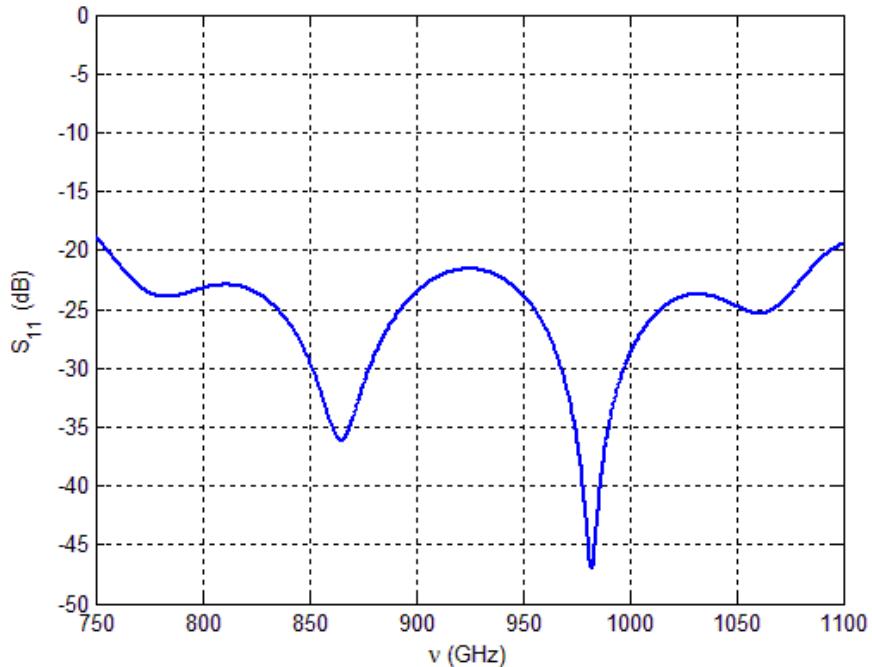
Figure 4.27: Return loss for the WR-1.0 step transition.

The horn antenna was then added to the structure using a CST Visual Basic macro file written by Stephen Doherty of Maynooth University, which reads in two text files, one with the radii and one with the lengths and creates a series of cascaded hollow cylinders making up the horn. This lead to the final return loss and HE_{11} content across the band, shown in Figure 4.29.
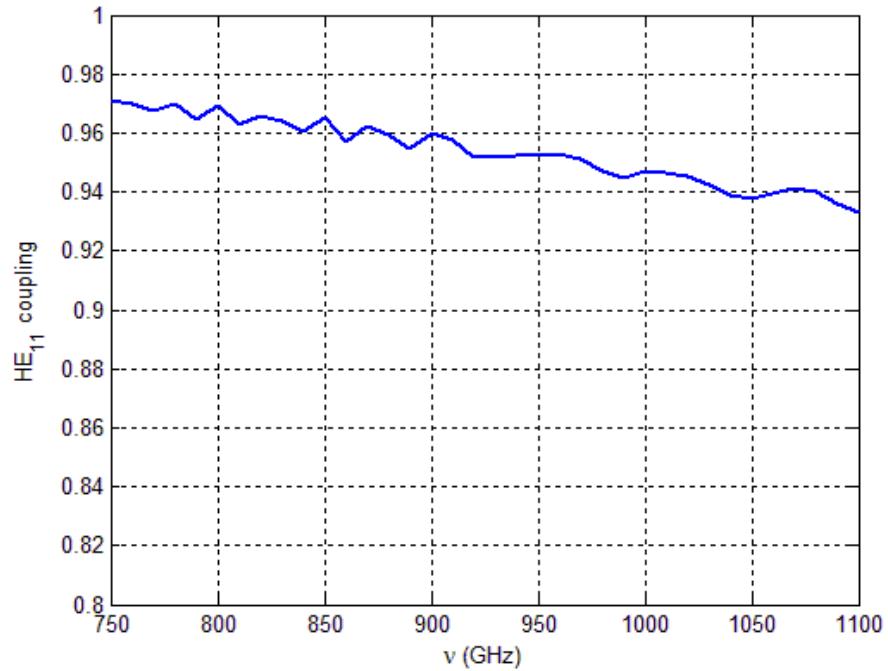
**Figure 4.28: HE11 content as a function of frequency for the final WR-1.0 module**
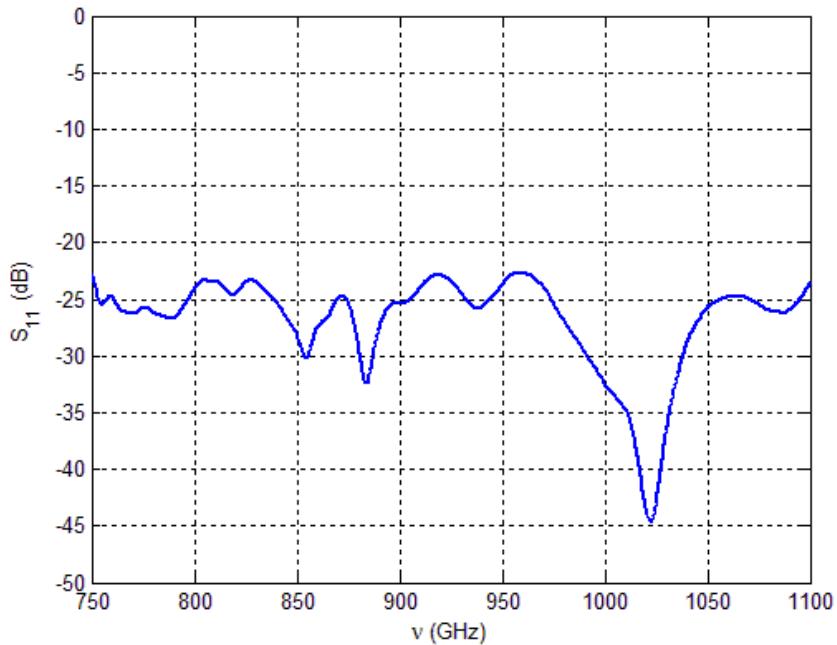
Figure 4.29: Return loss as a function of frequency for the final WR-1.0 module.

The full design met the criteria of less than -20 dB S_{11} and HE_{11} coupling greater than 92% across the full WR-1.0 band.

4.8 Results

The preceding methods were used to design horns for 6 individual bands, including two separate designs for the WR-3.4 band (one for the SWISSto12 module and one

for a plasma physics experiment at the Ecole Polytechnique Federale de Laussane (EPFL), Switzerland, (37)). The final dimensions of the various parameters for both the corrugated horn and step transitions are included in the following tables.

4.8.1 **WR-1.0**

The parameters of the horn and step-transition for the WR-1.0 band (750-1100 GHz) are shown in Table 4-9 and Table 4-10.

Table 4-9: Two-step transition parameters for the WR-1.0 design.

Parameter	Value (mm)	Value (λ_{mid})
x_{step1}	0.255	0.787
y_{step1}	0.163	0.502
z_{step1}	0.098	0.302
x_{step2}	0.324	1.0
y_{step2}	0.242	0.747
z_{step2}	0.098	0.302

Table 4-10: Corrugated horn parameters for the WR-1.0 design.

Parameter	Value	Value (λ_{mid})
v_{design}	971.25 GHz	0.952
w	0.065 mm	0.2
$\dfrac{t}{w}$	1	1
L	30 mm	92.564
R_{guide}	2 mm	6.17
R_{in}	0.15 mm	0.46
L_{in}	1 mm	3.09
A	0	0

4.8.2 **WR-1.5**

The parameters of the horn and step-transition for the WR-1.5 band (500-750 GHz) are shown in Table 4-11 and Table 4-12

Table 4-11:Two-step transition parameters for the WR-1.5 design.

Parameter	Value (mm)	Value (λ_{mid})
x_{step1}	0.382	0.796
y_{step1}	0.254	0.529
z_{step1}	0.138	0.287
x_{step2}	0.423	0.882
y_{step2}	0.333	0.694
z_{step2}	0.137	0.286

Table 4-12:Corrugated horn parameters for the WR-1.5 design.

Parameter	Value	Value (λ_{mid})
ν_{design}	640 GHz	0.977
w	0.1 mm	0.340
$\dfrac{t}{w}$	0.5	0.5
L	26 mm	58.37
R_{guide}	2.5 mm	5.212
R_{in}	0.219 mm	0.457
L_{in}	1 mm	2.085
A	0	0

4.8.3 WR-3.4

The parameters of the horn and step-transition for the WR-3.4 band (220-330 GHz) are shown in Table 4-13 and Table 4-14

Table 4-13:Two-step transition parameters for the WR-3.4 design.

Parameter	Value (mm)	Value (λ_{mid})
x_{step1}	0.87	0.798
y_{step1}	0.516	0.473
z_{step1}	0.325	0.298
x_{step2}	0.935	0.858
y_{step2}	0.746	0.684
z_{step2}	0.347	0.318

Table 4-14: Corrugated horn parameters for the WR-3.4 design.

Parameter	Value	Value (λ_{mid})
ν_{design}	300 GHz	0.917
w	0.25 mm	0.229
$\dfrac{t}{w}$	0.4 mm	0.4
L	30 mm	27.519
R_{guide}	4 mm	3.669
R_{in}	0.5 mm	0.459
L_{in}	1 mm	0.917
A	0	0

4.8.4 WR-3.4 EPFL

This horn was unusual as it was for use over a reduced bandwidth of 243 – 283 GHz, and also the corrugated waveguide it was coupling to had already been built, meaning the corrugation depths were pre-defined. However, these corrugations were found to be non-ideal when designing the horn. The solution to this problem was to taper the slot depths at the horn aperture to those in the waveguide over ten periods, as shown in Figure 4.30. The parameters of the horn and step-

transition for the WR-3.4 band design for EPFL (243-283 GHz) are shown in Table 4-15 and Table 4-16.
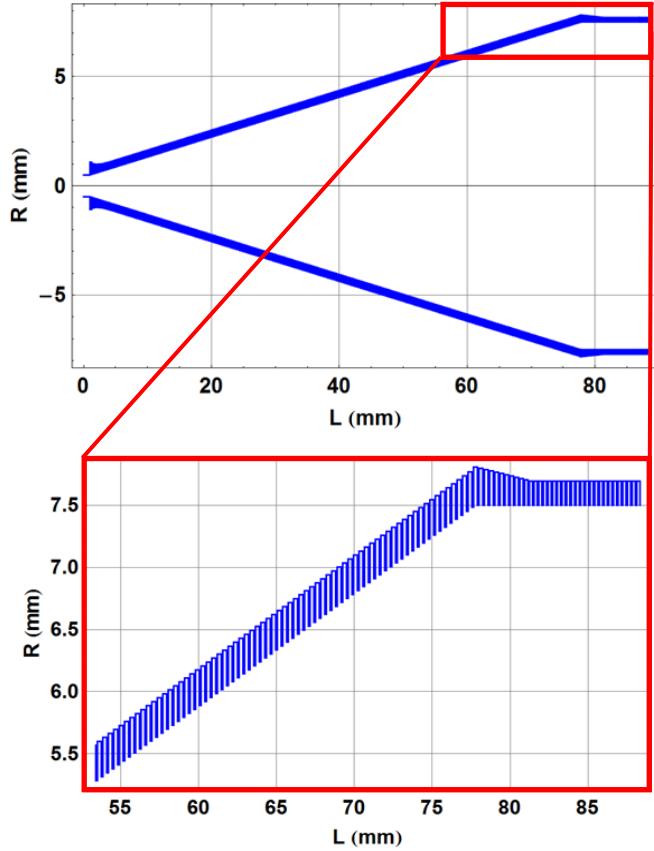

Figure 4.30: WR-3.4 horn for EPFL.

Table 4-15: Two-step transition parameters for the WR-3.4 design for EPFL.

Parameter	Value (mm)	Value (λ_{mid})
x_{step1}	0.87	0.763
y_{step1}	0.516	0.453
z_{step1}	0.325	0.285
x_{step2}	0.935	0.820
y_{step2}	0.746	0.654
z_{step2}	0.35	0.307

Table 4-16: Corrugated horn parameters for the WR-3.4 design for EPFL.

Parameter	Value	Value (λ_{mid})
v_{design}	263 GHz	1.046
w	0.25 mm	0.229
$\dfrac{t}{w}$	0.4	0.4
L	81 (horn), 88 (horn+trans)	74.301
R_{guide}	7.5	6.88
R_{in}	0.5	0.459
L_{in}	1	0.917
A	0	0

4.8.5 **WR-5.1**

The parameters of the step-transition and horn for the WR-5.1 band (140-220 GHz) are shown in Table 4-17 and Table 4-18

Table 4-17: Two-step transition parameters for the WR-5.1 design.

Parameter	Value (mm)	Value (λ_{mid})
x_{step1}	1.304	0.783
y_{step1}	0.89	0.534
z_{step1}	0.437	0.262
x_{step2}	1.48	0.889
y_{step2}	1.246	0.748
z_{step2}	0.499	0.3

Table 4-18: Corrugated horn parameters for the WR-5.1 design.

Parameter	Value	Value (λ_{mid})
ν_{design}	194 GHz	0.928
w	0.373 mm	0.224
$\dfrac{t}{w}$	0.6	0.6
L	48 mm	28.82
R_{guide}	4 mm	2.402
R_{in}	0.75 mm	0.45
L_{in}	1 mm	0.6
A	0	0

4.8.6 **WR-6.5**

An interesting example of the power of a parametric sweep analysis occurred during the design of this module. Initially a design was found to work at the lower, centre and upper ends of the band (110, 140 and 170 GHz), (following the procedure outlined in 4.7). However, a full frequency sweep revealed a spike in return loss at a previously unexamined frequency (165 GHz). By reducing the frequency range in the simulation to vary around this point (150 – 170 GHz) and performing a parameter sweep over many frequencies (steps of 1 GHz in this case) it is possible to find an empirical relationship between a parameter's value and the frequency at which the peak in return loss occurs, see Figure 4.31.
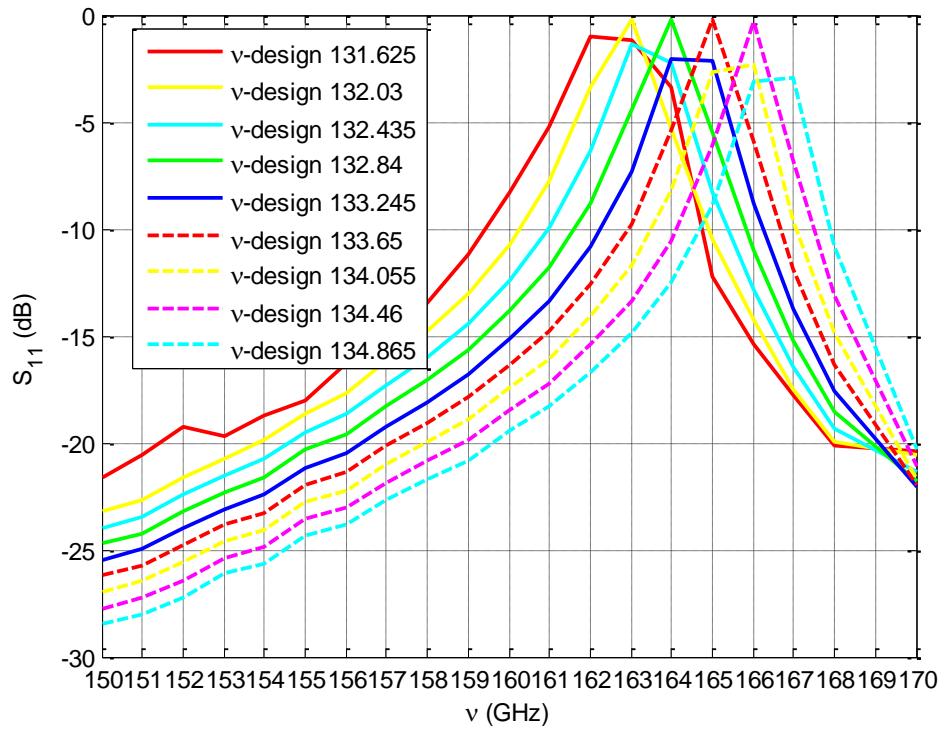
Figure 4.31: Return loss vs. frequency for several values of design frequency, in the WR-6.5 band.

From this information it was found that when the design frequency was equal to approximately 0.81 times the test frequency there was a spike in the return loss at this test frequency. So by choosing a value for design frequency which resulted in a return loss spike outside of the WR-6.5 band's range it is possible to remove this spike from the band of interest. In this case the design frequency must be set to a value greater than 145 GHz. The parameters of the step-transition and horn for the WR-6.5 band (110-170 GHz) are shown in Table 4-19 and Table 4-20.

Table 4-19: Two-step transition parameters for the WR-6.5 design.

Parameter	Value (mm)	Value (λ_{mid})
x_{step1}	1.651	0.771
y_{step1}	0.980	0.458
z_{step1}	0.550	0.257
x_{step2}	2.847	1.330
y_{step2}	1.574	0.735
z_{step2}	0.544	0.254

Table 4-20: Corrugated horn parameters for the WR-6.5 design.

Parameter	Value	Value (λ_{mid})
v_{design}	156 GHz	0.897
w	0.56 mm	0.26
$\dfrac{t}{w}$	0.4	0.4
L	62 mm	28.95
R_{guide}	4 mm	1.868
R_{in}	1.06 mm	0.495
L_{in}	4 mm	1.868
A	0	0

4.8.7 WR-10

The parameters of the step-transition and horn for the WR-10 band (75-110 GHz) are shown in Table 4-21 and Table 4-22.

Table 4-21: Two-step transition parameters for the WR-10 design.

Parameter	Value (mm)	Value (λ_{mid})
x_{step1}	2.396	0.739
y_{step1}	1.535	0.474
z_{step1}	0.879	0.271
x_{step2}	3.092	0.954
y_{step2}	2.422	0.747
z_{step2}	0.846	0.261

Table 4-22: Corrugated horn parameters for the WR-10 design.

Parameter	Value	Value (λ_{mid})
v_{design}	104.7 GHz	0.883
w	0.83	0.256
$\dfrac{t}{w}$	0.56 mm	0.56
L	70 mm	21.6
R_{guide}	9 mm	2.777
R_{in}	1.60 mm	0.494
L_{in}	5 mm	1.543
A	0	0

4.8.8 Final performance curves

Finally, the performance curves are presented in Figure 4.32 and Figure 4.33. Only the HE_{11} and S_{11} are shown because, as mentioned in section 4.1.1 the cross-polar power is taken into account in the HE_{11} coupling as this is a linearly polarized field, so strong coupling to this implies low cross-polarization. In general cross-polarization was never an issue when designing these horns, less than -20 dB of

cross-polar power came naturally with the high HE$_{11}$ content. The far-field beam patterns are shown in Appendix A, these include the cross-polar fields.
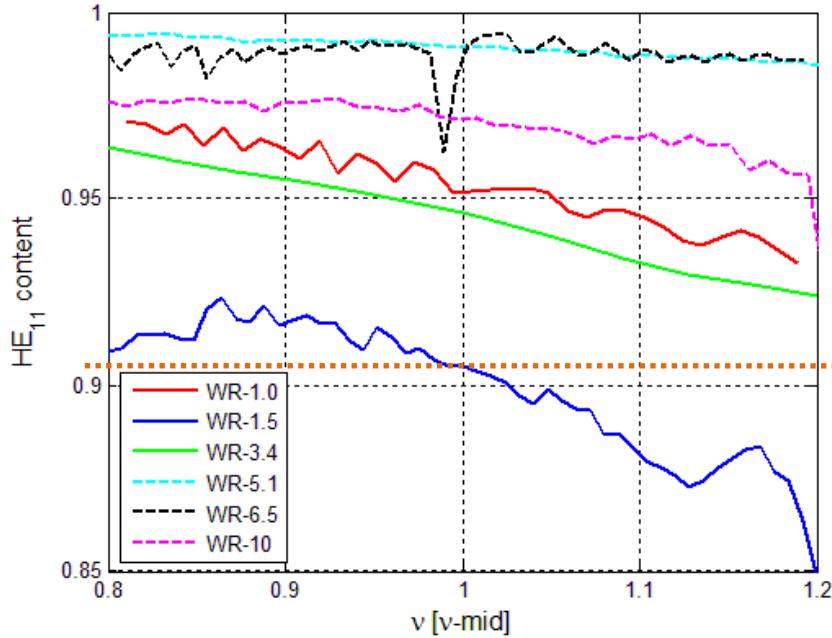
Figure 4.32: Final HE$_{11}$ content as a function of frequency (normalized to the central frequency) for each of the standard WR designs.
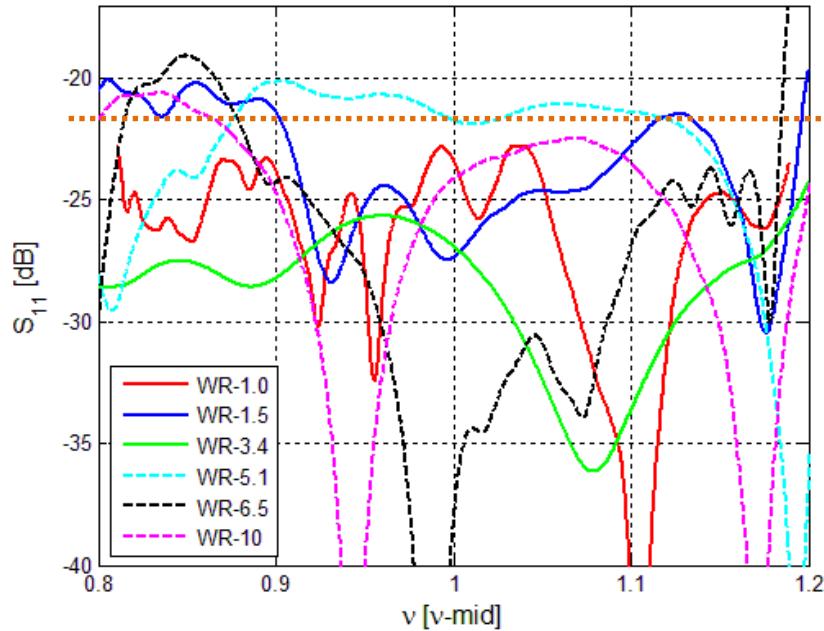
Figure 4.33: Final S$_{11}$ content as a function of frequency (normalized to the central frequency) for each of the standard WR designs.

Clearly the WR-1.5 band horn is does not meet the required level of 92 % HE$_{11}$ coupling, this is due to the particular design being the first one done in Maynooth and HE$_{11}$ content was not a metric being considered at the time.

4.8.9 WR+ bands (WR-6.5+, WR-10+)

The possibility of producing ultra-low return loss horns (less than -25dB) across two extended bands for WR-6.5 and WR-10 plus, as mentioned in 4.3.2, was examined. These designs made use of the tapered transition (see 4.2.2) and the Zhang throat (see section 4.3.2). Ultimately they were deemed too expensive for mass production by SWISSto12. They are worth presenting as, in theory, they worked very well. The return loss results from CST simulations are shown in Figure 4.34. The S_{11} is well below -20 dB across the entire band for both designs and well below - 25 dB for most of the bands, with a large portion of both bands being below or at -30 dB, which is equivalent to 0.1% of the power being reflected.
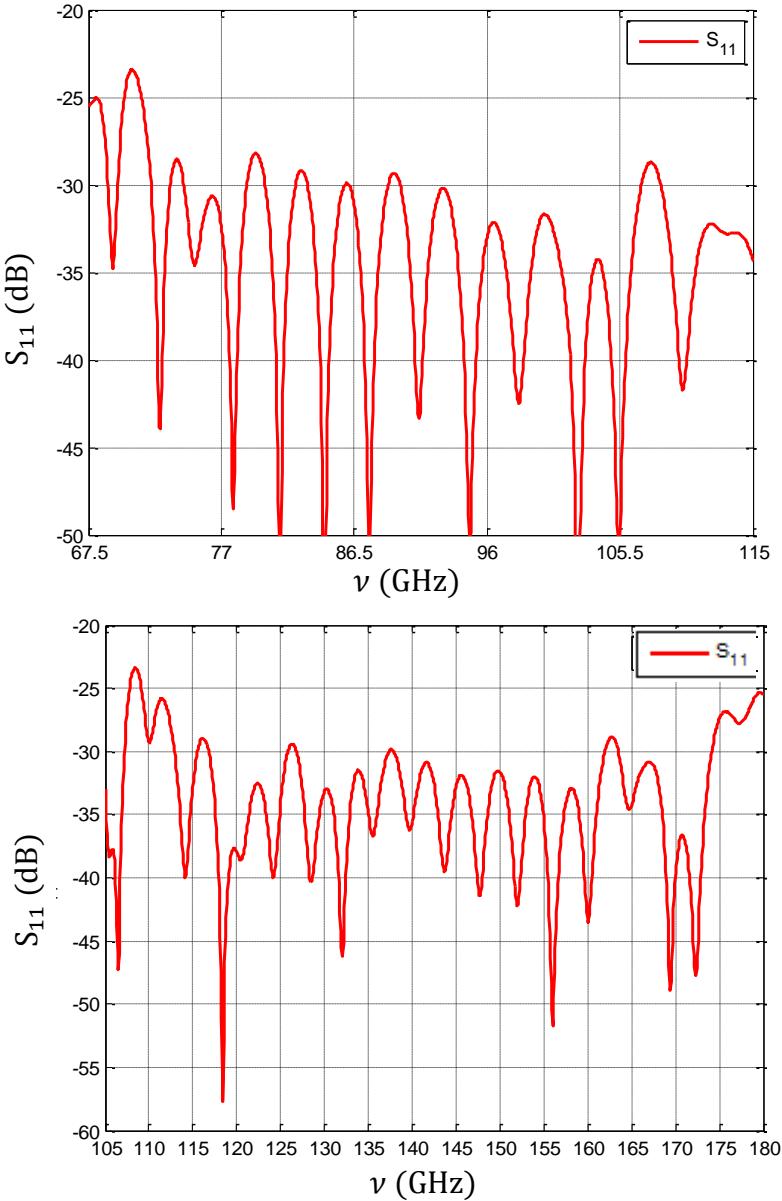
Figure 4.34: Return loss as a function of frequency for the WR-10+ (top) and WR-6.5+ (bottom) bands using the tapered rectangular to circular transition and Zhang throat designs.

4.8.10 **Analysis of optimised geometries**

An analysis of the geometries of the final designs has been done in order to try and gain some insight to the relationships between the optimised parameters found and the frequency band. These results may be useful for providing starting points when designing a corrugated horn antenna using a parametric sweep analysis in the future.

In Figure 4.35 the length of the designed horns as a function of the central wavelength of a band is shown. From this plot it can be seen that, although the horn length in mm generally increases with increasing wavelength, the horn length as a function of central wavelength actually decreases.
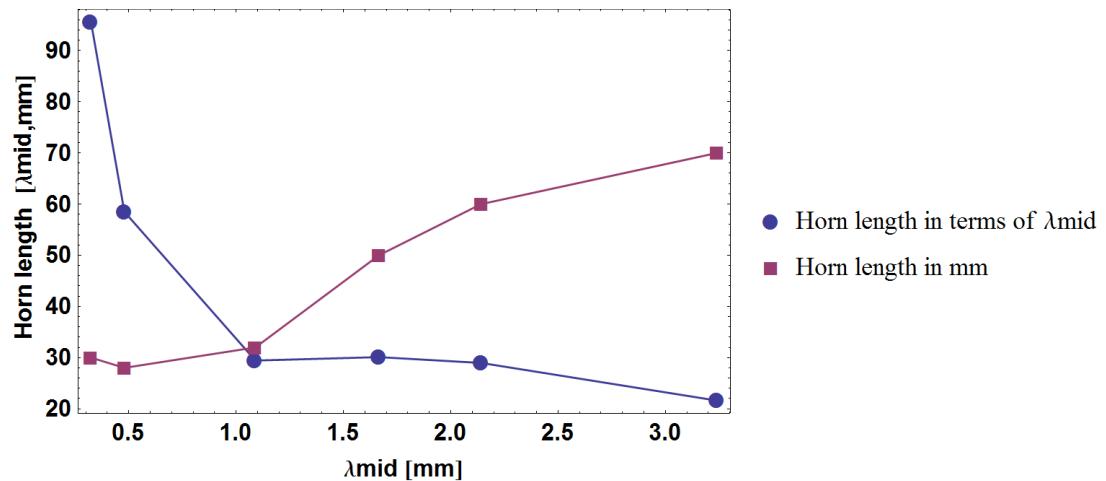
Figure 4.35: Horn length in as a function of the central wavelength of a band.

Figure 4.36 shows the variation in $\frac{w}{t}$ with aperture radius; here it is clear that the value is always between 0.4 and 0.6, with no apparent trend. There is one clear exception to this for the WR-1.0 band, where it was requested that w and t were set to be equal. In Figure 4.37 the relationship between aperture radius and design wavelength (both in terms of central wavelength) can be seen. There is a general proportional relationship. Figure 4.38 indicates a linear relationship between design wavelength and central wavelength i.e. as the central wavelength increases, the design frequency gets closer to the high frequency end of a band. Finally, in Figure 4.39 the various dimensions of the two step transition are shown as functions of central wavelength. Clearly these values are very similar for each band, indicating that there exists a relationship for minimal return loss (as return loss was

the only metric for the rectangular to circular transitions) between wavelength and these dimensions, which is independent of the operating band.
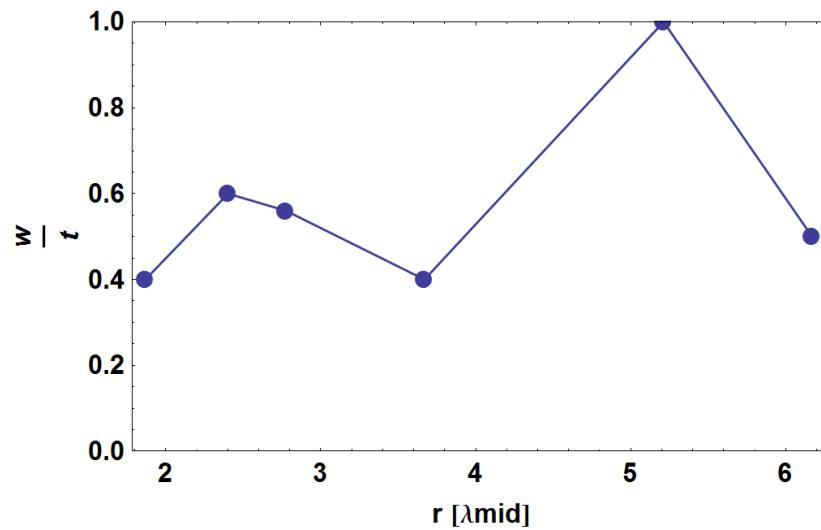
Figure 4.36: Ratio of slot width to ridge thickness as a function of aperture radius (in terms of central wavelength).
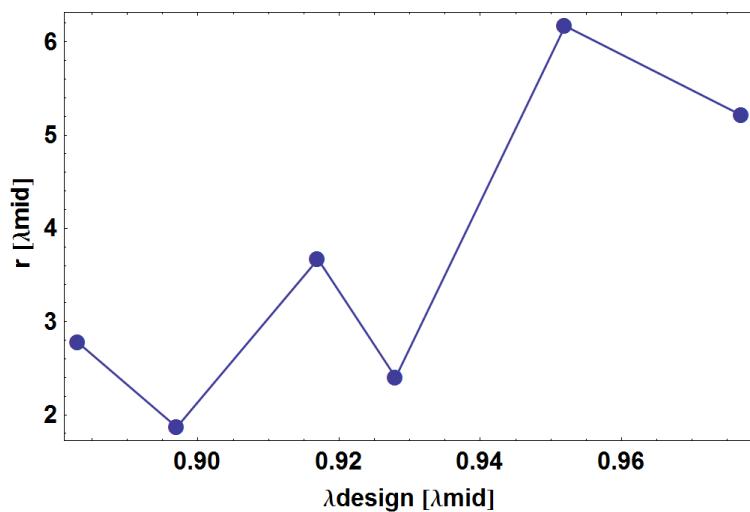

**Figure 4.37: Relationship between aperture radius and deign wavelength.**
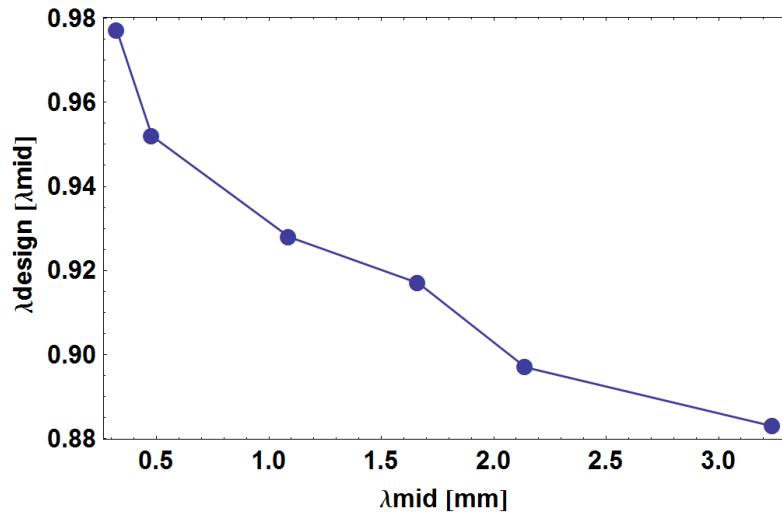
**Figure 4.38: Design wavelength as a function of central wavelength.**
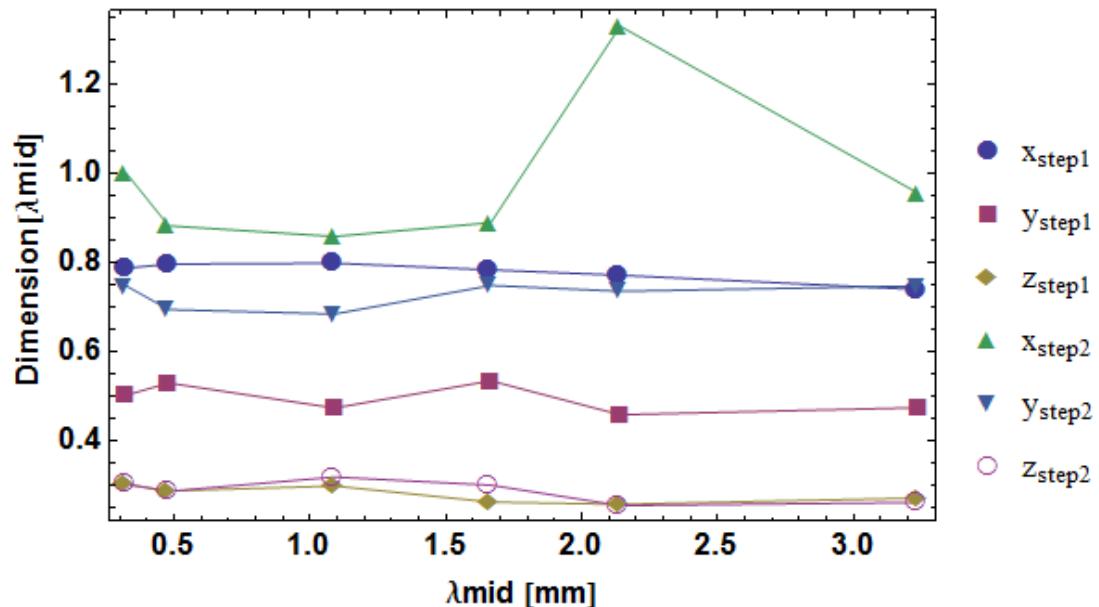
Figure 4.39: Various dimensions of the two-step transition as functions of central wavelength.

4.9 Tolerance analysis

A Monte Carlo simulation was performed where the radius of each section was modified by a random real number in the range $\pm 2\ \mu$m and the length of each section was varied by a random real number in the range $\pm 1\ \mu$m (as specified by SWISSto12 in (16)). This was done for three bands in order to examine the tolerance requirements as a function of frequency, and was prompted by results in Figure

4.28 discussed previously. The results of such analysis are shown in Figure 4.40, Figure 4.41 and Figure 4.42.

4.9.1 WR-1.0

The results of the tolerance analysis are shown in Figure 4.40. In this case it is clear that $\pm 2\ \mu$m is too large a tolerance to guarantee the desired performance.
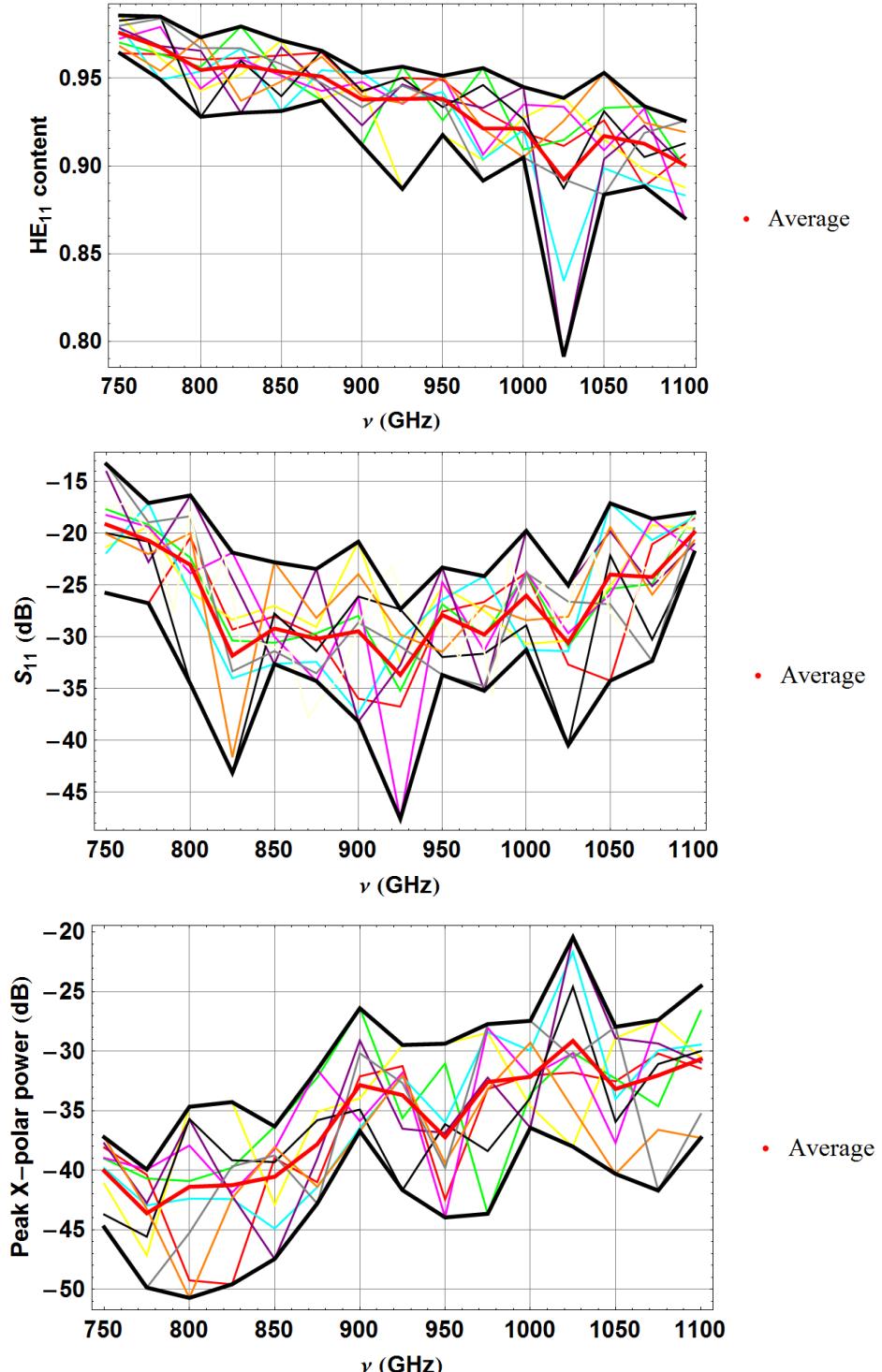

Figure 4.40: Monte Carlo tolerance analysis of the WR-1.0 band horn. The black lines are maximum and minimum values at each frequency

4.9.2 WR-6.5

The results of the tolerance analysis are shown in Figure 4.41. In this case it is clear that $\pm 2\,\mu$m is an acceptable tolerance to guarantee the desired performance for both HE_{11} and cross-polarization. The S_{11} is slightly above -20 dB at around 115 GHz and 170 GHz.
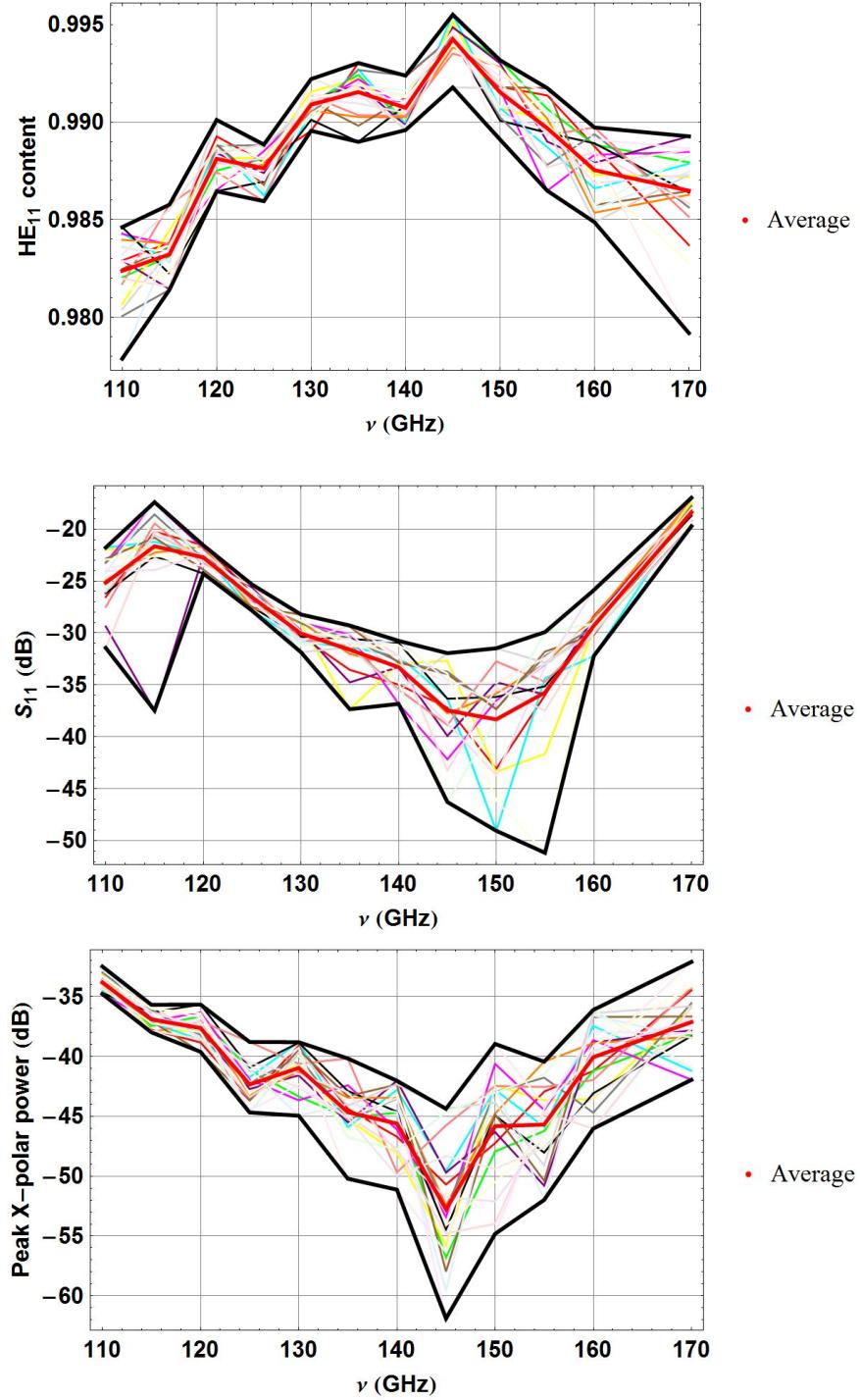
Figure 4.41: Monte Carlo tolerance analysis of the WR-6.5 band horn. The black lines are maximum and minimum values at each frequency

4.9.3 WR-10

The results of the tolerance analysis are shown in Figure 4.42. In this case it is clear that $\pm 2\,\mu$m (approximately 0.02λ) is an acceptable tolerance to guarantee the desired performance for HE_{11}, S_{11} and cross-polarization.
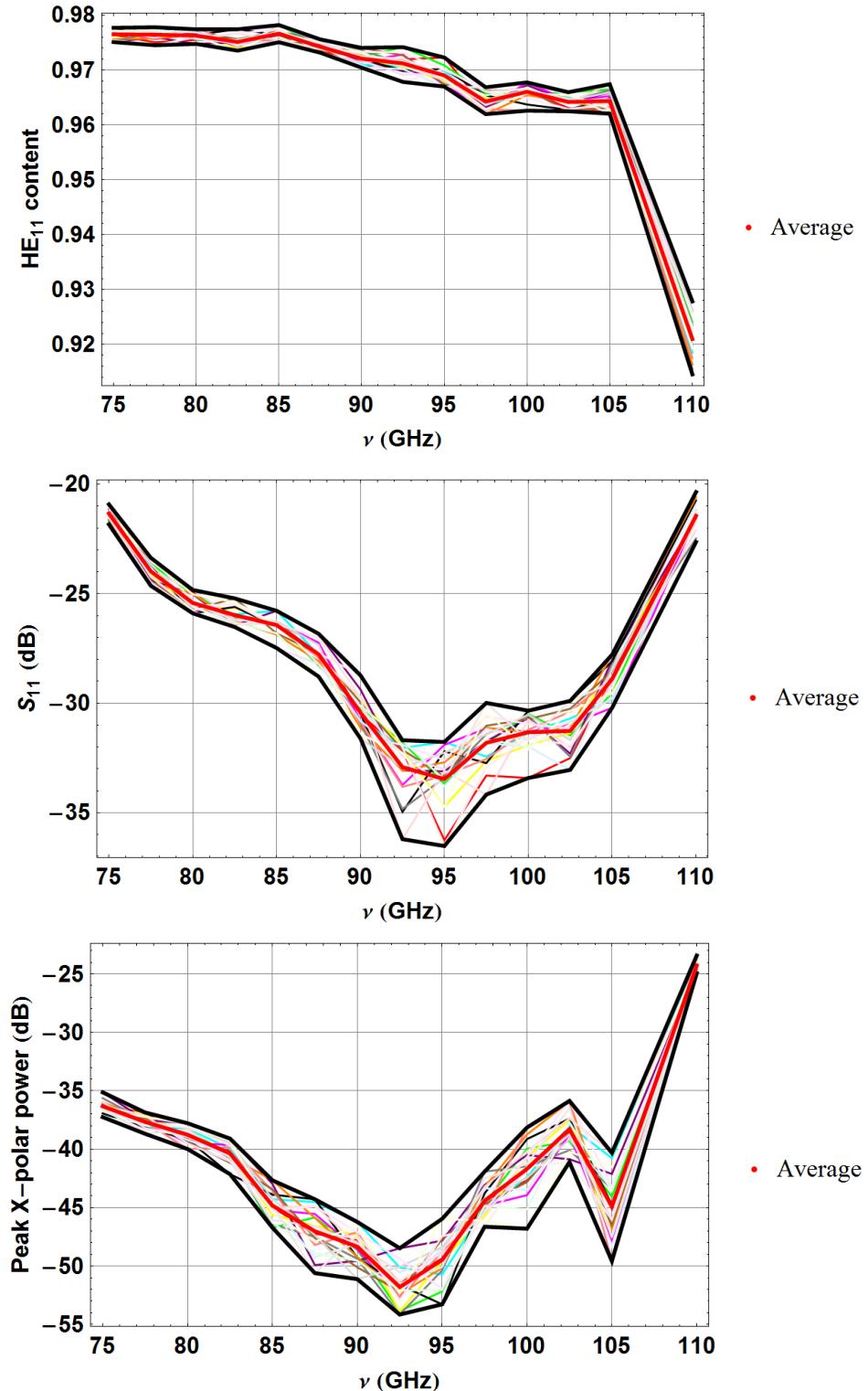
Figure 4.42: Monte Carlo tolerance analysis of the WR-10 band horn. The black lines are maximum and minimum values at each frequency

These three sets of plots demonstrate how, as would be expected, the effects of small deviations in the corrugation parameters become more important at high frequencies, as indicated by the increase in the black line "envelope" showing the deviation from the average value.

4.10   Conclusions

In this chapter there has been a discussion of the methods used to design nine corrugated feed horns. The goals of SWISSto12 for the performance of these horns were outlined. The design was broken into three separate transition stages: the rectangular to circular transition, the smooth-walled circular waveguide to corrugated horn transition and the corrugated horn throat to aperture transition. Two options for the design of the first stage were presented: firstly the step transition, consisting of two non-standard pieces of rectangular waveguide being placed between the WR guide and the circular waveguide, the dimensions of which are optimised using the parameter sweep and optimization abilities of CST, and secondly, the tapered transition, which takes a simpler approach but generates a structure which is difficult to manufacture. The tapered transition which replaces the two-steps of the step transition with a piece of waveguide whose cross-section changes from being rectangular (with the WR dimensions) at the WR guide interface to circular (with the dimension of the waveguide being coupled to) at the circular waveguide interface. For this second type of transition the only variable to be optimised is its length.

The second design stage again offered two general options: the Claricoats throat and the Zhang throat. Each throat takes its name from the original designers. The Claricoats throat uses a variable slot depth approach to form a good impedance transformer between smooth-walled and corrugated components. It begins with slot depths of half a wavelength at the interface and tapers these over 10 periods to slots that are 0.27 wavelengths deep at the design frequency while keeping a continuous flare angle. The Zhang throat also tapers the slot depths beginning at half a wavelength and ending at a quarter wavelength, however it is done linearly in this case. To improve the impedance transforming properties of the throat the ratio of ridge width to slot width is also tapered, beginning with a ratio of 7 (thick ridges,

thin slots) and finishing with a ratio of 0.25 (thin ridges, thick slots), this is subject to variation however depending on the aperture of the horn. The Zhang design was considered for ultra-broadband applications (WR+ bands), however it was deemed too difficult to manufacture and the Claricoats design was used instead, at the cost of a reduced bandwidth.

The final stage of the design is the horn antenna itself, which was done using a modified version of SCATTER that incorporated the generation of a geometry file. The various horn parameters were discussed with respect to the design goals i.e if a parameter was fixed or free. The design procedure for these parameters consists of an educated guess of parameters and then optimizing them with a parametric sweep analysis. As the project progressed, the author gained a better understanding of the complex inter-relationship between the parameters and a somewhat intuitive knowledge of sensible choices for the ranges considered for the parameter sweeps. Even still, the design work for this stage consisted of trial and error and continuous feed-back between parameters (finding local minima or maxima for a parameter, trying the next parameter, then perhaps the first parameter again etc.) until a design meeting the SWISSto12's criteria was found.

It was only after a horn had been designed that the rectangular to circular transition stage was designed. This was partly due to the relative speed of simulation in SCATTER when compared with CST, but also for the practical reason that the transition needed to couple not only to a smooth-walled circular waveguide but to a corrugated horn.

The chosen performance metrics of the designs and how they are calculated was discussed and the final dimensions of the horns were given and analysed in order to identify any potential design trends.

An example of the design procedure for the WR 1.0 band horn was given. This was followed by a Monte-Carlo analysis of the slot depths and widths and thicknesses for the purposes of investigating manufacturing tolerances. Included in this analysis is the effect of frequency on the tolerance requirements of a horn. It was shown

that (as one would expect) the tolerance requirement become more strict with increasing frequency, reaching 1 μm for the WR-1.0 band.

5. Measurements of WR-1.5 and WR-6.5 modules

This chapter will present results from measurements performed on several of the horns designed as part of this work. Although seven horns/convertor-modules have been designed to the specifications of SWISSto12, only two have been constructed so far, these are for the WR-1.5 and WR-6.5 bands. In this chapter there will be a discussion on the measurement results which have been received from SWISSto12 for the WR-1.5 and WR-6.5 bands and a comparison with simulation results. The first thing to describe is the measurement facility used in all cases: the vector network analyser.

The author would like to emphasise that he did not participate in any measurements, had limited access to measurement data and has no knowledge of the calibration methods or measurement set-up used. These results are preliminary only and should be viewed as such.

5.1 The vector network analyser

Vector network analysis is a measurement technique used to accurately characterise a device under test (DUT) by measuring its effect on the magnitude and phase of a swept-frequency signal. These measurements are performed using a port system similar to the one used by SCATTER, so for a two port system the DUT can be completely characterised by the four scattering parameters S_{11}, S_{12} S_{21} and S_{22}. Consider a DUT with an incident sinusoidal signal at port 1 and a response measured at port 2. This will lead to something like the situation in Figure 5.1:


Phase-difference: $\arg(S_{21})$

$|a|$

$|b|$

Amplitude-ratio:

$|S_{21}| = \dfrac{|b|}{|a|}$

— a
— b
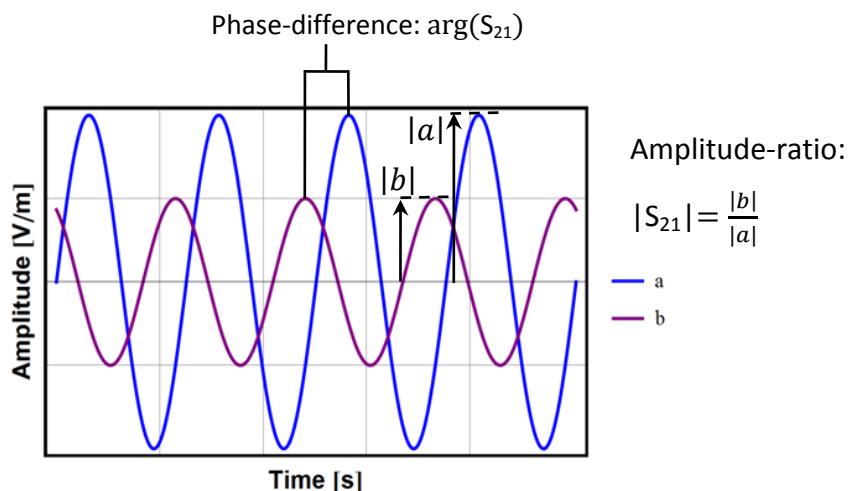
Figure 5.1: An example of a VNA measurement of (a), a sinusoidal signal incident at port 1 and the response signal (b) at port 2.

Figure 5.1 shows how the amplitude and phase of the signal have both been changed by the DUT. The scattering parameter S_{21} is a complex number containing information about the amplitude change and phase shift due to the DUT. In practice both phase and amplitude can be measured by using a heterodyne system, such as the one shown in Figure 5.2 (38).
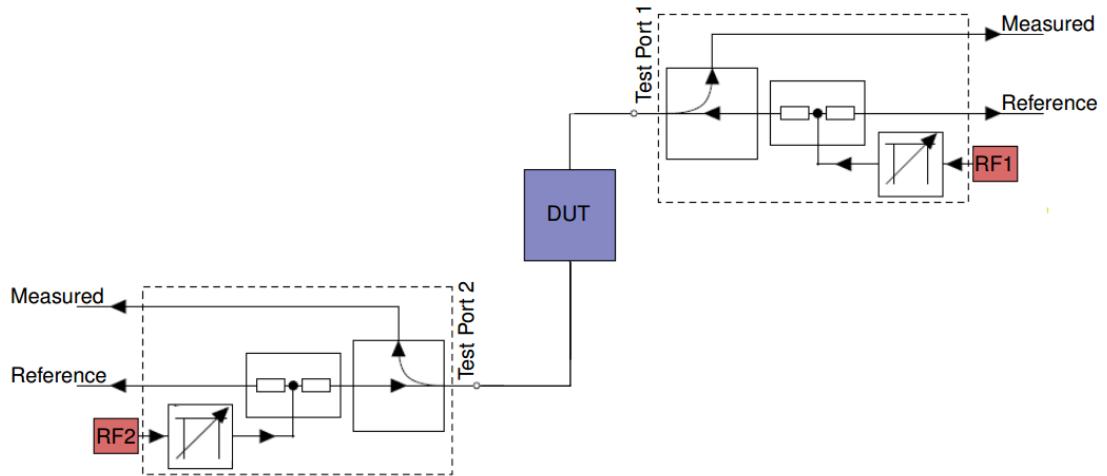

Figure 5.2: Example of a schematic of a heterodyne measurement system used in 2-port VNA.

A radio-frequency (RF) generator sends a signal to an attenuator which controls the total output power. From there the signal is split: one path leading to the reference channel, the other is sent to the DUT through port 1, this port also receives reflected signals from the DUT, which are sent to the measurement channel. The transmitted power is received at port 2 and sent to the second measurement channel. It is worth noting that both ports are transceivers.

So far this measurement only involves RF signals (which are easy to deal with using standard electronics). In order to reach the THz frequencies of interest here a frequency extension module must be used. A different frequency extension module is necessary for each of the WR bands. The RF signal is thus applied to the frequency extension module, where it is multiplied via frequency mixing, split and sent to the reference channel and DUT. Before being measured this signal's frequency is stepped back down so that standard electronics may be used, but it still contains the relevant information as we are only interested in changes in amplitude and phase due to the DUT, not absolute measurements.

5.2 WR-1.5 module measurements

The measurements of the WR-1.5 module were carried out in Lausanne, Switzerland by SWISSto12 using a Virginia Diodes VNA. The return loss (S_{11}) and radiation patterns of three stand alone (i.e. independent of the MCK) horns were measured, and their HE_{11} content was characterised. The measurement system is shown Figure 5.3 and one of the horns is show in detail in Figure 5.4.
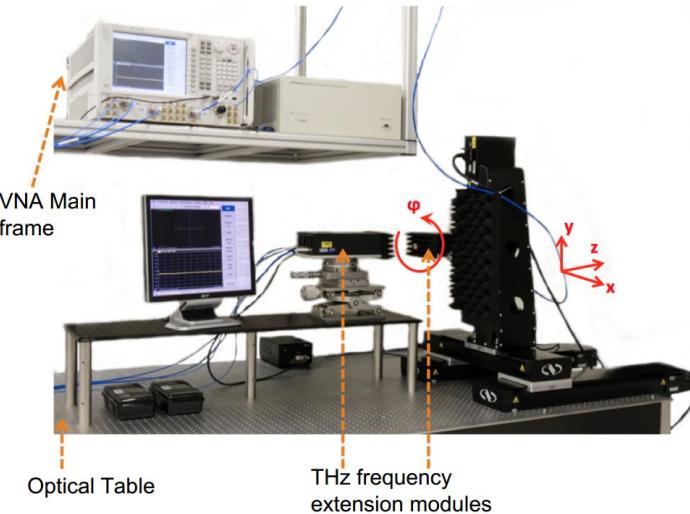

Figure 5.3: Measurement setup at SWISSto12's lab. (39)

Figure 5.4: WR-1.5 module horn (converter). Interface with WR-1.5 rectangular waveguide (left) and interface with corrugated waveguide/free-space (right).

The return loss measurements for two horns, overlaid with CST simulation data, are shown in Figure 5.5 where a similar trend is observed between the three data sets, with some clear discrepancies (measurements show a lot more structure). These discrepancies could be due to a plethora of factors such as VNA calibration, horn manufacturing tolerance, standing waves in the measurement system (deep nulls in the data) etc. Work remains to be done to properly account for these discrepancies.
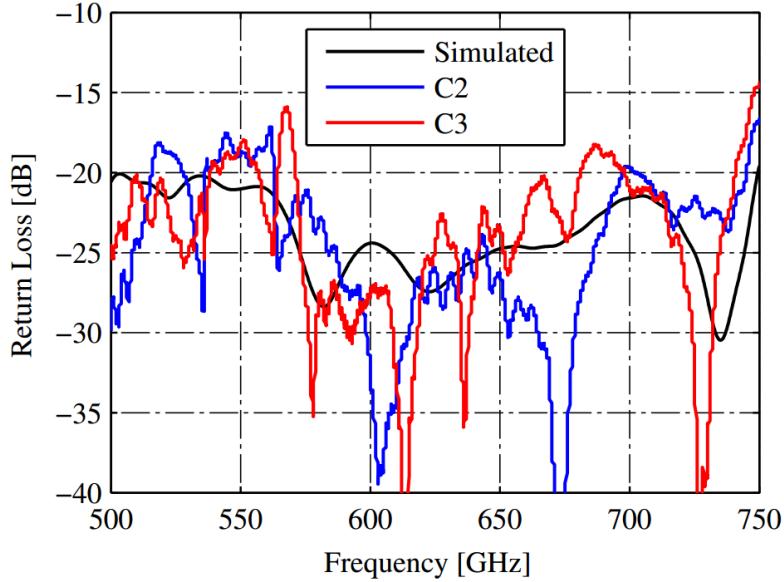
Figure 5.5: Measured and simulated (CST) return loss for the WR-1.5 design. (Measurement results for C1 were not available at the time of writing)

HE_{11} coupling was calculated by first measuring the radiation pattern on a 10 mm × 10 mm plane located 2.5 cm in front of the horn aperture, this was then back propagated to the aperture using the diffraction integral shown in (5.1). The results of the measurement and subsequent back propagation are seen in Figure 5.6:

$$u(x, y, z_i) = \frac{1}{2\pi} \iint u(x', y', z_j) \frac{\partial}{\partial z}\left(\frac{\exp(ikr)}{r}\right) dx' dy' \qquad (5.1)$$
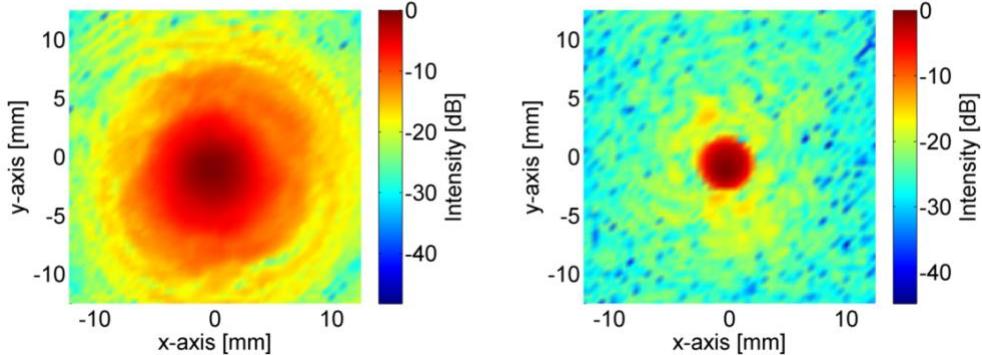
Figure 5.6: Measured (left) and back propagated (right) radiation pattern from a WR-1.5 horn design.

The HE_{11} coupling at the aperture plane can then be calculated following the method outlined in 4.6.2, replacing the simulated SCATTER field with the measurement data. This is a first-order measurement and further work is required

in refining the measurement procedure, in order to account for spurious effects such as standing waves between the horn and measurement probe, the effect of the beam pattern of the measurement probe itself, or stray light reflected from metallic surfaces in the lab etc. The results of this coupling analysis are shown in Figure 5.7. There are some disagreements between the three converters and simulated results, with the magnitude of this disagreement increasing with frequency, however the general trend predicted by simulation (i.e. decreasing HE_{11} coupling with increasing frequency) is seen for all measurements. In order to account for any degradation in performance due to manufacturing tolerances a Monte-Carlo analysis of the effect of changing the radius of each section by a random real number in the range $\pm 2\,\mu$m (the resolution of the machining of the rings (16)) was performed. The effect of this is seen in coloured lines in the bottom plot of Figure 5.7. The black line is the result of a simulation assuming perfect manufacture and is the same as seen in the top plot.
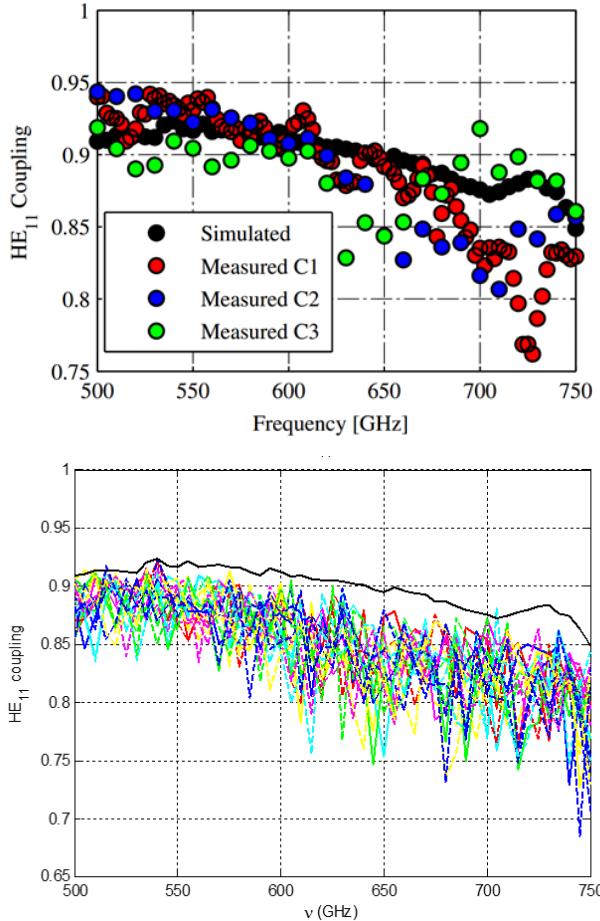

Figure 5.7: Measured and simulated HE_{11} coupling across the band for the WR-1.5 design (top) and a Monte-Carlo analysis of the tolerancing effects of the individual ring radii (bottom). (C1, C2 & C3 refer to converter 1,2 & 3).

114

The range of HE_{11} coupling values for realisations manufactured to a tolerance of 2 μm is very similar to the measured range: The difference being around 0.05 at 500 GHz increasing to around 0.15 at 750 GHz, which is promising. However the measurements occasionally show an increase in HE_{11} coupling compared to the ideal simulations, while the Monte-Carlos analysis predicts a clear decrease. This issue is yet to be resolved fully, but with an improved measurement procedure this should be accounted for. Overall the measurements and simulation are showing good agreement, indicating that tighter tolerance requirements may need to be applied in order to reach the desired performance levels. As seen in section 4.9 these tolerance requirements are expected to be loosened for the lower frequency bands.

Finally, a comparison was made between the measured near-field data and a CST simulation. In order to retrieve the electric field information in CST at a plane 25 mm away from the aperture plane, a piece of vacuum 25 mm $\times$ 10 mm $\times$ 10 mm was placed in front of the horn, with an electric field monitor at the end, as shown in Figure 5.8. The results from this comparison can be seen in Figure 5.9.
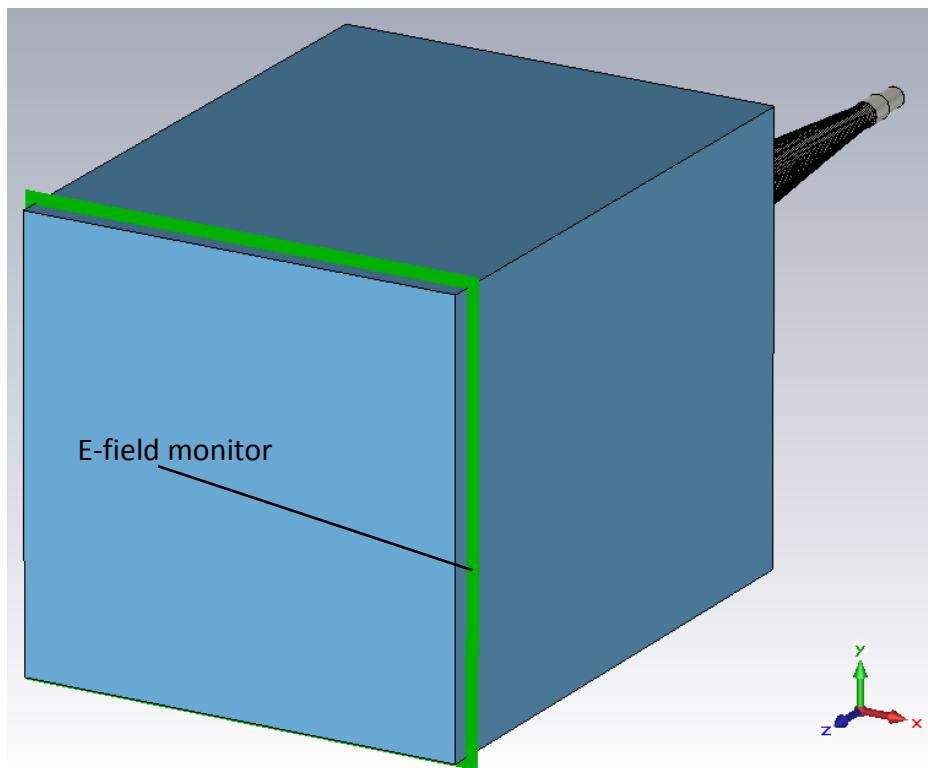

Figure 5.8: CST setup for near-field calculation at a plane 25 mm from the aperture.
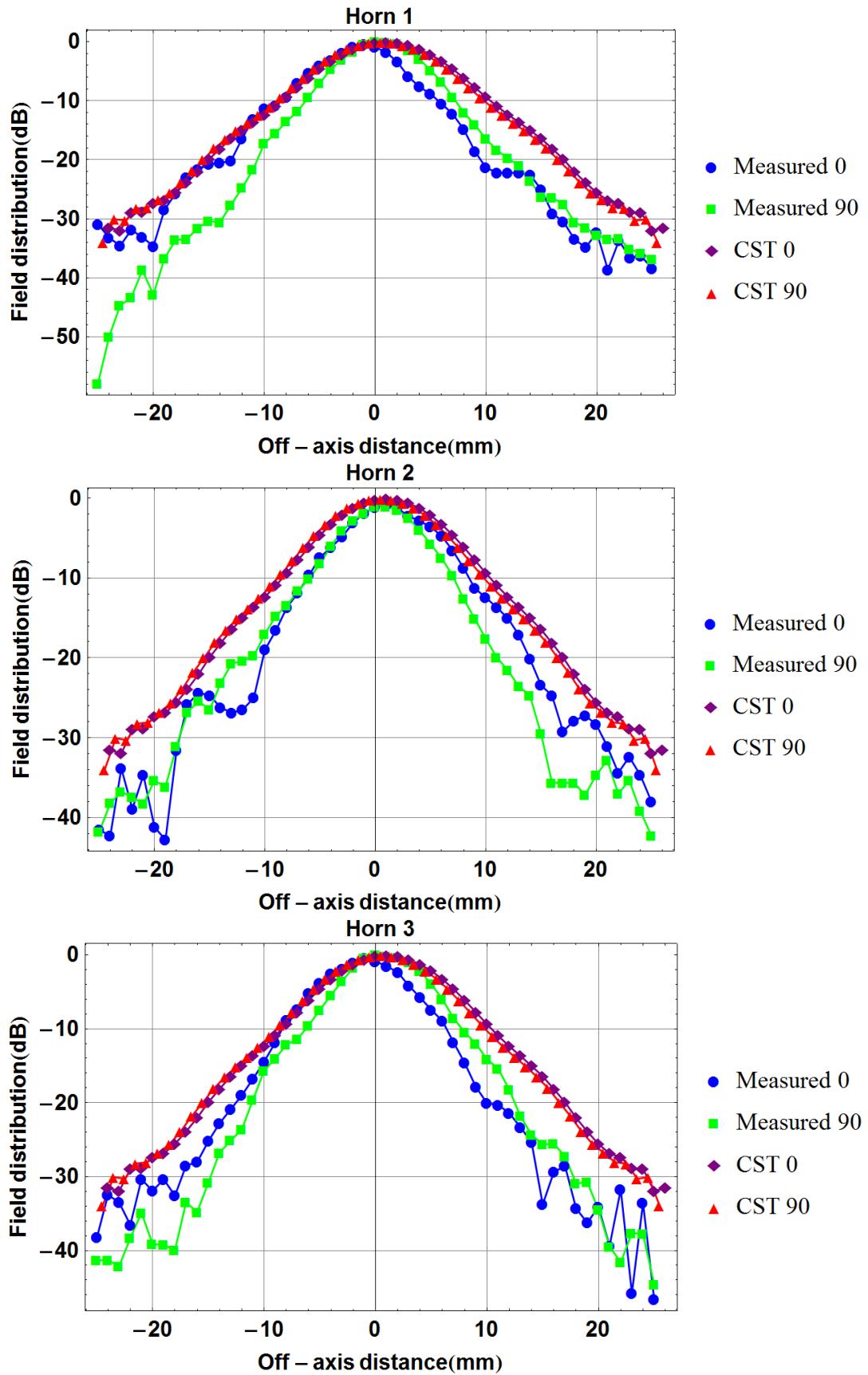
Figure 5.9: Measured and simulated radiation patterns for three WR-1.5 horns. "Measured 0" refers to a 0° (E-plane) cut of the radiation pattern, "Measured 90" refers to a 90° (H-plane) cut of the radiation pattern, etc.

Again, there are clear differences between measurements and simulation, as well as being due to factors outlined previously, the directionality of the measurement probe has a large role to play in radiation pattern measurements. It is not really measuring a single point in the field but has a beam-pattern itself which must be considered. The author would like to reiterate the preliminary nature of these measurements.

5.3 WR-6.5 module measurements

The WR-6.5 module has so far only been considered for use with the Material Characterisation Kit (MCK) and so no radiation pattern measurements have been performed, meaning that the HE_{11} coupling has yet to be measured. However both the return loss and insertion loss have been measured, again this was done by SWISSto12 in Lausanne.

5.3.1 WR-6.5 return loss

The return loss measurements for two manufactured horns are shown in Figure 5.10, including the simulated results from CST. Again there are major disagreements between the data sets, especially in terms of the peaks and nulls, these are likely caused by similar factors outlined in section 5.2. The overall levels however are in general agreement, with the measured data largely remaining below the -20 dB requirement.
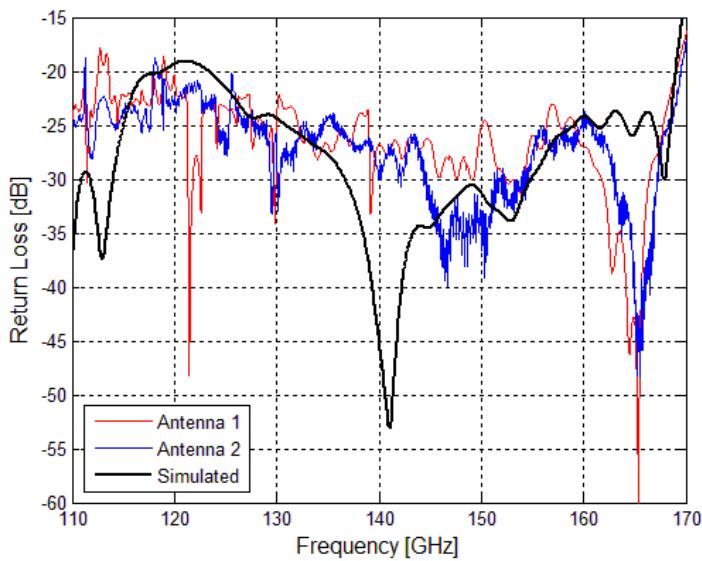

Figure 5.10: WR-6.5 antenna return loss measurements and CST simulation.

5.3.2 WR-6.5 insertion loss

Insertion loss is the loss in transmitted power, not caused by reflections. The general mechanism for insertion losses in the case of a corrugated horn such as those considered here is Ohmic losses due to the finite conductivity of the antenna walls; the rapidly varying electric and magnetic fields induce eddy-currents in the walls leading to Joule heating, thus power is dissipated in the form of heat. This is another reason it is desirable to contain as much power as possible on axis in the horn, as there will then be less power available at the walls to create these eddy-currents.

The insertion loss results are shown in Figure 5.11, again including measurements and simulation. The insertion loss measurements were performed by placing a reflector at the aperture of the antenna and measuring the S_{11} on a VNA. In this setup if the antenna was made from PEC it would be expected that all power would be reflected and the S_{11} should be at 0 dB across the band. Any deviation from this is due to the insertion loss.
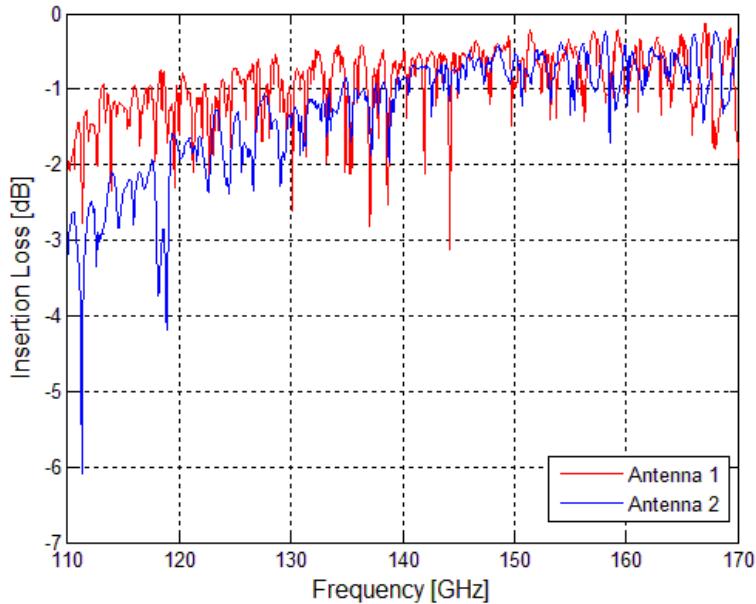

Figure 5.11: Insertion loss measurements for two horns. Better time-gating parameters were chosen for the top plot. Better insertion loss was recorded for the bottom plot. No CST simulation data is available here due to limited computational resources at the time.

The insertion loss is worse at the low frequencies for Antenna 2 here due to some of the rings not being manufactured properly by SWISSto12's supplier. The measured data here appears quite noisy, this is because of the way the

118

measurements were taken with the reflector covering the horn aperture. In this setup the antenna will behave somewhat like a resonating cavity, causing some power to be reflected multiple times before being measured. Due to the difference in time of arrival of these signals and the desired measurement signal it is possible to filter them from the data using a technique known as time-gating. In order to perform this technique the frequency data must be inverse-Fourier-transformed into the time-domain; a window function is then used to filter out signals outside of the time measurement band of interest. Finally the data is Fourier transformed back in to the frequency domain, leading to the smooth curve shown in Figure 5.11, (40). Another method of improving the noisy data is to reduce the bandwidth of the VNA and increase the averaging. The noise is also dependant on calibration and settings. An example of time-gating done on the WR-6.5 horn measurement data by the author in order to better understand the process will now be given.

5.3.3 Time-gating

An array containing linear amplitude data in the frequency domain can be discrete-inverse-Fourier-transformed into the time domain using Mathematica's *InverseFourier* function. Figure 5.12 shows this for WR-6.5 insertion loss measurements.
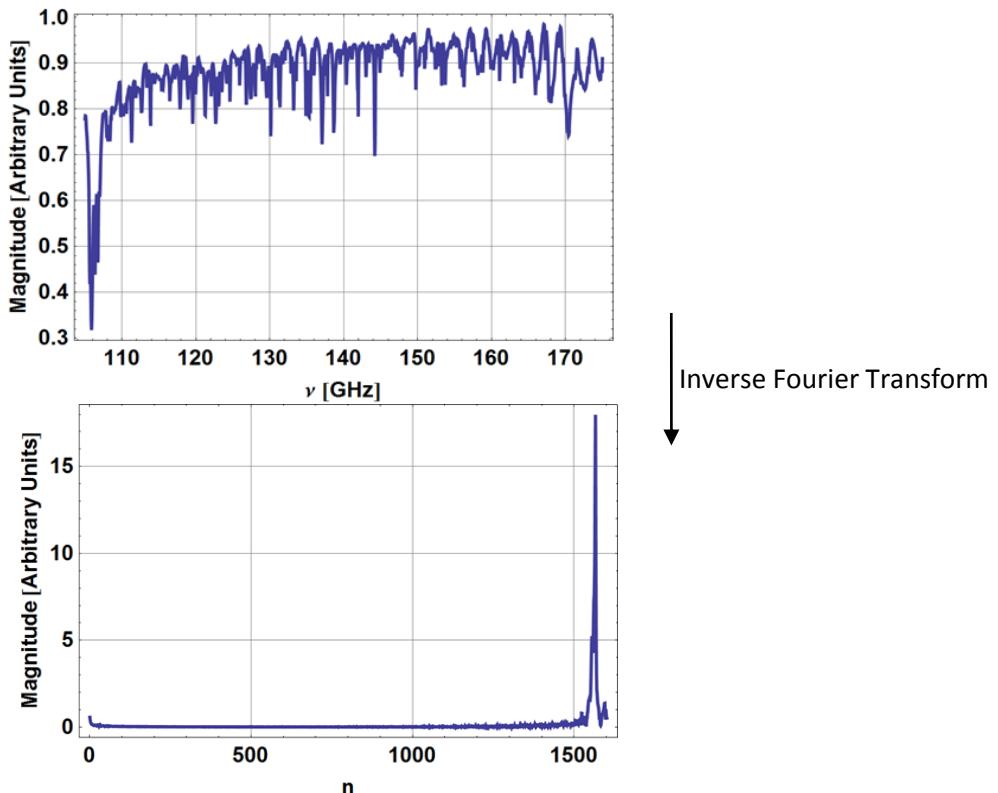

Figure 5.12: Inverse Fourier transform performed in WR-6.5 insertion loss measurement data. The variable n is explained in the text.)

119

From this it is clear that in the time domain there is a sharp impulse response, this is caused by the first round-trip reflection of the signal, there are several smaller ripples around this peak, these are caused by the secondary reflections, and it is this effect that we want to remove. Before discussing how this is done, it is worth noting that the independent variable of the bottom plot in Figure 5.12 (**n**) is in terms of time "bins" rather than units. In order to convert this to units of seconds we must use (5.2), leading to Figure 5.13.

$$t(n) = \frac{n}{N \Delta N} \tag{5.2}$$

where N is the number of data points and ΔN is the measurement step size.
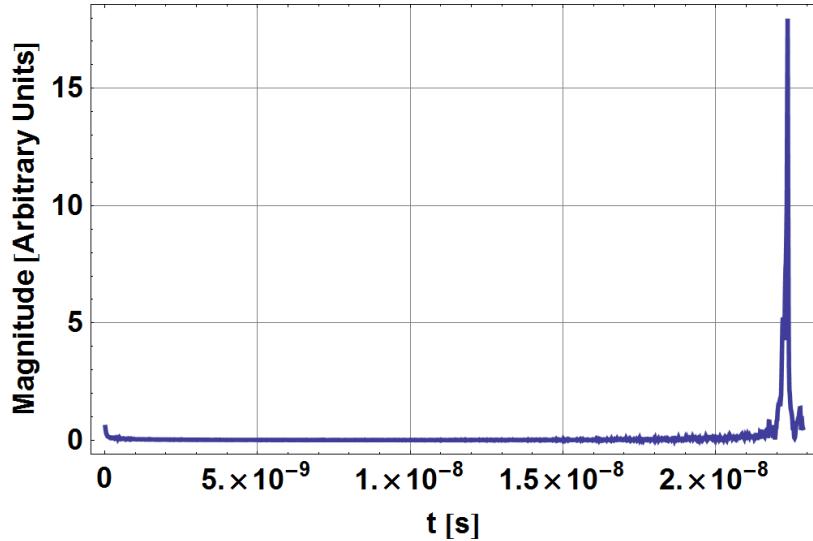

Figure 5.13: Inverse Fourier transform of WR-6.5 measurement data, in terms of time.

In order to remove the unwanted time signals we can implement a window function. A window function is essentially a way of reducing data outside of the region of interest to zero. There are many window functions available, which all have associated advantages and disadvantages depending on the scenario. A standard window function is the Hann or Hanning window, given in equation (5.3), which is taken from (41). A plot of a Hanning window is shown in Figure 5.14.

$$w(n) = 0.5 - 0.5\cos\left(\frac{2\pi n}{N}\right), for\ n = 0,1,2,\dots N - 1 \tag{5.3}$$

where, N is the width of the window in terms of samples.
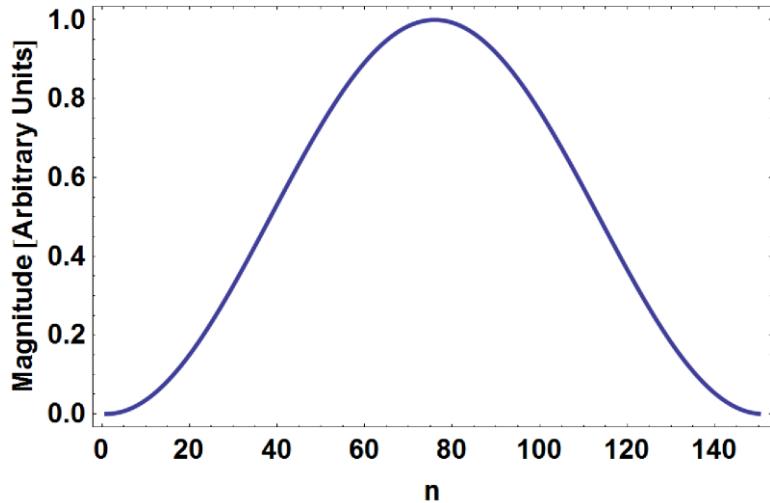
Figure 5.14: Hanning Window, N=150.

This function will have the effect of smoothly reducing the data around the peak to zero, clearly the width of the window (determined by the choice of N) will have an important impact on the effectiveness of the window function. Care must also be taken to align the window to the correct region of the data set. A window function can be applied to the data using (5.4), (41). That is, multiply the two functions and perform a discrete Fourier transform.

$$X_w(m) = \sum_{n=0}^{N-1} w(n)x(n)e^{-\frac{j2\pi nm}{N}} \tag{5.4}$$

where, N is the width of the window in terms of samples. Multiplying this window by the data shown in Figure 5.12 (lower plot) with $N = 50$ leads to Figure 5.15. There are clearly still some ripples at the higher end of the scale, due to the asymmetry of the time response. Now, Fourier transforming this back into the frequency domain leads to Figure 5.16.
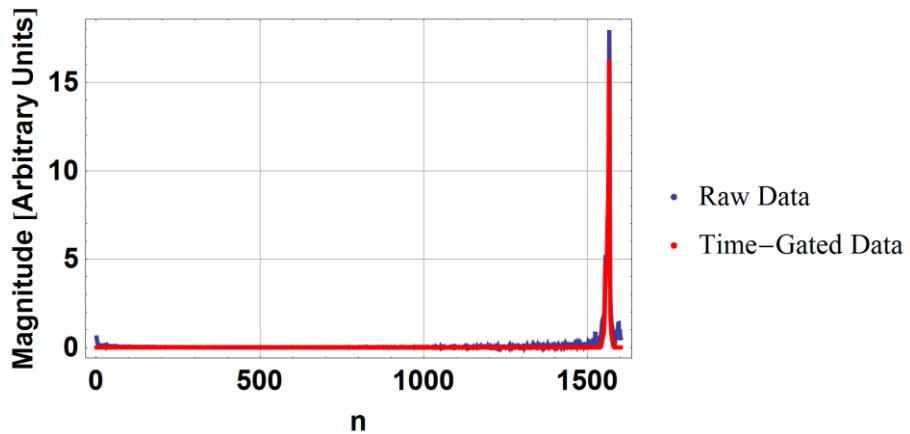

Figure 5.15: Comparison of raw data from Figure 5.12 with the same data after multiplication by the window function.

121
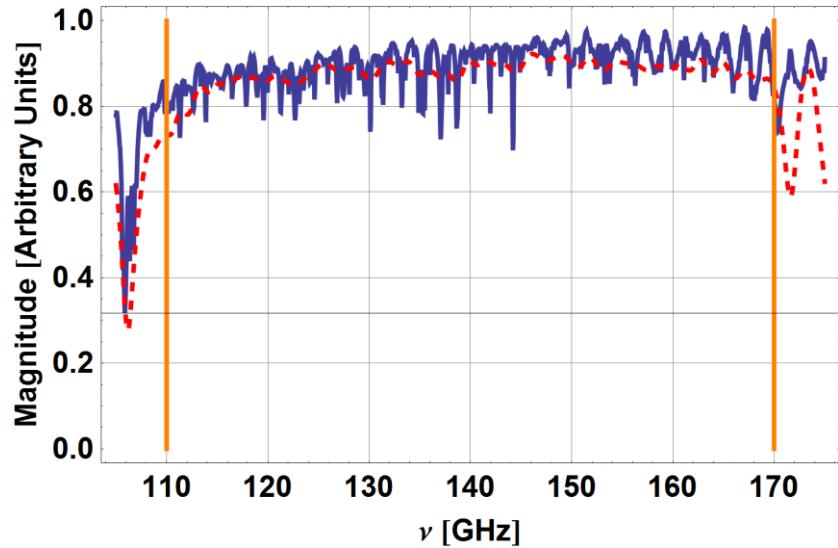
Figure 5.16: Time-gated data (red) overlaid on measured data (blue). The orange lines mark the edges of the WR-6.5 band.

The time-gated data is clearly smoother than the raw data with much of the variations due to multiple reflections removed. Increasing the measurement sampling rate or investigating other window functions could improve this technique further.

The raw data with overlaid time-gated data curves for both antennas are shown in Figure 5.17 and Figure 5.18.
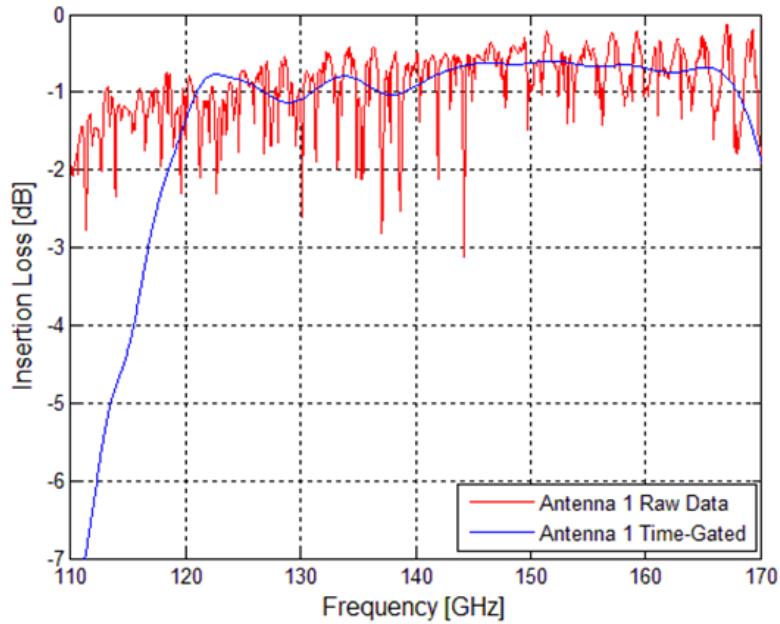

**Figure 5.17: Raw and time-gated data for Antenna 1.**

122
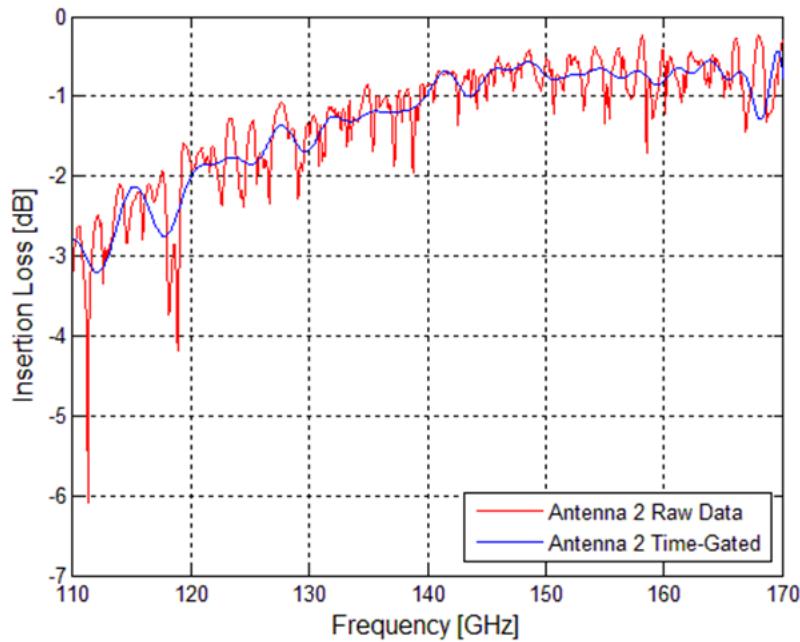
Figure 5.18: Raw and time-gated data for Antenna 2.

The time-gated data for Antenna 1 is an example of poor of time-gating parameters, while the time-gating parameters for Antenna 2 were chosen more appropriately.

5.4 Conclusions

This chapter considered aspects of measuring the properties of corrugated horn antennas as well as measurement results from three designs presented in Chapter 4. It also contained a description of a vector network analyser and its measurement capabilities i.e. amplitude and phase of an EM wave. This was followed by some results from the measurements of the near-field properties of a WR-1.5 horn, which were numerically back-propagated to the aperture plane of the horn using diffraction integrals. These aperture fields were used to calculate the measured HE_{11} coupling coefficient values at various frequencies in the band. Return loss measurements were also given. A comparison between measurement and simulation was given for all of these results and a Monte-Carlo analysis of the tolerancing requirements was performed to try and account for discrepancies in the measurement data.

Some results from insertion loss and return loss measurements for a WR-6.5 band horn are also described, again including some comparisons between measurements

123

and simulation for the return loss measurements which were in good agreement. There was also an explanation and example of time-gating on the insertion loss measurements.

6. Final summary and conclusion

This thesis was primarily concerned with the development of high-performance corrugated conical horn antennas for use in the THz region of the electromagnetic spectrum. They are fed by a smooth-walled circular waveguide which transition to an industry standard WR-band rectangular waveguide for use in vector network analysis experiments (VNA). These antennas will be built by the company SWISSto12 and will serve the dual purpose of acting as free-space radiators or as crucial components in SWISSto12's material characterisations kits (MCK), where they bridge the gap between the VNA frequency extension module rectangular WR-band guides and a cylindrical corrugated waveguide containing a sample for measurement.

Chapter 1 was an introduction to THz radiation, with some context given to its place in the electromagnetic spectrum and how we must borrow techniques from the microwave and optical regions to manipulate and model it. The many applications of THz were mentioned with emphasis on astronomical applications and security and medical imaging. The research interests of SWISSto12 were discussed in some detail, and the novelty of their 'stacked ring' approach to building corrugated waveguides was described. The utilization of these waveguides in plasma physics experiments and in SWISSto12's own MCK was also outlined and the role of the author in designing the horn antenna components for these kits was detailed. Another innovative manufacturing process used by SWISSto12 for building inexpensive high-quality passive elements (stereolithography (3D printing) combined with a metallic plating technique to create light-weight waveguide and smooth-walled horn antennas) was then described.

Chapter 2 contained a description of the operation of circular and rectangular waveguides, including a derivation of the circular TE and TM modes. The use of waveguides as horn antennas was introduced followed by the concept of hybrid modes and the importance of the HE_{11} mode in particular. I showed how the relative contribution of TE_{11} and TM_{11} modes propagating in a guide can be adjusted to minimize levels of cross-polar power. Two methods for generating a HE_{11} mode

were outlined, these were the Potter horn and the corrugated cylindrical waveguide.

Chapter 3 contained the analysis methods used in this thesis for the design of waveguides and corrugated conical horn antennas. These were: the surface impedance model (including the hybrid mode model), the mode-matching technique for corrugated horns, which was employed in the in-house software package SCATTER, and the finite integration technique as used by the commercially available simulation software CST: Microwave Studio. Examples from SWISSto12 horns and the Planck telescope were used to illustrate the techniques.

Chapter 4 described the design process for the horn components which were a major element of this work. The design requirements were outlined (HE_{11}, S_{11} and cross-polar content) and the design process was broken into three stages. These were: the rectangular to circular transition, the circular to corrugated transition and the corrugated waveguide to free-space/large-diameter corrugated waveguide. Two possible types of transition for the rectangular to circular (two-step or smooth) and circular to corrugated (Claricoats or Zhang) sections were outlined. The important elements to consider when designing a corrugated horn antenna, such as the geometric-profile and period of corrugations were discussed. Next the full design procedure was described, including the method of parametric sweep analysis for designing a corrugated horn and the specific performance metrics and how they were calculated. An example of a design for the WR-1.0 band was given next. This was followed by the final design parameters for each of the horns (WR-1.0, WR-1.5, WR-3.4, WR-3.4 for EPFL, WR-5.1, WR-6.5, and WR-10) and a presentation of the final return loss and HE_{11} content. The requirement of HE_{11} content greater than 92% across the band was met for all of the designs apart from the WR-1.5 band. The WR-1.5 design was the first one developed, and this was before HE_{11} content had become a critical factor. The return loss requirement of less than -20 dB across the band was also realised for each band except the WR-6.5 which rises above this value at two spots in the band at around 122 GHz and 168 GHz. The S_{11} for two ultra-low return loss horns designed for the WR-6.5+ and WR-10+ bands was then shown, with a value below -25 dB across the bands. An analysis of the geometries of

the horns and step transitions was performed in order to find possible trends which may be of use to future designers and the results of this were presented with several trends identified. These trends include a relationship between horn length and the central wavelength of a band, a small range of optimum values for the ratio of slot width to ridge width for each of the designs, a linear relationship between design wavelength and central wavelength and also fairly constant relationship between the dimensions of the step-transition and central wavelength of a band. Finally an examination of the effect of manufacturing tolerances of the ring radii on the performance of the horns using a Monte Carlo analysis was presented for three of the WR-bands, showing how the tolerance requirements increase with frequency. A tolerance of $\pm 2\mu m$ was acceptable for the WR-6.5 and WR-10 bands, however it was not good enough to guarantee the desired performance for the WR-1.0 band.

Some measurements of the horns which have been built so far were discussed in Chapter 5, which began with a description of a VNA. The measured return loss and HE_{11} content of the WR-1.5 band horn as well near-field radiation patterns at three frequencies across the band were compared with SCATTER and CST simulations, showing good agreement. The return loss measurements for the WR-6.5 band horn were also compared with simulation and show good agreement as well. The insertion loss measurements were shown and the procedure of time-gating on these was described using an example.

In conclusion: 9 individual corrugated conical horns with rectangular to circular transitions were designed to meet the criteria set by SWISSto12 (HE_{11} coupling, return loss and cross-polarization), and the components which have been manufactured and measured so far show promising performance.

6.1 Future work

Some potential future work will now be considered. The code used during the horn design process could be implemented as a starting point to build a general horn design programme with a user interface, where the user specifies some requirements for the horn's performance (e.g. bandwidth, gain, peak cross-polar

power, Gaussicity, HE_{11} content, return loss, side-lobe level, etc), restrictions on its geometry and a parameter to be swept over or optimized. This would be a very useful tool which would speed up the design process.

There currently exist two versions of SCATTER: one for cylindrical waveguides and one for rectangular waveguides, however there is no way to combine them. Such a combination would allow for design of the rectangular to circular transitions in SCATTER, speeding up the simulation time compared to CST. The irregular shaped boundary at the rectangular-circular interface prevents closed-form solutions to the power coupling integrals at this plane, i.e. we cannot analytically solve the power-coupling integrals between a rectangular and circular mode-set. It can be solved analytically but this takes longer than a CST simulation. However, by transforming from a surface integral to a line integral along the edge of the boundary it may be possible to match or even improve on the speed of CST. This is one of the current projects at Maynooth University.

Finally, only two of the designs (WR-1.5 and WR-6.5) in this thesis have been built and tested. Further work on the measurement procedure for forthcoming horns will provide more accurate results on their modal content, return loss and radiations patterns etc.

7. **Bibliography**

1. **C. O' Sullivan, J. A. Murphy.** *Field Guide to Terahertz Sources, Detectors and Optics.* Bellingham : SPIE, 2012.

2. *Coherent Manipulation of semiconductor quantum bits with terahertz radiation.* **B. E. Cole, J. B. Williams, B.T. King, M.S. Sherwin, C.R. Stanley.** 2000, Nature, Vol. 410, pp. 6 0- 63.

3. *Tranmission Line Technology for Electron Cyclotron Heating.* **J. L. Doane.** 1, 2008, Fusion Scence and Technology, Vol. 53, pp. 39 - 53.

4. *High Field Dynamic Nuclear Polarization- The Renaissaince.* **R. G. Griffin, T. F. Prisner.** 2010, Physical Chemistry Chemical Physics, Vol. 12, pp. 5737 - 5740.

5. *Searching for Terahertz Waves.* **X. C. Zhang.** 9, London : Nature, 2010, Nature Photonics, Vol. 4, p. 662. ISSN - 1749-4885.

6. *Materials for Terahertz Science and Tecnhology.* **B. Ferguson, X. C. Zhang.** 14, 2002, Nature Materials, Vol. 1, pp. 26 - 33.

7. *Plasmonics: Superfocusing of Terahertz Waves.* **M.B.Johnston.** 1, London : Nature, 2007, Nature Photonics, Vol. 1, pp. 14-15. ISSN - 1749-4885.

8. *Security Applications of Terahertz Technology.* **M. C. Kemp, P. F. Taday, B. E. Cole, J. A. Cluff, A. J. Fitzgerald, et al.** Orlando : SPIE, 2003. Terahertz for Military and Security Applications. Vol. 5070, pp. 44 - 52. ISBN - 9780819449290.

9. *Herschel Mission Overview and Key Programmes.* **G. L. Pilbratt.** San Diego : SPIE, 2008. Space Telescopes and Instrumentation: Optical, Infrared, and Millimeter. Vol. 7010, pp. 1-12. ISBN - 9780819472205.

10. Herchel Spce Observatory. [Online] [Cited: 5th August 2015.] http://www.herschel.fr/cea/star-formation/en/.

11. **M. Whale.** *Optical Characterisation of Astronomical Submillimetre Receivers including ALMA Bands 5 and 9.* Maynooth : National University of Ireland, Maynooth, PhD thesis, 2010.

12. Attacama Large Milimetre Array. [Online] [Cited: 17th August 2015.] http://www.almaobservatory.org/en/visuals/images/astronomy/?g2_itemId=3431.

13. **Planck Collaboration.** Planck 2015 results. XIII. Cosmological Parameters. Ithica : ArXiv, 2015.

14. European Space Agency. [Online] [Cited: 12th August 2015.] http://www.esa.int/spaceinimages/Images/2013/03/Planck_CMB.

15. Teraview. [Online] [Cited: 17th August 2015.] http://www.teraview.com/applications/index.html.

16. *Note: Stacked rings for terahertz-wave guiding.* **E.de Rijk, A. Macor, J-Ph. Hogge, S. Alberti, J-Ph. Ansermet.** 6, Melville : AIP Publishing, 2011, Review of Scientific Instruments, Vol. 82.

17. SWISSto12. [Online] [Cited: 10 December 2015.] http://www.swissto12.ch/Products/Material%20Characterisation%20Kit/index.html
.

18. *Note: Three-dimensional stereolithography for millimetre wave and terahertz aplications.* **A. Macor, E. de Rijk, S. Alberti, T. Goodman, J.P. Ansermet.** 4, Melville : AIP Publishing, 2012, Review of scientific instruments, Vol. 83.

19. **P. C. Magnusson, Andreas Weisshaar, Vijai K. Tripathi, Gerald C. Alexander.** *Tansmission Lines and Wave Propogation, Fourth Edition.* London : CRC Press, 2001.

20. **N.J. Cronin.** *Microwave and Optical Waveguides.* London : Institue of Physics Publishing, 1995.

21. **D.Jackson.** Fourier Series and Orthogonal Polynomials. [book auth.] Dunham Jackson. *Fourier Series and Orthogonal Polynomials.* Oberlin : The Mathematical Association of America, 1941, p. 86.

22. **P.J.B Claricoats, A.D.Olver.** *Corrugated horns for microwave antennas.* London : Peter Peregrinus Ltd, 1984.

23. **P. D. Potter.** *A New Horn Antenna with Suppressed Sidelobes and Equal Beamwidths.* Pasadena : Internal Report: NASA, Jet Propulsion Laboratory, 1963.

24. *Characterization of a Dual-Mode Horn for Submillimeter Wavelengths.* **H. M. Pickett, J. C. Hardy, J. Farhoomand.** 8, New York : IEEE Publishing, 1984, IEEE Transactions on Microwave Theory and Techniques, Vol. 32, pp. 936 - 937. ISSN: 0018-9480.

25. **P. F. Goldsmith.** *Quasioptical Systems.* New York : Institue of Electrical and Electronic Engineers, 1998.

26. CST - Computer Simulation Technology. *CST-Computer Simulation Technology Web Site.* [Online] [Cited: 07 September 2015.] https://www.cst.com/.

27. *Design of Conical Corrugated Feed Horns for Wide-Band High-Frequency Applications.* **X. Zhang.** 8, New York : IEEE Publishing, 1993, Transactions on Microwave Theory and Techniques, Vol. 41, pp. 1263-1274.

28. **R. Colgan.** *Electromagnetic and quasi-optical modelling of horn antennas for far-IR space applications.* Maynooth : National University of Ireland Maynooth, Ph.D Thesis, 2001.

29. **E. Gleeson.** *Single and multi-moded corrugated horn design for cosmic microwave background experiments.* Maynooth : National University of Ireland, Maynooth, PhD Thesis, 2004.

30. **A.D. Olver, P.J.B. Claricoats, A.A.Kishk and L. Shafai.** *Microwave Horns and Feeds.* New York : IEEE Press, 1994.

31. *Optical modelling offar-infrared astronomical instrumentation exploiting multimode horn antennas.* **C. O'Sullivan, J. A. Murphy, I.McAuley, D. Wilson, M. L. Gradziel, N. Trappe, F. Cahill, T. Peacocke, G. Savini, K. Ganga.** Montreal : SPIE, 2014. Millimeter, Submillimeter, and Far-Infrared Detectors and Instrumentation for Astronomy VII. Vol. 9153.

32. *Discrete Electromagnetism with the Finite Integration.* **M. Clemens, T. Weiland.** : Progress in Electromangetics Research, 2001, Progress in electromagnetic research, Vol. 32, pp. 65-67.

33. **S.Doherty.** *Optical and Quasi-Optical Design and Analysis of Astronomical Instrumentation including a Prototype SAFARI Pixel.* Maynooth : National University of Ireland, Maynoth, Ph.D Thesis, 2012.

34. *Analysis of TE11 - to HE11 Corrugated Cylindrical Waveguide Mode Convertors.* **G. L. James.** 10, New York : IEEE Transactions on Microwave Theory and Techniques, 1981, IEEE Transactions on Microwave Theory And Techniques, Vol. 29, pp. 1059 - 1066.

35. *Improved Radiation Pattern Perfromance of Gaussian Profiled Horn Antennas.* **R. Gonzalo, Jorge Teniente and Carlos del Rio.** 11, : IEEE Transactions of Antennas and Propagation, 2002, IEEE Transactions on Antennas and Propagation, Vol. 50, pp. 1505-1513.

36. *Profile Options for Feed Horn Design.* **C. Granet.** Sydney : IEEE, 2000. Microwave Conference, 2000 Asia Pacific. pp. 1448-1451.

37. Personal Communication with SWISSto12.

38. **E. McLoughlan.** *Optimisation of a Near Field Scanning Syatem.* Maynooth : National University of Ireland, Maynooth, Masters Thesis, 2012.

39. *Rectangular to Large Diameter Conical Corrugated Waveguide Converter Based on Stacked Rings.* **S. Doherty, A. von Bieren, F. Cahill, A. Macor, E. de Rijk, N.**

Trappe, M. Billod, C. O'Sullivan. Lisbon, 2015. European Conference on Antennas and Propagation (EuCAP).

40. **Rohde & Shwartz.** *1EZ44: Time Domain Measurements using Vector Network Analyzer R&S®ZVR.* : Rohde & Shwartz, 1998. .

41. **R. G. Lyons.** *Understanding Digital Signal Processing.* Reading, Massachusetts : Addison-Wesley Publishing Company, 1997.

8. Appendix A

Presented here are the far-field beam patterns for the 6 horns designed for the standard WR bands.
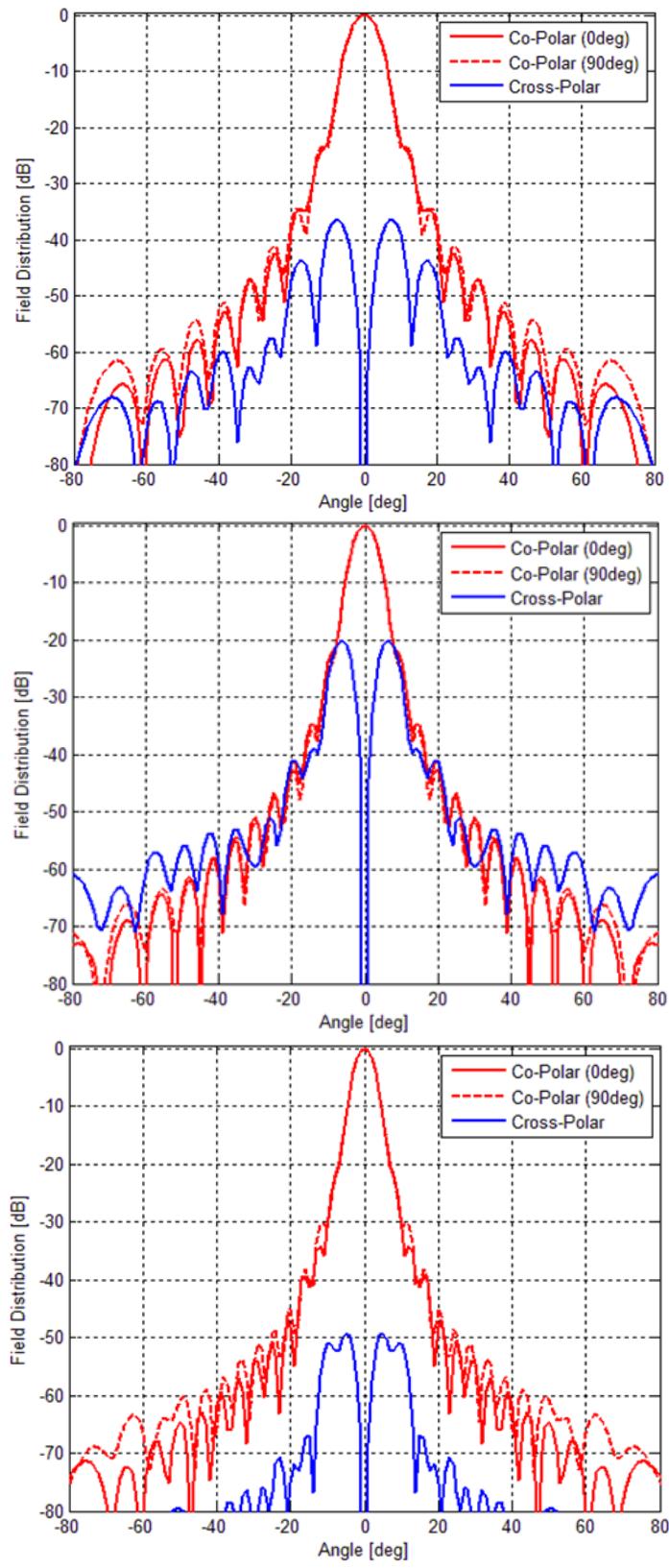
Figure A.1: Far field beam patterns for the WR-1.0 horn at 750GHz (top), 925GHz (middle) and 1100GHz (bottom).

134
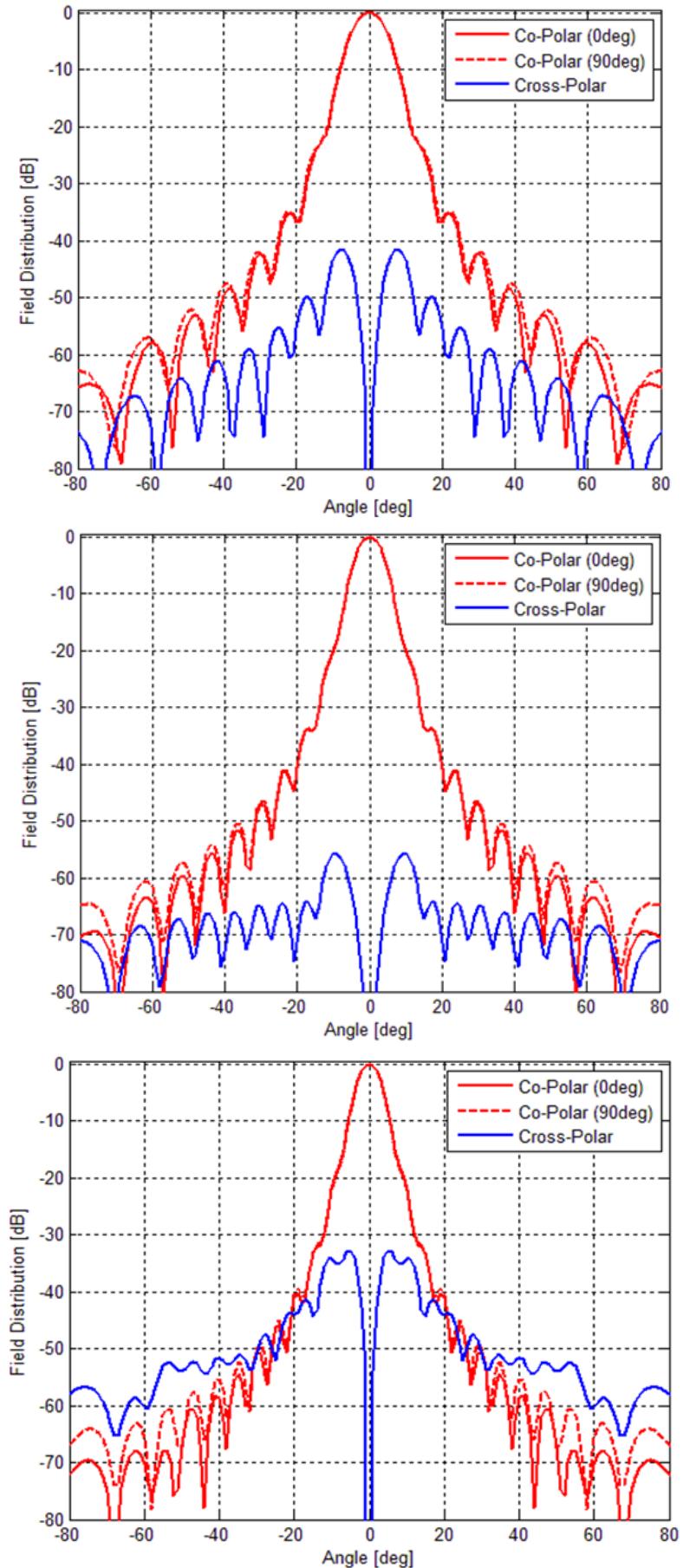
Figure A.2: Far field beam patterns for the WR-1.5 horn at 500GHz (top), 625GHz (middle) and 750GHz (bottom).

135
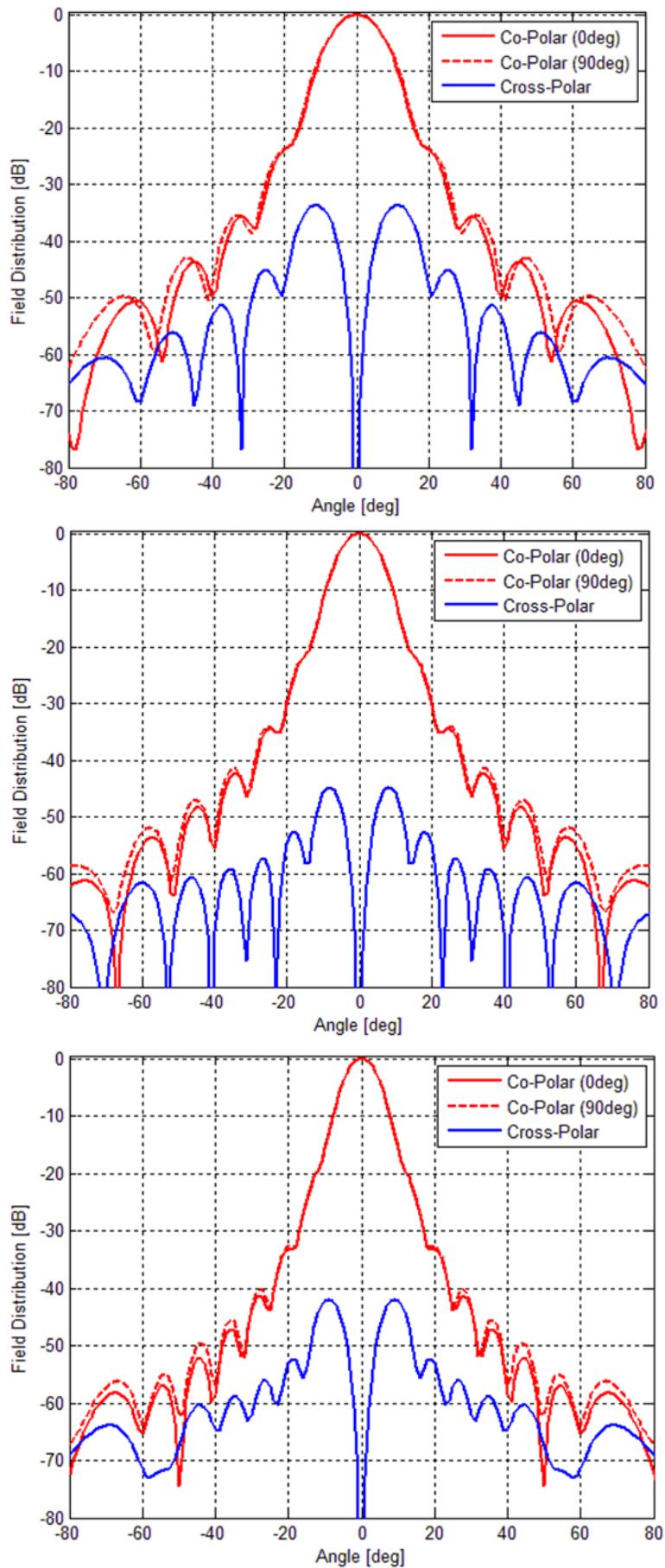
Figure A.3: Far field beam patterns for the WR-3.4 horn at 220 GHz (top), 275 GHz (middle) and 330 GHz (bottom).
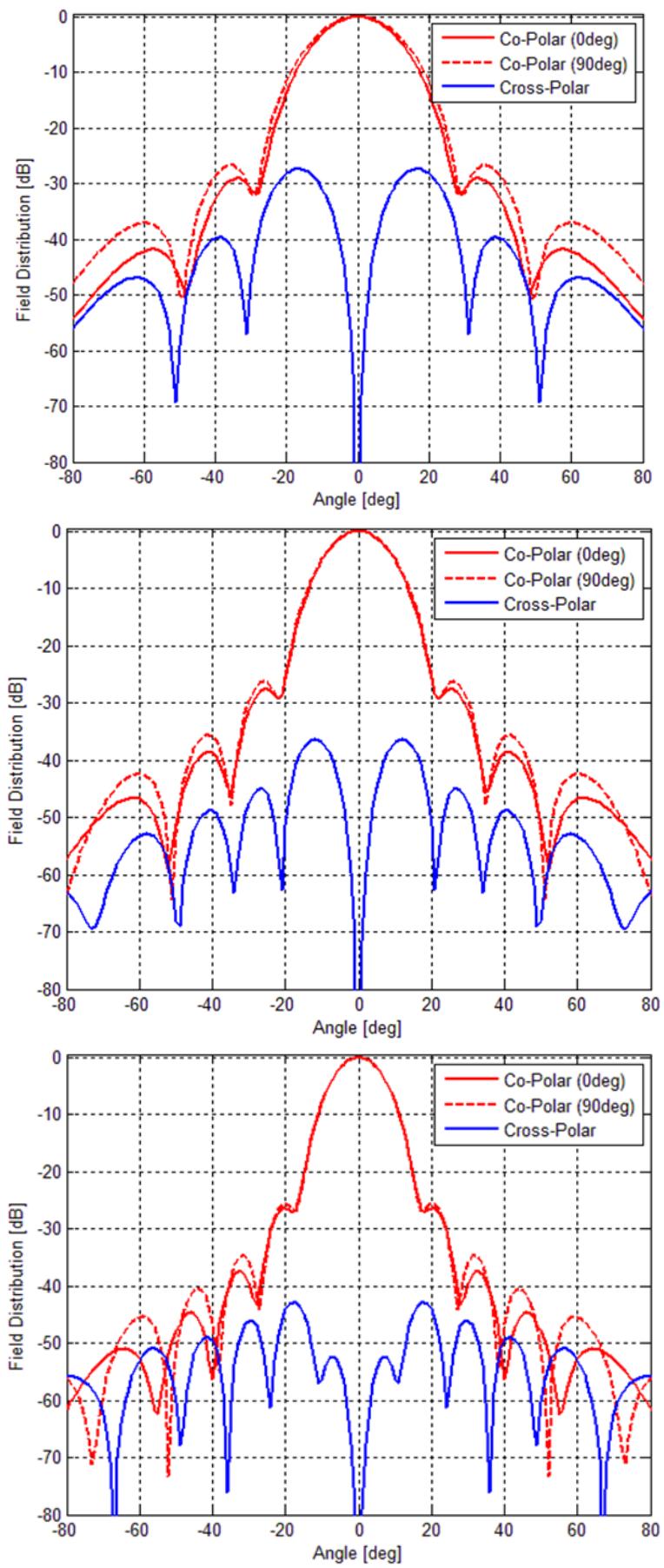
**Figure A.4: Far field beam patterns for the WR-5.1 horn at 140 GHz (top), 180 GHz (middle) and 220 GHz (bottom).**

137
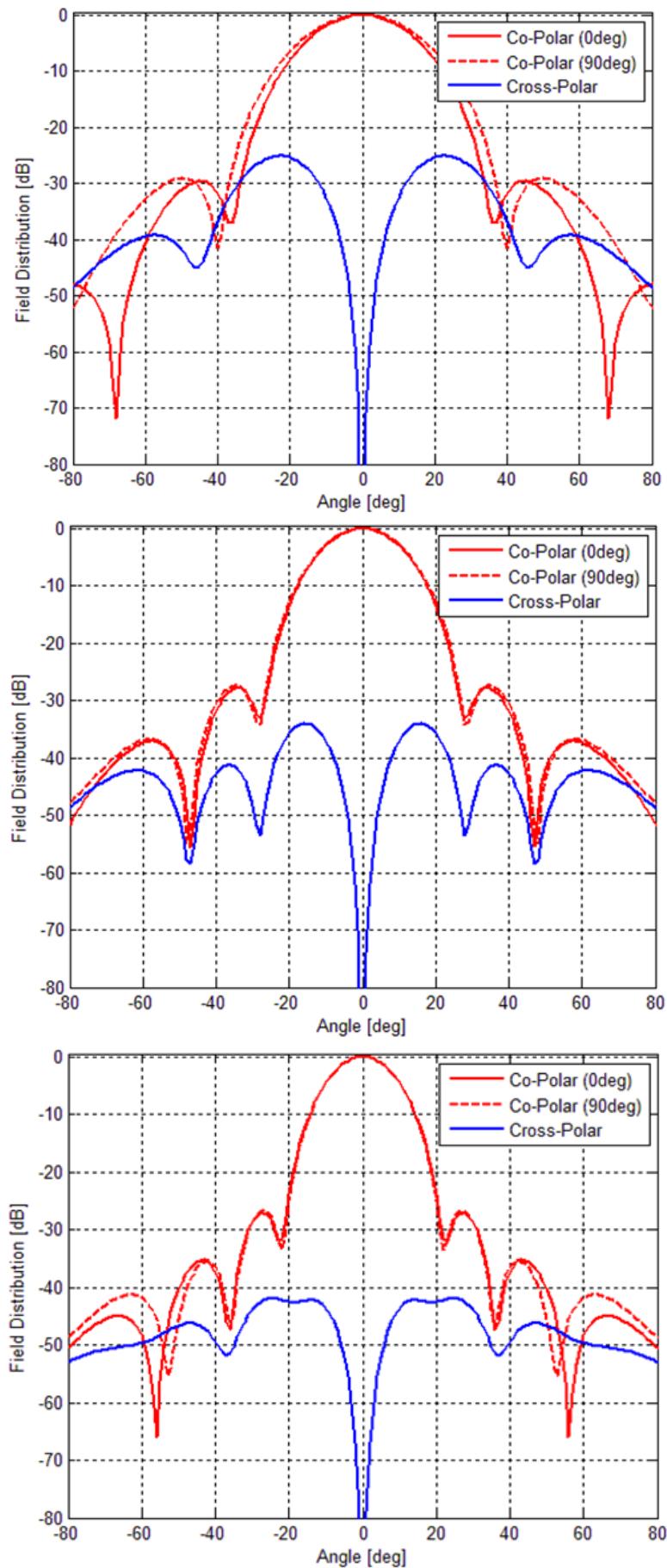
Figure A.5: Far field beam patterns for the WR-6.5 horn at 110 GHz (top), 140 GHz (middle) and 170 GHz (bottom).

138
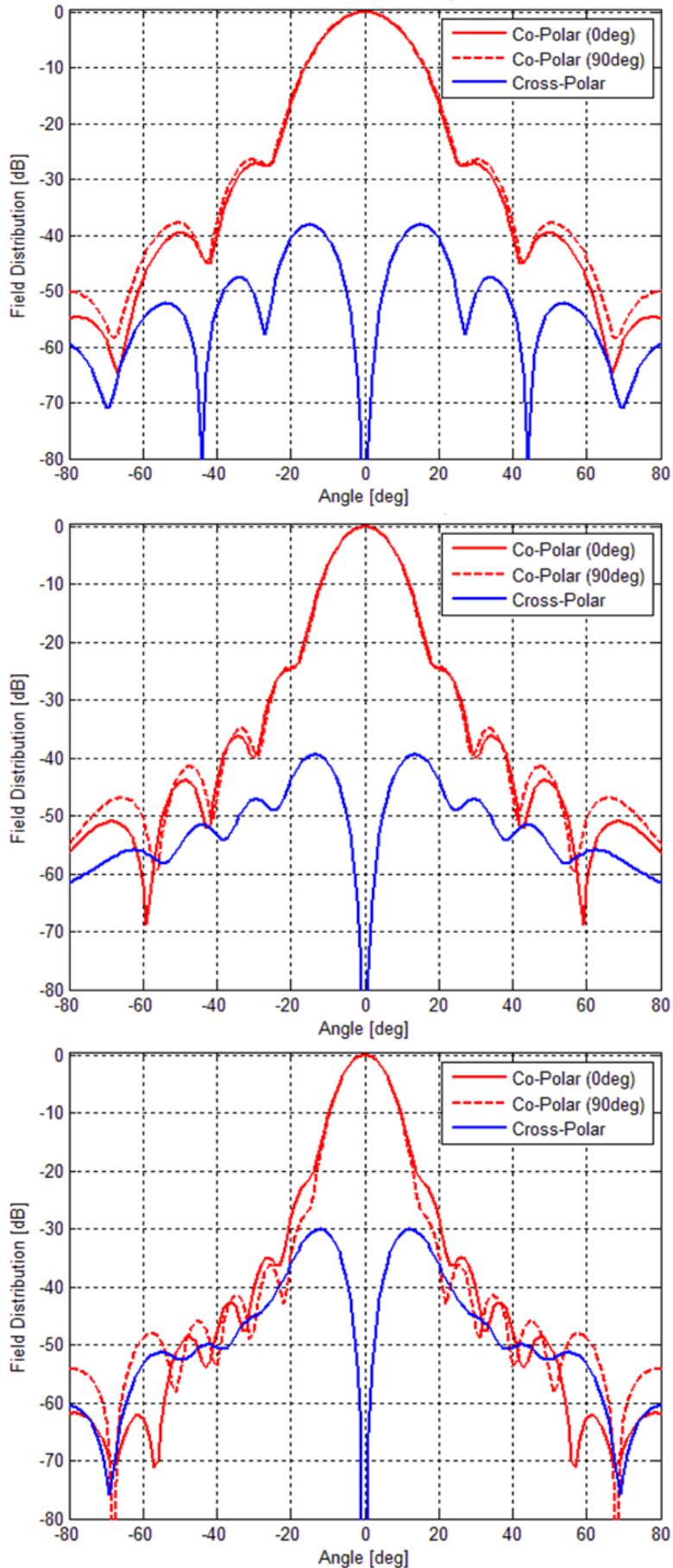
Figure A.6: Far field beam patterns for the WR-10 horn at 67.5 GHz (top), 91.25 GHz (middle) and 115 GHz (bottom).